UNIVERSITY OF OKLAHOMA

GRADUATE COLLEGE

COMBINING SEISMIC ATTRIBUTES AND MACHINE LEARNING FOR SEISMIC
FACIES ANALYSIS

A DISSERTATION

SUBMITTED TO THE GRADUATE FACULTY

in partial fulfillment of the requirements for the

Degree of

DOCTOR OF PHILOSOPHY

By

DAVID LUBO-ROBLES

Norman, Oklahoma

2022

COMBINING SEISMIC ATTRIBUTES AND MACHINE LEARNING FOR SEISMIC
FACIES ANALYSIS

A DISSERTATION APPROVED FOR THE

SCHOOL OF GEOSCIENCES

BY THE COMMITTEE CONSISTING OF

Dr. Matthew J. Pranter, Chair

Dr. Kurt J. Marfurt, Co-chair

Dr. Heather Bedle

Dr. Deepak Devegowda

To God.

Acknowledgments

First, I thank God for all the blessings he has given me throughout my whole life and for being my strength to accomplish this important objective for my professional and personal life.

To my advisors, Dr. Matthew J. Pranter and Dr. Kurt J. Marfurt, thank you for all their guidance, and dedication. You are excellent professionals, and it has been an honor to learn from you. Dr. Pranter, thank you for your constant motivation, and all your suggestions that enhanced and complement my research. Also, thanks for being an amazing person and for all your advice. Dr. Marfurt, thank you for giving me the opportunity to be one of your students and for your encouragement, and all the long conversations we had all these years in which we shared and discussed several ideas for research. You are a kind person, and I will always be grateful for your support.

I would like to express my greatest appreciation to my committee members Dr. Heather Bedle and Dr. Deepak Devegowda for all their technical input. Dr. Bedle thanks for all your advice and encouragement. Dr. Devegowda thanks for all your valuable and precise comments. Also, thank you to my colleagues Dr. Thang Ha, Dr. Vikram Jayaram, and Dr. Sivaramakrishnan Lakshmivarahan for their support during my research.

I would like to thank the amazing staff in the School of Geosciences, especially to Leah Moser, Rebecca Fay, Ginger Leivas, and Ashley Tullius, and all the members of the Attribute Assisted Seismic Processing and Interpretation (AASPI) and the Reservoir Characterization and Modeling Lab (RCML).

Lastly, to my parents Maria Elena and Eduardo and my grandfather Isidoro for all their unconditional love and for always be there for me.

Table of Contents

List of Figures

characterized by high-amplitude coherent reflectors (the purple rectangle 1). However, conformal sediments close to the edges of the salt show a rapid change in the amplitudes and dips and low-frequency noise (the purple arrows). These conformal sediments are characterized by lower seismic amplitudes and a reduction in the quality of the seismic image (the purple rectangle 2).

Figure 3.3. Sensitivity analysis, seismic facies classification, and application of SHAP values for model interpretation workflow. Three cases are generated to analyze how different perturbations made to the input attributes affect the classification: case 1 considers the seismic attributes computed from the original volume; case 2 applies a 3D Kuwahara filter (Qi et al., 2016; Lubo-Robles et al., 2021) to remove noise, sharpen the edges between seismic facies, and smooth their internal response; and case 3 adds band-limited AWGN with S/N = 2 to the entire survey and recomputes the seismic attributes using the same parameters as case 1. I select a suite of candidate seismic attributes based on my geologic insight and experience to differentiate between the target seismic facies. Then, I generate the training and validation data sets by manually picking a group of polygons enclosing each of the target seismic facies. Moreover, I apply a Min-Max scaler (Jain et al., 2005; Pedregosa et al., 2011) to remove scale dependency in the seismic attributes. Then, considering the seismic attributes from case 1, I perform a hyperparameter search and apply fivefold cross validation to find the most optimal hyperparameters to train a random forest architecture. The same hyperparameters are used for cases 2 and 3 to make an unbiased sensitivity analysis. Finally, I apply a SHAP TreeExplainer (Lundberg and Lee, 2017; Lundberg et al., 2018a) to compute the SHAP values and explain the outputs of the models. The SHAP global

deviation becomes the most important attribute followed by the total energy. For MTD, the attribute importance when considering case 1 is the same as the overall importance (Figure 3.9a) and relative changes in the attribute importance remain similar for cases 2 (Figure 3.9b) and 3 (Figure 3.9c). For salt, spectral bandwidth becomes the second most important attribute for the classification when applying Kuwahara filtering, while the GLCM contrast shows a large increase in its importance in the presence of strong random noise (case 3). Finally, for conformal sediments, GLCM entropy and spectral bandwidth become the third and fifth most important attributes in the classification when analyzing case 2. Moreover, when adding band-limited noise, the GLCM contrast shows a slight increase in its importance and becomes the fifth most important attribute, whereas the coherence shows a decrease in its importance.

Figure 3.11. The SHAP summary plots. Each dot represents an individual voxel of the training data set. The y-axis is associated with the attribute importance for each seismic facies, whereas the x-axis represents the SHAP value for each seismic attribute in the classification (Lundberg et al., 2020; Molnar, 2021). I observe that the attribute's effects are similar for all cases with only some differences. (a-c) For MTD, high to medium values of total energy, high values of dip deviation, energy deviation, and GLCM entropy, and low values of coherence, covariance of dip and energy gradient, GLCM contrast, and spectral bandwidth tend to increase the probability of having MTDs. (d-f) High values of dip deviation, GLCM contrast, and spectral bandwidth, and low values of total energy, energy deviation, coherence, covariance of dip and energy gradient, and reflector convergence increase the probability for the salt seismic facies. (g-i) Finally, for conformal sediments,

sediments. Note that positive SHAP values increase the probability and are characterized by the red colors, whereas negative SHAP values are associated with the blue colors and decrease the probability. (a-c) Total energy attribute. In general, the ML model correctly distinguishes between the target seismic facies. However, high-amplitude conformal sediments and reflectors with lower amplitude, lower seismic quality around the diapirs increase the probability of having MTDs (the white arrows). Some dipping reflectors and noisy areas close to the diapirs increase the probability of a voxel being classified as salt (the orange arrows), whereas overlap between conformal sediments and MTD is visible (the yellow arrows). (d-f) Dip deviation attribute. Overlap between MTD and salt is visible. In addition, MTDs still show overlap with the reflectors surrounding the diapirs (g-i) Energy deviation attribute. Salt diapirs show a strong overlap with the flat, high-amplitude conformal sediments located inside the mini-basins. Finally, using the dip and energy deviation attributes, dipping reflectors decrease the probability of having conformal sediments...129

the salt seismic facies, values of and covariance of dip and energy gradient smaller than 0.15-0.2 with lower values of coherence are pushing towards salt. However, some values larger than 0.15-0.2 also increase the probability for this seismic facies. (g-i) Finally, for the conformal sediments, two well-defined tends increasing the probability of a voxel being classified as conformal reflectors are seen: (1) values of covariance of dip and energy gradient smaller than 0.1-0.2 and higher values of coherence and (2) values of covariance of dip and energy gradient larger than 0.1-0.2 with lower values of coherence. 135

Figure 3.S4. The SHAP dependence plot for GLCM contrast. (a-c) For MTD, two trends are still visible, but there is some vertical overlap between them for cases 1 and 2. For these cases, values of GLCM contrast lower than approximately 90 and low to high values of covariance of dip and energy gradient and total energy are pushing towards MTDs. In contrast, for case 3, there is more vertical separation between the trends in which values of GLCM contrast smaller than 140 and low to high values of dip deviation are increasing the probability. (d-f) In cases 1 and 2 for the salt seismic facies, values of GLCM contrast larger than approximately 75-80 and low to high values of covariance of dip and energy gradient are increasing the probability of having salt. Moreover, when adding band-limited AWGN, a better definition of the trend for this seismic facies is seen in which values of GLCM contrast larger than approximately 140 with lower total energy are increasing the probability. (g-i) For the conformal sediments facies, two trends that are pushing towards this facies are still seen. For cases 1 and 2, the first trend is characterized by values of GLCM contrast lower than approximately 75-80 and lower values of energy deviation and covariance of dip and energy gradient, whereas the second trend show values of GLCM contrast larger than

with high values of total energy increase the probability (d-f) For salt, values of GLCM entropy larger than 0.5 with low to high values of covariance of dip and energy deviation are increasing the probability for cases 1 and 2 (g-i) Finally, for conformal sediments, values of GLCM entropy smaller than 0.5 with high values of total energy are increasing the probability. Note that some voxels characterized by GLCM entropy larger than 0.5 and lower total energy can also increase the probability of having MTD or conformal sediments. Moreover, applying Kuwahara filtering, trends for these seismic facies remain very similar to considering case 1, but the data look more compressed and clustered, making the trends better defined. Finally, similar to the spectral bandwidth attribute, trends using the GLCM entropy are lost in the presence of strong noise.

Figure 3.S7. SHAP dependence plot for reflector convergence. Using the original data, there is a strong overlap between facies and analyzing possible trends for this attribute is a challenging task. However, applying Kuwahara filtering or adding band-limited AWGN, these trends become slightly better defined for all seismic facies. However, some overlap between seismic facies still exists. (a-c) For MTD seismic facies, values of reflector convergence larger than approximately 0.25-0.3 with high values of covariance of dip and energy gradient have higher impact in the classification and increase the probability. However, some values characterized by reflector convergence lower than 0.25-0.3 and lower values of covariance of dip and energy gradient also increase the probability for this facies. (d-f) For salt, voxels characterized by reflector convergence lower than 0.3 and low values of coherence and high values of dip deviation increase the probability. (g-i) For the conformal sediments facies, two trends increasing the probability are seen: (1) values of

List of Tables

Abstract

Understanding how to correctly select a group of input seismic attributes is critical to perform a robust machine learning (ML)-based seismic facies analysis. However, due to the large number of seismic attributes enhancing different geologic features in the seismic volume and the fact that some of these attributes might offer redundant or irrelevant information, interpreters usually ask which the most optimal attributes are for their facies analysis and how the selected attributes might impact their results. In this dissertation, I evaluate three different strategies to address these challenges. In my first application, I introduce a novel technique called exhaustive probabilistic neural network (PNN), which combines an exhaustive search algorithm with a PNN to evaluate all possible combinations of seismic attributes and select the combination that best differentiates the target salt and nonsalt seismic facies in a 3D Eugene Island seismic volume located in the Gulf of Mexico. From seven candidate input attributes, the exhaustive PNN removed irrelevant attributes and found that a smaller group of four seismic attributes composed of the coherence, GLCM contrast, total energy, and dip deviation provided the most accurate result.

As a second approach, I apply Shapley additive explanations (SHAP) to understand how changes in the quality of the input seismic attributes might impact the predictions made by a random forest architecture trained to differentiate between mass transport deposits (MTDs), salt, and conformal siliciclastic sediments in the Gulf of Mexico. I found that the seismic attribute importance is dynamic and can change based on the facies analyzed and the quality of the input seismic amplitude and attributes data. Furthermore, I found that, the ML architecture learns a set of rules in multiattribute space to differentiate between the three

facies, where seismic attributes measuring variations in energy and dip contribute most to the classification.

My third attribute selection workflow was based on the well-established use of principal component analysis (PCA). Here, my goal was to choose the best attributes for use in unsupervised gas hydrate facies analysis in a seismic volume located in the Blake Ridge, offshore South Carolina, USA. For attribute selection, I apply PCA considering three training data selection strategies. I found that using a balanced training data set - composed of the same number of samples per seismic facies – offered the best identification of the gas hydrate bottom-simulating reflectors (BSRs) and reduced the overlap with surrounding facies. A weakness of this workflow is due to PCA measuring the impact of individual seismic attributes instead of the optimal attribute combination, with the total number of attributes used subjective rather than quantitative. I use the selected attributes as input for self-organizing maps (SOM) classification.

After this evaluation, I find that the exhaustive PNN technique offers a robust implementation to quantitatively select the most optimal seismic attribute combination to perform a supervised seismic facies analysis, whereas SHAP provides the best insight not only into which attributes provide the highest individual importance in the classification, but also as to what attribute (e.g., anomalously high or low) value offers the best discrimination between the target facies, providing better insight into not only how the ML model works, but also in the underlying seismic expression of the geology.

Chapter 1: Introduction

Machine learning (ML) and seismic attributes have been increasingly applied by geoscientists to discover patterns in their data and identify geologic features of interest as a means to perform a more complete and faster reservoir characterization (Roy et al., 2014; Zhao et al., 2015; Di et al. 2017, 2019; Lubo-Robles and Marfurt, 2019; Wu et al., 2019).

For ML-based seismic facies analysis, seismic attributes have become common inputs. Following Chopra and Marfurt (2007), a seismic attribute consists of any measure computed from a seismic amplitude volume that successfully enhances geologic features in a depositional environment. However, since the introduction of complex trace attributes by Taner et al. (1979), the number of attributes has exploded where many of them provide redundant and irrelevant information (Barnes, 2007), making an integrated analysis of these measurements difficult for all but the most experienced seismic interpreters (Roden et al., 2015)

Therefore, determining the most optimal seismic attribute combination to use as input into a ML algorithm to distinguish among seismic facies continues to be a challenging task. Such a choice requires not only a substantial understanding on what seismic attributes measure and how they respond to the seismic expression of stratigraphic and structural features of interest but also as to how changes in the input attributes might impact the results obtained from the ML models.

This dissertation aims to address the challenges stated above, and is structured as follows:

In Chapter 2, I introduce a novel technique called exhaustive probabilistic neural network (PNN), which couples a PNN with an exhaustive search algorithm to test all possible combinations of seismic attributes and select the most optimal attribute combination to perform a supervised seismic facies classification to distinguish between salt and nonsalt seismic facies in a Gulf of Mexico seismic amplitude volume.

In Chapter 3, I train a random forest model to distinguish between mass transport deposits, salt, and conformal sediments in the Gulf of Mexico and apply Shapley additive explanations (SHAP) to understand how perturbations made to the input seismic attributes such as applying a Kuwahara filter or adding band-limited noise affect the model predictions. Moreover, by corendering the SHAP values with the seismic amplitude volume, I perform an in-context interpretation to evaluate how changes in the geology impact the model classification.

In Chapter 4, I use a suite of geometric and spectral attributes as input into self-organizing maps (SOM) to perform an unsupervised seismic facies analysis as a means to identify bottom simulating reflectors (BSRs) and surrounding facies in a seismic volume located in the Blake Ridge, offshore South Carolina, USA where the attributes are selected using those that contribute most to the first several principal components. Because my objective is to differentiate specific target seismic facies, I evaluate the use of three different training data sets: (1) using all seismic data samples found in the entire 3D seismic volume, (2) using biased training data that are extracted from polygons only enclosing the BSRs, and (3) using biased training data considering four main seismic facies including the BSRs, chaotic to sigmoid reflectors, low-amplitude reflectors, high-amplitude, high frequency

reflectors, and trapped free gas. Finally, in Chapter 5, I summarize the major conclusions

based on the results obtained in Chapters 2, 3 and 4 in the dissertation.

References

Barnes, A. E., 2007, Redundant and useless seismic attributes: Geophysics, **72**, P33–P38.

Chopra, S., and K. J. Marfurt, 2007, Seismic Attributes for Prospect Identification and Reservoir Characterization, SEG Geophysical Development Series, 11.

Di H., M. A. Shafiq, and G. AlRegib, 2017, Seismic fault detection based on multi-attribute support vector machine analysis, 87th Annual International Meeting, SEG, Expanded Abstracts, 2039-2044.

Di H., M. A. Shafiq, Z. Wang, and G. AlRegib, 2019, Improving seismic fault detection by a super-attribute-based classification, Interpretation, **7**, SE251-267.

Lubo-Robles, D., and K. J. Marfurt, 2019, Independent component analysis for reservoir geomorphology and unsupervised seismic facies classification in the Taranaki Basin, New Zealand: Interpretation, **7**, SE19–SE42.

Roden, R., T. Smith, and D. Sacrey, 2015, Geologic pattern recognition from seismic attributes: Principal component analysis and self-organizing maps: Interpretation, **3**, SAE59–SAE83.

Roy A., A. S. Romero-Peláez, T. J. Kwiatkowski, and K. J. Marfurt, 2014, Generative topographic mapping for seismic facies estimation of a carbonate wash, Veracruz Basin, southern Mexico: Interpretation, **2**, SA31-SA47.

Taner, M. T., F. Koehler, and R. E. Sheriff, 1979, Complex seismic trace analysis: Geophysics, **44**, no. 6, 1041-1063.

Wu X., L. Liang, Y. Shi, and S. Fomel, 2019, FaultSeg3D: Using synthetic data sets to train an end-to-end convolutional neural network for 3D seismic fault segmentation: Geophysics, **84**, no.3, IM35-IM45.

Zhao, T., V. Jayaram, A. Roy, and K. J. Marfurt, 2015, A comparison of classification techniques for seismic facies recognition: Interpretation, **3**, SAE29–SAE58.

Chapter 2: Exhaustive probabilistic neural network for attribute selection and supervised seismic facies classification*

Abstract

Machine learning (ML) algorithms, such as principal component analysis, independent component analysis, self-organizing maps, and artificial neural networks, have been used by geoscientists to not only accelerate the interpretation of their data, but also to provide a more quantitative estimate of the likelihood that any voxel belongs to a given facies. Identifying the best combination of attributes needed to perform either supervised or unsupervised ML tasks continues to be the most-asked question by interpreters. In the past decades, stepwise regression and genetic algorithms have been used together with supervised learning algorithms to select the best number and combination of attributes. For reasons of computational efficiency, these techniques do not test all of the seismic attribute combinations, potentially leading to a suboptimal classification. In this study, I have developed an exhaustive probabilistic neural network (PNN) algorithm that exploits the PNN's capacity in exploring nonlinear relationships to obtain the optimal attribute subset that best differentiates target seismic facies of interest. I determine the efficacy of my proposed workflow in differentiating salt from nonsalt seismic facies in a Eugene Island seismic survey, offshore Louisiana. I find that from seven input candidate attributes, the

exhaustive PNN is capable of removing irrelevant attributes by selecting a smaller subset of four seismic attributes. The enhanced classification using fewer attributes also reduces the computational cost. I then use the resulting facies probability volumes to construct the 3D distribution of the salt diapir geobodies embedded in a stratigraphic matrix.

Introduction

The past two decades have seen an increasing use of unsupervised and supervised machine learning (ML) techniques for geophysical applications such as fault detection (Di et al., 2017, 2019; Wu et al., 2019), seismic facies analysis (Roy et al., 2014; Zhao et al., 2015; Amin et al., 2017; Long et al., 2018; Wrona et al., 2018), and prediction of well log properties based on seismic attributes (Hampson et al., 2001; Dorrington and Link, 2004). For seismic facies classification, interpreters select a suite of seismic attributes as input to define a multivariate classification task. Common attributes used for classification include the same geometric, instantaneous, spectral, textural, and geomechanical attributes that human interpreters have found to be useful.

In supervised learning, the goal is to differentiate one or more interpreter-defined target seismic facies from each other and from an undifferentiated background. In unsupervised learning the goal is to provide a relatively unbiased classification of the dominant facies which may or may not have geologic significance. However, whether the interpreter is performing an unsupervised or supervised seismic facies classification, the choice of attributes and the selection of training data strongly bias the results. Moreover, selecting the best attribute combination to distinguish different target facies requires

5

significant understanding of not only geologic processes and the seismic expression of structural and stratigraphic patterns, but also of the features measured by seismic attributes.

There are three other challenges in using ML for seismic facies analysis: (1) the Hughes (1968) phenomenon in which the classification performance of a ML algorithm decreases after reaching a certain number of input features, (2) the overwhelming number of attributes that limit the interpreter's ability to interact with all the information available (Roden et al., 2015), and (3) the presence of redundant and irrelevant attributes that do not provide any additional information and create confusion for human interpreters (Barnes, 2007), and, at best, increased cost for ML algorithms.

A partial solution is dimensionality reduction. Principal component analysis (PCA) and independent component analysis are simple projection techniques that find the statistically most important features (Guo et al., 2009; Qi and Castagna, 2013; Chopra and Marfurt, 2014; Honorio et al., 2014; Roden et al., 2015; Lubo-Robles and Marfurt, 2019). Generative topographic maps (GTM) and self-organizing maps are unsupervised learning algorithms in which a multidimensional data set is projected into a lower dimensional space to extract the most valuable information from the data (Roy et al., 2014; Roden et al., 2015; Zhao et al. 2015; Qi et al., 2016; Zhao et al., 2018). If one allows a large number of classes (colors), the classification is approximately continuous, with the final "categorical" classification defining specific seismic facies provided by the human interpreter. Once the major facies have been mapped and their attribute sensitivity are quantified, a smaller suite of attributes or linear combinations of attributes can be used for supervised learning.

Considerably more progress has been made in predicting continuous variables from seismic attribute data. Working with seismic attributes and well-log data, Hampson et al. (2001) use stepwise multilinear regression to choose the best number and collection of seismic attributes to predict a desired well-log property. Dorrington and Link (2004) generalize this approach by using a genetic algorithm together with a multilayer feedforward network to select seismic attributes for porosity prediction. Support vector machine (SVM) algorithms define weights to be applied to the different attributes to achieve the desired separation between seismic facies. In their work, Chang-kai and Wen-kai (2010) use those attributes with larger SVM weights to construct a smaller subset of attributes to differentiate reservoir from nonreservoir seismic facies. Amin et al. (2017) use information theory to rank the seismic attributes and determine the optimal attribute subset for salt-dome detection.

Wang et al. (2015) combine a rough sets algorithm with PCA to reduce the number of attributes used as input for porosity prediction. Finally, Galvis et al. (2017) first use a relevancy filter to discard attributes showing high correlation and then apply a wrapper forward method selection based on k-means to select the optimal combination of attributes to identify surface waves in multicomponent common-shot gathers.

One key limitation to these workflows is that they do not test all the possible combinations of input features; thus, they can miss important relationships existing between the attributes. Recently, Qi et al. (2020) evaluate all possible combinations of seismic attributes to differentiate among salt, mass-transport deposits (MTDs) and conformal sediments using a semisupervised learning technique consisting of applying Gaussian mixture models (GMMs) and Bhattacharyya distance to measure the similarity between two

7

GMMs per facies and select the optimal combination associated with the maximum average cumulative distance, and then GTM is applied to perform an unsupervised seismic facies classification.

In this study, I propose to perform an exhaustive search in which all possible $2^M - 1$ combinations are tested, where M represents the number of input seismic attributes. Because testing all possible combinations of attributes is computationally expensive and the algorithm's complexity is proportional to the number of input attributes, I use a supervised ML technique called the probabilistic neural network (PNN), which is based on well-established Gaussian statistics and allows for a more robust probability density function (PDF) estimation based on Parzen windows and Bayes's criteria to provide simple, fast, and repeatable training in which only the smoothing parameter r requires optimization.

By coupling an exhaustive search algorithm with the PNN, I can explore nonlinear relationships between seismic attributes and seismic facies. The goal of my "exhaustive PNN" is to test all possible combination of seismic attributes, reject irrelevant and redundant attributes, provide the optimal combination to distinguish salt from siliciclastic seismic facies, and perform a supervised seismic facies classification.

I begin my paper with a summary of the mechanics of PNN applied to seismic facies classification. I then describe my exhaustive search algorithm to create different subsets of seismic attributes that are then provided to a PNN to measure their performance. After selection of the best combination, I apply a first-order gradient optimization technique called Adam to further improve the performance of the neural network.

Next, I apply my algorithm to the Eugene Island 3D seismic survey located in the Gulf of Mexico. To differentiate the low-amplitude, discontinuous reflectors associated with salt diapirs from the high-amplitude, parallel reflectors associated with the surrounding conformal sedimentary layers, I use discontinuity, texture, and nonparallelism attributes. I also manually define the target facies of the training and validation data sets to represent salt diapirs and conformal reflectors. Given the optimal combination of seismic attributes, I perform a supervised seismic facies classification and analyze whether the proposed workflow can determine the best combination of seismic attributes for the desired classification task. An appendix provides mathematical details explaining how the algorithm works.

Geologic background

The Eugene Island minibasin is a giant Plio-Pleistocene oil and gas field located offshore Louisiana in the outer continental shelf of the Gulf of Mexico (Alexander and Flemings, 1995; Joshi and Appold, 2016). Following Alexander and Flemings (1995), the Eugene Island minibasin evolution can be described in three phases.

The first phase of evolution is characterized by the deposition of distal deltaic sands, bathyal and prodelta shales, and turbidites on top of a salt sheet. This sediment loading caused the salt sheet to migrate outward laterally, creating new accommodation space in the area (Alexander and Flemings 1995; Joshi and Appold, 2016). The second phase is related to high sediment accumulation rates due to salt withdrawal and is characterized by lowstand deltas associated with deposition of mud and sand sequences (Alexander and Flemings, 1995; Joshi and Appold, 2016). Finally, the third phase is associated with fluvial deposits

9

and a decrease of salt withdrawal in which little accommodation space was further developed (Alexander and Flemings, 1995; Joshi and Appold, 2016).

Data set

The Eugene Island seismic survey is located in the Gulf of Mexico, offshore Louisiana, and it has an area of approximately 306 km^2. For this study, the seismic volume consists of 700 inlines and 700 crosslines with a bin size of 82.5 x 82.5 ft and record length of 3 s.

Figure 2.1a shows a representative vertical slice along inline 521 through the seismic amplitude volume. I observe a salt diapir (salt diapir 1; the red arrow) associated with salt withdrawal during the prodelta and proximal deltaic phases of deposition (Alexander and Flemings, 1995; Joshi and Appold, 2016) surrounded by high-amplitude, laterally continuous conformal reflectors. In general, salt diapir 1 is characterized by low-amplitude, discontinuous reflectors. However, crossing coherent migration artifacts (the blue arrow) associated with the high P-wave velocity and geometry of the salt (Jones and Davison, 2014) are seen inside salt diapir 1.

Also, I show a time slice at $t = 2$ s through the seismic amplitudes in the Eugene Island survey (Figure 2.1b). Besides salt diapir 1, I observe the presence of another salt diapir (salt diapir 2) that is also characterized by low-amplitude, discontinuous reflectors.

Methods

PNN

The PNN is a type of feedforward neural network widely used in classification tasks. To classify a given voxel, the PNN uses Parzen windows and Bayes's criteria to estimate its PDF and assigns it to the class in which the PDF is largest (Specht, 1990; Masters, 1995; Hajmeer and Basheer, 2002). Several kernels can be used during the Parzen window estimation; however, the most common kernel used is the Gaussian function due to its high performance and simple computation (Masters, 1995). I begin by subdividing my volume into three parts: (1) labeled training data used to define several of the necessary parameters for the model, (2) labeled validation data used to test my algorithm's performance during the learning phase, and (3) the remainder of the volume representing test/unseen data to be classified by the trained PNN. In my application, both the training and validation data are generated by the human interpreter drawing polygons around facies of interest. In addition, another approach to assess the effectiveness of the model when classifying previously unseen data can be defining a test dataset by picking polygons for the seismic facies of interest but using salt diapir 2 and its surrounding conformal sediments instead of performing the seismic facies classification in the whole volume. The *m*th attribute at a training sample n, a_{nm}, defines a component of a seismic attribute vector $\mathbf{a}_n$. Given my training data composed of a set of training seismic attributes vectors $\mathbf{a}$, the average estimated PDF $g_k(\mathbf{x})$ is given by:

$$g_k(\mathbf{x}) = \frac{1}{N_k} \sum_{n=1}^{N_k} \exp\left[-\sum_{m=1}^{M} \frac{(x_m - a_{nm})^2}{r^2} \right],$$
(1)

where N_k is the number of training samples associated with the kth class defined by the training data, M is the number of input attributes, **x** is a validation seismic attribute vector, and r is a smoothing parameter that requires careful selection through training.

The PNN architecture consists of four layers (1) the input layer, (2) the pattern layer, (3) the summation layer, and (4) the output layer (Specht, 1990; Masters, 1995) (Figure 2.2a). In the input layer, an unknown input sample is selected to be classified into a particular class. Second, in the pattern layer, the PNN starts by computing the difference between the validation and the training attributes (Figure 2.2b). This difference is then input into the Gaussian activation function in equation 1 (Masters, 1995). In the summation layer, the PNN calculates the average estimated density function $g_k(\mathbf{x})$ for each class. Finally, in the output layer (Figure 2.2b), the PNN assigns the unknown sample to class q where

$$g_q(\mathbf{x}) \geq g_k(\mathbf{x}) \, k = 1, 2, \dots, K. \tag{2}$$

PNN also provides confidence estimates of the classification (Masters, 1995) given by

$$P_k(\mathbf{x}) = \frac{\frac{1}{N_k} \sum_{n=1}^{N_k} \delta_{nk} \exp\left[-\sum_{m=1}^{M} \frac{(x_m - a_{nm})^2}{r^2}\right]}{\sum_{k=1}^{K} \left[\frac{1}{N_k} \sum_{n=1}^{N_k} \delta_{nk} \exp\left[-\sum_{m=1}^{M} \frac{(x_m - a_{nm})^2}{r^2}\right]\right]}, \tag{3}$$

where P_k represents the normalized probabilities given by the estimated PDF of each class k , $g_k(\mathbf{x})$, divided by the sum of all the density functions of all K classes. The Kronecker delta δ_{nk} is equal to one if the training case n belongs to class k, and it is zero otherwise.

PNN training

To optimize the smoothing parameter r, I sweep over a range of values for r, and select the one associated with the minimum continuous error function $e_k(\mathbf{x})$ defined by Masters (1995) as

$$e_k(x) = [1 - P_k(x)]^2 + \sum_{j \neq k}[P_j(x)]^2, \qquad (4)$$

Because I am interested in the error of all the samples, I define the global error as

$$E = \frac{1}{H}\sum_{h=1}^{H} e_k(\mathbf{x}_h), \qquad (5)$$

where H is the number of validation samples.

A limitation of the sweeping over values of the smoothing parameter r is that it uses the same value for each seismic attribute. To adapt the selection of r for each attribute, I use an adaptive learning rate first-order gradient stochastic optimization algorithm called Adam, which computes the first and second moments of the gradient of E with respect to the smoothing parameter r (Kingma and Ba, 2015). For more information on the mathematical details of the Adam procedure, please refer to Appendix A.

Exhaustive PNN workflow

I present a novel technique called exhaustive PNN, which uses a PNN-based architecture and a voxel-type classification for the model generation to automatically determine the best suite of seismic attributes for performing a supervised seismic facies classification.

The first step in the exhaustive PNN workflow (Figure 2.3) consists of selecting a suite of candidate seismic attributes using my geological insight. Using $M = 7$ candidate input attributes, the total number of combinations is $2^M - 1 = 127$. Then, I apply a 3D Kuwahara filter to block and smooth the seismic attributes, preconditioning them for subsequent classification (Qi et al., 2016). Second, a group of polygons for each facies is selected to create the training and validation data sets used for the model generation. In this application, supervised data labeled by the interpreter represents 0.0093% of the seismic volume after picking the polygons for each seismic facies on seven coarsely spaced inlines. Then, these data were split into two parts, with 80% of the voxels belonging to the training data, and the remaining 20% of the voxels belonging to the validation data set.

In addition, to avoid any bias related to different units between the input candidate attributes, an attribute scaling scheme is required. In general, seismic attributes are characterized by super-Gaussian distributions (Walden 1985; Honorio et al., 2014; Lubo-Robles and Marfurt, 2019), whereas other attributes such as Sobel filter similarity, and spectral magnitude components show a Poisson distribution. Therefore, instead of using a Z-score normalization in which a Gaussian distribution is assumed, I scale my data using estimators that are robust in the presence of outliers (Huber, 1981) and do not assume knowledge of the distribution. In this study, I perform a robust scaling, in which the data are centered using the median and scaled using the interquartile range (IQR) given by the difference between the 75th and 25th percentiles. The robust scaling percentiles are computed from the training data and are used to scale the training and validation data sets.

I define an initial seismic attribute combination and smoothing parameter r to initialize the exhaustive PNN algorithm. To select the best smoothing parameter r, I sweep through values ranging from $0.05 \leq r \leq 3.5$ with an interval $\Delta r = 0.05$ and I use equation 5 to compute the validation $E_V(r)$ and training $E_T(r)$ errors. These errors are stored, and a new seismic attribute combination is defined. A smoothing parameter r is computed for each of the 127 possible attribute combinations, which are ranked based on their validation error (E_V), and then I interpret these results and select the optimal combination of seismic attributes and smoothing parameter r that provides the smallest validation error, while maintaining a balanced bias-variance trade-off.

In PNN, the training data set is used to construct the pattern layers (or a weighted combination of attributes) that will later be "learned" by the algorithm in the training step. The validation error (E_V) is computed when considering the validation data set in the input layer, whereas the training error (E_T) is calculated when comparing the training data set with itself.

At this point, my exhaustive search algorithm only allows training of the neural network using the same smoothing parameter r for each seismic attribute. To relax this restriction, I can implement an optional step that further minimizes the validation error on the best combination by using the Adam optimization technique (Kingma and Ba, 2015) (Appendix A). Once trained and validated, I apply the PNN classifier to the optimum set of attributes and compute the probability of each class.

Bias-variance trade-off

In ML, interpreters face a bias-variance trade-off in which they need to create a model that provides an accurate prediction of the data at hand, but that is general enough to classify new data (Briscoe and Feldman, 2011; Goodfellow et al., 2016).

Briscoe and Feldman (2011) find that high-variance models are associated with overfitting whereby the classifiers fit the training data very well but loose generalization performance. In contrast, high-bias models cannot capture correctly the patterns found in the training data, thus leading to underfitting.

To find a balanced bias-variance trade-off, I analyze the relationship between the classifier's error when evaluating my training and validation data sets. In general, underfitting is associated with relatively high training and validation errors, whereas overfitting is characterized by a gap between the training and validation errors in which the former decreases during training, but the latter increases after finding a minimum value associated with the best generalization performance (Jabbar and Khan, 2015; Goodfellow et al., 2016).

Candidate seismic attributes

Seismic attributes are powerful tools that allow interpreters to better visualize geologic features of interest as well as to quantify reservoir properties such as continuity and morphology to study the structural and depositional setting of a particular environment (Chopra and Marfurt, 2007).

To perform the supervised seismic facies classification to differentiate between salt and nonsalt facies in the Eugene Island seismic volume, I evaluate seven candidate seismic attributes selected based on my geologic insight and past experience: coherence, gray-level cooccurrence matrix (GLCM) contrast, GLCM dissimilarity, total energy, energy deviation, covariance of dip and energy gradient, and dip deviation. These seven candidate attributes serve as input to my exhaustive PNN algorithm with the goal of finding the best subset combination of the seven seismic attributes and the corresponding smoothing parameter r.

The coherence attribute provides a measure of similarity between neighborhood traces, and it is widely use by seismic interpreters in order to map discontinuities in the seismic data such as faults and channels edges (Chopra and Marfurt, 2007; Li and Lu, 2014) as well as low-energy, discontinuous reflectors associated with salt and shale diapirs (Chopra and Marfurt, 2007). The total energy attribute measures the sum of the energy of the neighborhood analytic traces in which geologic features associated with low-amplitude, chaotic reflectors are characterized by low coherent energy.

GLCM or texture attributes analyze lateral and vertical changes in seismic amplitudes, allowing the delineation of geologic features that are characterized by complicated patterns or textures (Haralick et al., 1973; Angelo et al., 2009). In this paper, I compute two GLCM attributes: GLCM contrast, which calculates the local intensity variation between data samples (Chopra and Marfurt, 2007; Di and Gao, 2017), and GLCM dissimilarity, which also measures the intensity variation between samples but is less sensitive to outliers than GLCM contrast.

Nonparallelism attributes (Qi and Marfurt, 2019) provide the standard deviation of structural dip and amplitude gradients within an analysis window. The energy gradient measures how the seismic energy varies laterally along the structural dip, whereas the dip deviation attribute computes changes from parallel to chaotic reflections. The covariance of dip and energy seismic attribute is sensitive to highly chaotic, rotated, and high-amplitude deformed reflectors. Conformal sediments are characterized by similar dips in an analysis window, MTD and karst collapse exhibit greater variability, whereas the "reflectors" within salt are a mix of coherent and random noise, giving rise to rapidly changing dips and amplitude gradients.

In Figure 2.4, I show the 3D Kuwahara-filtered seismic attributes along inline 521. I note that the selected candidate attributes show different responses when comparing the salt diapir (the red arrow) against the more coherent, higher amplitude background geology. Moreover, I observe that applying a Kuwahara filter using 3D overlapping oblique cylindrical windows aligned with the average structural dip smooths the internal seismic response of salt diapir 1 and sharpens its edges, thus improving the discrimination between salt and the nonsalt seismic facies.

Definition of training and validation datasets

To generate a PNN model to isolate the salt diapirs present in the Eugene Island data set from the background geology, I need to define my training and validation data sets. As training data, I pick a suite of polygons for inline 501 to 551 at 10-line intervals (Figure 2.5a-2.5f) to extract the voxels of the salt (the purple polygon) and nonsalt (the green polygon) seismic facies from the seven seismic attributes used as input in the exhaustive PNN

workflow. For the validation data set, I only pick a suite of polygons enclosing the salt (the purple polygon) and nonsalt (the green polygons) facies along inline 451 (Figure 2.5g). These training and validation data sets consist of approximately 28,500 and 5500 voxels, respectively, thus maintaining an approximate 80%-20% splitting ratio for training the PNN.

Note that the training and validation sets are generated only for salt diapir 1 to leave salt diapir 2 as testing data (Figure 2.1) to evaluate the performance of the PNN when classifying new unlabeled (unseen) data. In addition, no time slices are used when generating these data sets to avoid any data leakage from the validation to the training data set. In practice, I suggest using those inlines that best exhibit the variability in the data volume.

Results

Attribute selection to discriminate salt from the background geology in the Eugene Island seismic volume using exhaustive PNN

After I select the candidate seismic attributes to be used as input in the exhaustive PNN algorithm (Figure 2.4) and generate the training and validation data sets defining the salt and nonsalt seismic facies (Figure 2.5). I apply a robust scaling to change the units of the seismic attributes to a common scale to avoid any bias that can affect the prediction accuracy of the model.

In Figure 2.6, I show the histograms of the training data set before (Figure 2.6a) and after (Figure 2.6b) applying robust scaling to all of the input features. I observe that the shape of the distributions is maintained after scaling and that all input features have similar range. Moreover, input features such as the coherence, GLCM contrast, GLCM dissimilarity,

covariance dip and energy, and dip deviation are characterized by a bimodal distribution, whereas the total energy and energy deviation are associated with a skewed distribution. Applying the robust scaling results in a better scaling scheme than a Z-score normalization that assumes a normal distribution of the data.

Observe that the shape of the distributions is maintained after applying the robust scaling percentiles computed from the training data set to the validation samples (Figure 2.7). Also note that the candidate attributes for the training and validation data sets show very similar distribution meaning that I am capturing the same intrinsic patterns on both data sets, which the PNN "learns" to distinguish between salt and nonsalt seismic facies in the Eugene Island seismic survey.

When running the exhaustive PNN algorithm using seven input candidate attributes, I test 127 different combinations between the attributes. I then store the ideal smoothing parameter r associated with the best validation (E_V) and training (E_T) errors to make a low bias-low-variance model able to generalize when classifying the remaining unlabeled data. Also, in this application, I compute a suite of evaluation measures given by the accuracy, precision, recall, specificity, and the area under the received operating characteristic (ROC) curve to further assess the performance of the combinations (Lachiche and Flach, 2003; Fawcett, 2004; Sokolova et al., 2006; Sokolova and Lapalme, 2009).

Performance evaluation metrics are constructed from the confusion matrix in which correctly classified and misclassified samples for each class are stored and divided into true-positive, true-negative, false-positive, and false-negative categories (Sokolova et al., 2006;

Sokolova and Lapalme, 2009). In this study, the positive and negative classes are associated with the salt and nonsalt seismic facies, respectively.

Following Sokolova et al. (2006) and Sokolova and Lapalme (2009), the accuracy estimates the global performance of the classifier without considering a specific class, whereas precision and recall compute how often the model correctly classified the positive class. Precision is defined as the ratio of true positives to the total number of samples predicted as positive, and recall is calculated as the true positives divided by the total number of samples actually belonging to the positive class. Finally, specificity determines the efficacy of the model in identifying the negative class and is computed as the fraction of true negatives to the sum of true negatives and false positives (Sokolova et al., 2006; Sokolova and Lapalme, 2009).

The ROC curve is another technique for studying the performance of a classifier in which the relationship between the recall (true-positive rate) and the specificity (true-negative rate) is analyzed at different probability thresholds (Lachiche and Flach, 2003; Fawcett, 2004; Sokolova et al., 2006). Computing the area under the ROC curve (AUC) provides an estimate of the average performance of the ROC curve into a single value. In general, AUC values range from 0.5 (random guessing; bad performance) to 1.0 (excellent performance) (Fawcett, 2004).

In Table 2.1, I show the best five combinations of seismic attributes obtained after running and analyzing the results from the exhaustive PNN algorithm testing a suite of smoothing parameters ranging from $0.05 \leq r \leq 3.5$ with $\Delta r = 0.05$. I note that these combinations of attributes show values of accuracy, precision, recall, specificity, and AUC

above 98% representing excellent performance when distinguishing between salt and nonsalt seismic facies.

Also, the minimum validation error (E_V) in combinations 1, 2, and 4 was obtained using a smoothing parameter $r = 0.1$, whereas combinations 3 and 5 obtained a better performance when using a smoothing parameter of $r = 0.15$ because there is an increase in the gap between the training and validation errors associated with overfitting of the model when using smaller values of r.

When analyzing combinations 1, 2, and 3, I select combination 1, which is composed of the coherence, GLCM contrast, total energy, and dip deviation attributes, and I select smoothing parameter $r = 0.1$ as the best combination for differentiating between salt and nonsalt seismic facies in the Eugene Island seismic survey because, using only four seismic attributes, it provides the minimum validation (E_V) error and a balanced bias-variance trade-off. Moreover, this combination shows excellent performance during the classification associated with high values of accuracy, precision, recall, specificity, and AUC.

In Figure 2.8a, I show the learning curve associated with combination 1. I observe that using values of $r > 0.1$ results in relatively high training (E_T) and validation (E_V) errors possibly associated with the model underfitting the data. In contrast, when the smoothing parameter is equal to $r = 0.05$, E_T and E_V change from 0.01223 and 0.01689 to 0.00324 and 0.02032 respectively. This rapid decrease in E_T and increase in E_V indicates that the model is overfitting the data leading to a decrease in performance when classifying new unseen data. In Figure 2.8b, I show the ROC curve for combination 1, where the diagonal blue line represents a random guess classifier that does not have information to distinguish between

facies (Fawcett, 2004). I note that combination 1 shows a high true-positive rate, a low false-positive rate, and an AUC close to 1.0, indicating that the model can correctly differentiate between salt from nonsalt seismic facies.

In Figure 2.9, I show the results obtained after applying the exhaustive PNN using the coherence, GLCM contrast, total energy, and dip deviation attributes, and smoothing parameter r equal to 0.1 to the Eugene Island survey. The PNN facies prediction corendered with the seismic amplitude along inline 391 (Figure 2.9a), shows that, in general, the neural network classifies correctly between salt (purple facies; red arrow) and nonsalt seismic facies (the green facies).

However, some salt classification gaps associated with coherent migration artifacts are visible inside salt diapir 1 (the blue arrows). These features are not classified as salt because they have a different seismic pattern that is closer to those of valid reflections from the conformal sediments. In contrast, some low-amplitude discontinuities related to normal faults in the area (the yellow arrow) and missing or noisy data in the edges of the survey with little interpretational value (the red rectangle) are misclassified as salt (the purple facies). The data quality plays an important role in voxel-by-voxel classification algorithms. In contrast, a human interpreter would be able to put such features in their proper geologic and/or seismic data quality context (Posamentier and Kolla, 2003).

Figure 2.9b shows the PNN facies prediction corendered with the seismic amplitude volume along time slice $t = 1.78$ s. Note that the salt diapir 1 (the red arrow) is correctly classified by the exhaustive PNN algorithm. In addition, salt diapir 2 used as a test data set

is also correctly classified by the proposed algorithm as salt facies (purple facies; the red arrow).

Finally, in Figure 2.9c and 2.9d, I examine the PNN salt probability volume along inline 391 and time slice $t = 1.78$ s. I observe that the extracted purple facies in salt diapir 1 and salt diapir 2 are classified as salt with very high probabilities meaning that the proposed algorithm has high performance when distinguishing between the salt and the surrounding geology.

Correlation analysis

To analyze the relationship between the candidate attributes, I evaluate their correlation heatmap using the training and validation data sets (Figures 2.10 and 2.11). To quantitatively assess their correlation, I examine the Pearson's and Spearman's rank correlations. The Pearson (1984) correlation measures the linear dependence between the features, whereas the Spearman (1904) rank correlation evaluates linear or nonlinear positive and negative relationships using a monotonic function. From Figures 2.10 and 2.11, I analyze the correlations between attribute pairs associated with combination 1 (the green rectangles). The absolute Pearson's correlation and Spearman's rank correlations vary from 0.44 to 0.95 and 0.63 and 0.97, respectively, in the training data set, whereas, in the validation data set, the absolute Pearson's correlation varies from 0.52 to 0.95 and the Spearman's rank correlation ranges from 0.73 to 0.97. I also note that the coherence attribute has a high correlation with GLCM contrast and dip deviation.

In Figures 2.10 and 2.11, I also note that GLCM contrast and GLCM dissimilarity show a very high average Pearson's and rank correlations of 0.99 making them almost

24

perfectly correlated. I note that when the exhaustive PNN uses them together (Table 2.1, combination 2) the validation error (Ev) of the neural network increases.

According to Guyon and Elisseeff (2003), redundant attributes are characterized by a perfect correlation; thus, adding them to an ML architecture should not provide any additional information. However, if two attributes show a very high correlation, they can complement each other to provide better class separation. Guyon and Elisseeff (2003) suggest that irrelevant attributes by themselves can be more valuable if they are combined with others. Therefore, I hypothesize that highly correlated attributes can complement each other because the performance of the classifier increases when they are used together. Kim et al. (2019) find that using correlated attributes provided superior classifications in noisier parts of the data.

To test my hypothesis, I analyze the facies predictions using two highly correlated attributes - dip deviation and coherence, which show absolute Pearson's and rank correlations of 0.9 and 0.65, respectively. Mathematically, I know these two attributes are independent, with coherence mapping lateral changes in waveform, and dip deviation measuring lateral and vertical changes in dip. For the two seismic facies used in my training data – salt and conformal sediments - these two attributes are statistically correlated. To test whether using both attributes is useful, I compute the seismic facies volume using only the dip deviation and then I compare this volume with the results obtained using dip deviation and coherence together.

From the exhaustive PNN workflow, I determined that the optimal smoothing parameter r when using only dip deviation is $r = 0.05$ because it provides the lowest $Ev =$

0.1046, whereas when using the combination of dip deviation and coherence, the optimal r

is equal to 0.2 with a validation error of $E_V = 0.029$, which represents a 72% decrease in the

validation error compared to the result obtained using only the dip deviation as input

attribute. Moreover, when using only the dip deviation as input, the accuracy, precision,

recall, specificity, and AUC of the classification are equal to 0.937, 0.894, 0.997, 0.872, and

0.9475, respectively, whereas while using the dip deviation and coherence I obtain accuracy

= 0.983, precision = 0.979, recall = 0.988, specificity = 0.9781, and AUC = 0.9971.

Therefore, the latter combination shows an increase in the accuracy, precision, specificity,

and AUC of the results.

In Figure 2.12a, I analyze the PNN facies prediction corendered with the seismic

amplitude along inline 391 using the dip deviation as the input attribute and a smoothing

parameter of $r = 0.05$. I note that the neural network does a good job of classifying the salt

and nonsalt seismic facies. However, there are several gaps inside salt diapir 1 (the blue

arrows) that were misclassified as nonsalt seismic facies by the algorithm. In addition, areas

near normal faults (the yellow arrow) and noisy data (the red rectangle) are misclassified as

salt.

Figure 2.12b shows the PNN facies prediction for the same line using the

combination of dip deviation and coherence attributes and smoothing parameter $r = 0.2$.

Misclassifications within the salt are reduced to one large gap (the blue arrow) corresponding

to the coherent noise indicated by the blue arrow in Figure 2.1, whereas outside the salt,

misclassifications associated with normal faults (the yellow arrow) and noisy areas near the

edges of the seismic volume (the red rectangle) are diminished.

In Figure 2.13a and 2.13b, I compare the PNN facies prediction using only the dip deviation against the facies prediction volume using dip deviation and coherence at time slice $t = 1.78$ s. I observe that when using two seismic attributes, there is a better delineation of the edges of the salt diapir 1 (the blue arrows). However, on both examples, the model tends to overestimate the size of the salt diapirs by classifying some of the surrounding conformal sediments as salt. Finally, salt diapir 2 looks better defined internally (the yellow arrows) when using the dip deviation and coherence as input attributes.

Although the dip deviation and coherence show a high correlation between each other, I observe in Figures 2.12 and 2.13 that these attributes complement each other resulting in better class separation in the multiattribute space when differentiating between salt and nonsalt seismic facies in the Eugene Island seismic survey.

Facies prediction using an optimal subset versus all candidate seismic attributes

To further assess the effectiveness of the exhaustive PNN workflow, I compare the facies prediction volume when taking all the candidate seismic attributes and the subset of attributes composed of the coherence, GLCM contrast, total energy, and dip deviation as input in the neural network for performing the seismic facies classification.

In Figure 2.14, I show the learning curve when using all of the candidate attributes as input. I note that for $r > 0.45$, the model shows high training (E_T) and validation (E_V) errors possibly associated with underfitting, whereas when using values of $r < 0.45$, there is a large gap between the training (E_T) and validation (E_V) errors indicating that the model is overfitting the data. I hypothesize that the increasing gap between these errors might be

27

associated with the Hughes phenomenon (Hughes, 1968) due to the increasing number of attributes used as input.

To perform an unbiased comparison, I consider two possible cases when computing the seismic facies volume using all seven candidate seismic attributes. Case 1 consists of selecting the smallest validation error giving by $E\text{v} = 0.01977$ and $r = 0.2$ without considering the large gap existing between the validation and training errors. Case 2 tries to minimize the gap between the training and validation errors. Here, I select $r = 0.45$ as the optimal smoothing parameter because it provides training and validation errors that are closer to each other ($E_\text{V} = 0.02325$ and $E_\text{T} = 0.02322$).

In both cases, I note that there is an increase in the validation error ranging from 14.6 to 27.4% and a decrease in the accuracy, precision, recall, and specificity compared to the results obtained using the exhaustive PNN attribute subset.

In Figure 2.15, I show the comparison of the PNN facies prediction volumes corendered with the seismic amplitude along inline 391 considering case 1 (Figure 2.15a), case 2 (Figure 2.15b), and the exhaustive PNN attribute subset (Figure 2.15c). In general, I note that salt diapir 1 shows a similar internal response and only minor changes in the edge definition (the blue arrows). Therefore, including more attributes do not provide any significant change or improvement in the facies prediction. However, cases 1 and 2 show an increase of voxels associated with normal faults (the yellow arrows) and seismic noise (the red rectangle), being misclassified as salt seismic facies compared to the results obtained using the exhaustive PNN attribute subset.

Analyzing the PNN facies prediction corendered with the seismic amplitude volume

at $t = 1.78$ s for case 1, case 2, and the attribute subset selected using the exhaustive PNN

workflow (Figure 2.16), I still observe that salt diapir 1 does not show any significant change

when including more attributes as input in the algorithm. However, when studying salt diapir

2, which is used as test data set to assess the performance of the model when classifying

unseen data, I note that the result obtained using the exhaustive PNN attribute subset (Figure

2.16c) displays a better internal result compare to the facies volumes obtained in cases 1 and

2 (Figures 2.16a and 2.16b) in which salt diapir 2 has more gaps possibly associated with

coherent migration artifacts being misclassified as nonsalt seismic facies (the yellow

arrows).

Finally, from the results obtained after applying the exhaustive PNN algorithm, I

note that from seven input candidate attributes, a suite of four seismic attributes composed

of coherence, GLCM contrast, total energy, and dip deviation are the best combination to

distinguish between salt and nonsalt seismic facies. I can quantitatively show that this

combination generates a more robust, simpler, less computationally expensive model that

avoids the Hughes (1968) phenomenon while removing irrelevant attributes that do not

contribute to making a better model.

Application of the Adam optimization technique

To overcome the limitation associated with the exhaustive search algorithm in which

a fixed smoothing parameter *r* is used, I implement an optional step in the exhaustive PNN

workflow that consists of applying the Adam optimization technique to find a distinct

smoothing parameter for each seismic attribute for further improving the performance of the

neural network when using the best combination of attributes given by the coherence, GLCM contrast, total energy, and dip deviation.

Adam is a computationally efficient first-order gradient stochastic optimization technique that computes adaptive learning rates from the first and second moments of the gradients. Therefore, it provides robust results when facing large data sets, noisy or sparse gradients, and nonstationary problems (Kingma and Ba, 2015).

For selecting a suite of smoothing parameters r's to be used as starting point in the Adam optimization technique, I implement a random initialization approach to guarantee symmetry-breaking during training with values ranging from 0.05 to 0.15 because from the exhaustive search algorithm I determine that a smoothing parameter close to 0.1 is providing the highest accuracy (Figure 2.8).

Figure 2.17 shows the validation error at different iterations during the implementation of the Adam algorithm. I observe that the minimum validation error (E_V) obtained is equal to 0.01627 associated with iteration 15th and smoothing parameters equal to 0.065, 0.075, 0.104, 0.222, respectively. This new E_V is smaller than the E_V using a fixed smoothing parameter of 0.1 for all seismic attributes in combination 1. Moreover, I note an improvement in the performance evaluation metrics after implementing Adam.

Finally, I also compute the training error (E_T) using the new suite of smoothing parameters at iteration 15 (Figure 2.17). I observe that E_T is equal to 0.01266; thus, it guarantees that I am obtaining a balanced bias-variance trade-off model after implementing Adam.

In Figure 2.18, I show the results when applying the exhaustive PNN using different smoothing parameters for each seismic attribute in combination 1 after implementing Adam along inline 391. I note that the neural network is still correctly classifying between the salt (purple facies; red arrow) and the background geology (the green facies). Moreover, the flanks of the salt diapir (the orange arrows) are better delineated than the results obtained when using a fixed smoothing parameter (Figure 2.18a). In addition, low-amplitude discontinuities related to normal faults are no longer classified as salt when applying Adam (the yellow arrow). However, gaps associated with coherent migration artifacts inside salt diapir 1 and noisy data in the edges of the survey are still misclassified by the algorithm.

In Figure 2.18b, I examine the PNN facies prediction after applying Adam corendered with the seismic amplitude volume along time slice 1.78 s. I observe that both salt diapirs are still correctly classified by the proposed workflow. Moreover, salt diapir 2, which is used as test data, looks better defined than when using the same smoothing parameter for each seismic attribute in combination 1.

Finally, analyzing the PNN salt probability volume along inline 391 (Figure 2.18c) and time slice 1.78 s (Figure 2.18d), I observe that the purple facies associated with salt diapir 1 shows an internal increase in the probabilities (the green arrow), whereas salt diapir 2 still show high probabilities during the classification; thus, by applying Adam in the exhaustive PNN algorithm I can improve the performance of my model when differentiating between salt and nonsalt seismic facies in the Eugene Island seismic volume.

Geobody extraction

To obtain a 3D distribution of the salt diapirs present in the Eugene Island seismic survey and isolate them from the surrounding conformal reflectors, I perform a geobody extraction (Meyer et al., 2001) to model and extract the voxels from my PNN facies prediction and PNN salt probability volumes computed using the optimal combination of attributes given by coherence, GLCM contrast, total energy, and dip deviation and a suite of smoothing parameters for each of these attributes after applying Adam.

In Figure 2.19, I show the 3D salt mapping using as criterion voxels characterized by salt facies with probabilities higher than 75%. I note that I am able to extract with high accuracy the salt diapirs 1 and 2 (purples facies; the red arrows) from the surrounding geology. I also observe that salt diapir 2, which is used as testing data set in this study, shows some gaps (the blue arrow), which I hypothesize are associated with misclassified salt facies as background geology or salt voxels that show probabilities lower than 75% due to the presence of crossing coherent migration artifacts. Salt diapir 1 is well defined internally with salt voxels being classified with very high confidence (Figure 2.18c) by the exhaustive PNN algorithm.

Computational effort

The Eugene Island data volume used in this study consisted of 700 inlines, 700 crosslines, and 750 vertical samples, giving a total of 367.5 million voxels. The polygons constructed on the seven inlines provided 28,500 training and 5500 validation voxels. Using 60 processors on an Intel workstation, the time for the exhaustive search algorithm to find

the best of 127 attribute combinations was 23.5 min. After training found the best combination to be four attributes, the final classification took 2.6 h.

Conclusion

Application of exhaustive PNN to a 3D Gulf of Mexico seismic survey proved to be a powerful tool in selecting the optimal combination of seismic attributes to perform a supervised seismic facies classification to distinguish between salt and nonsalt seismic facies. Coupling an exhaustive search algorithm together with a PNN, I determine that from seven input candidate attributes, the best combination is given by using only four attributes composed of the coherence, GLCM contrast, total energy, and dip deviation with a smoothing parameter r of 0.1. Moreover, applying a first-order gradient optimization technique called Adam, I can further improve the performance of the proposed algorithm by finding different smoothing parameters for each of the seismic attributes while maintaining a balanced bias-variance trade-off. Because a high correlation between attributes does not necessarily imply that they are redundant, and they might complement each other providing better class separation, I found that my proposed workflow can generate a simpler, more robust, less computationally expensive model by removing irrelevant attributes while maintaining attributes that can complement each other. Furthermore, the occurrence of the Hughes phenomenon is reduced after performing the attribute selection workflow. Finally, a geobody extraction is conducted to delineate the 3D distribution of the salt diapirs and isolate them from nonsalt seismic facies. Using the seismic classification results obtained from Adam and looking for voxels characterized by salt facies with probabilities higher than 75%, I extract salt diapirs 1 and 2 (the purples facies) from the surrounding geology with

high accuracy. In general, salt diapir 2, used as test data set in this study, is well-defined although some gaps are visible possibly related to misclassification or low confidence values due to the presence of crossing coherent migration artifacts. Salt diapir 1 is better internally defined than salt diapir 2 because salt voxels are classified with higher confidence by the exhaustive PNN algorithm.

Acknowledgments

Appendix A

Preprocessing for the exhaustive PNN algorithm

Seismic attributes often have different units of measurement and ranges of values. For example, coherence ranges from 0 to 1, whereas the seismic envelope may range between 0 and +10000, thereby requiring normalization to balance their contribution to any subsequent classification. Following Walden (1985), Honorio et al. (2014), and Lubo-Robles and Marfurt (2019), I know that, in general, seismic attributes are characterized by super-Gaussian distributions whereas other attributes such as coherence and spectral magnitude components show a Poisson distribution about 0, or for coherence, bias towards 1. In this

paper, I perform a simple, but robust scaling that avoids knowledge of the detailed distribution and is resistant to the presence of outliers given by:

$$a_m^{scaled} = \frac{a_m - q_{2m}}{q_{3m} - q_{1m}}, \tag{A1}$$

where each attribute is centered about their median q_2, and is scaled by the IQR given by the difference between q_3 and q_1, which are the 75th and 25th percentiles. The robust scaling percentiles are computed from the training data and are used to scale the training, validation, and testing data sets.

The PNN algorithm for finding different smoothing parameters

To find a different smoothing parameter r for each seismic attribute, I need to compute the derivatives of the continuous error function with respect to the smoothing parameters (Masters, 1995). Then, using these derivatives together with a first-order optimization technique such as Adam, I update the smoothing parameters to minimize the error.

Masters (1995) computes the derivative of the error function for a single sample in the validation. In this study, I am interested in minimizing the global error E. Therefore, I generalize Masters (1995) to compute the derivative of the global continuous error E given by

$$\frac{\partial E}{\partial r_i} = \frac{1}{H}\sum_{h=1}^{H}\{2[P_k(x)-1][\frac{\partial P_k(x)}{\partial r_i}] + 2\sum_{j\neq k}[P_j(x)\frac{\partial P_j(x)}{\partial r_i}]\}, \tag{A2}$$

where

$$\frac{\partial P_k(x)}{\partial r_i} = \frac{\frac{1}{N_k}\left\{\left[2\sum_{n=1}^{N_k}\delta_{kn}e^{-\sum_{m=1}^{M}\frac{(x_m-a_{nm}^{scaled})^2}{r_i^2}}\right]\frac{(x_m-a^{scaled})^2}{r_i^3}\right\} - \left[\sum_{k=1}^{K}\frac{1}{N_k}\left\{\left[2\sum_{n=1}^{N_k}\delta_{kn}e^{-\sum_{m=1}^{M}\frac{(x_m-a_{nm}^{scaled})^2}{r_i^2}}\right]\frac{(x_m-a^{scaled})^2}{r_i^3}\right\}\right]P_k(x)}{\sum_K\left[\frac{1}{N_k}\sum_{n=1}^{N_k}\delta_{kn}e^{-\sum_{m=1}^{M}\frac{(x_m-a_{nm}^{scaled})^2}{r_i^2}}\right]}$$

<div align="right">(A3)</div>

where P represents the normalized probabilities given by the estimated density function of each class k divided by the sum of all the density functions of all classes, K represent the total number of classes, H the number of samples in the validation data set, and δ_{nk} is the Kronecker delta function.

Then, following Kingma and Ba (2015) and using the derivative of the continuous error functions $\frac{\partial E}{\partial r_i}$, I apply the first-order gradient stochastic optimization algorithm called Adam that uses adaptive learning rates by computing the first and second moments of the gradients. The learning rule is given by:

$$r_i^+ = r_i - \frac{\alpha\,\widehat{m}_t}{\sqrt{\widehat{v}_t} + e}$$

<div align="right">(A4)</div>

where, t is the current iteration of a user-defined total number of iterations T, r_i^+ is the updated smoothing parameter for each attribute, r_i is the smoothing parameter of the previous iteration, and $\widehat{m}_t$ and $\widehat{v}_t$ are the bias-corrected first and second moment estimation of the gradient $\frac{\partial E}{\partial r_i}$ (equation A2). The Adam algorithm also uses hyperparameters for the step size α and a small constant e to avoid division by zero.

With this background, the bias-corrected first and second moment estimation (Kingma and Ba, 2015) are given by

$$\widehat{m}_t = \left[\beta_1 m_{t-1} + (1 - \beta_1)\frac{\partial E}{\partial r_{i_t}}\right] \bigg/ (1 - \beta_1^t) \tag{A5}$$

and,

$$\widehat{v}_t = \left[\beta_2 v_{t-1} + (1 - \beta_2)\frac{\partial E}{\partial r_{i_t}}^2\right] \bigg/ (1 - \beta_2^t) \tag{A6}$$

where β_1 and β_2 are also hyperparameters for the Adam algorithm. In the first iteration, $t = 0$, m_t, and v_t are initialized to zero. According to Kingma and Ba (2015), good default values for the hyperparameters are $\beta_1 = 0.9$, $\beta_2 = 0.999$, $\alpha = 0.001$, and $e = 10^{-8}$. However, in this paper, I use a step size $\alpha = 0.01$, which results in faster convergence with a reduced number of iterations, T, needed to decrease the validation error E_V.

References

Alexander, F., and P. Flemings, 1995, Geologic evolution of a Pliocene–Pleistocene salt-withdrawal minibasin: Eugene Island Block 330, Offshore Louisiana: AAPG Bulletin, **79**, 1737–1756, doi: 10.1306/7834DEEA-1721-11D7-8645000102C1865D.

Amin A., M. Deriche, M. A. Shafiq, Z. Wang, and G. AlRegib, 2017, Automated salt dome detection using an attribute ranking framework with a dictionary-based classifier: Interpretation, **5**, no. 3, SJ61-SJ79, doi: 10.1190/INT-2016-0084.1.

Angelo, S.M., M. Matos, and K.J. Marfurt, 2009, Integrated seismic texture segmentation and clustering analysis to improved delineation of reservoir geometry: 79th Annual International Meeting, SEG, Expanded Abstracts, 1107-1111, doi: 10.1190/1.3255046.

Barnes, A. E., 2007, Redundant and useless seismic attributes: Geophysics, **72**, no.3, P33–P38, doi: 10.1190/1.2716717.

Briscoe, E., and J. Feldman, 2010, Conceptual complexity and the bias/variance tradeoff: Cognition, **118**, 2-16, doi: 10.1016/j.cognition.2010.10.004.

Chang-kai Z., and L. Wen-kai, 2010, Seismic attributes selection based on SVM for hydrocarbon reservoir prediction, 80th Annual International Meeting, SEG, Expanded Abstracts, 1586-1590, doi: 10.1190/1.3513144.

Chopra, S., and K. J. Marfurt, 2007, Seismic attributes for prospect identification and reservoir characterization: SEG Geophysical Development Series 11.

Chopra, S., and K.J. Marfurt, 2014, Churning seismic attributes with principal component analysis: 84th Annual International Meeting, SEG, Expanded Abstract, 2672-2676, doi: 10.1190/segam2014-0235.1.

Di, H., and D. Gao, 2017, Nonlinear gray-level co-occurrence matrix texture analysis for improved seismic facies interpretation: Interpretation, **5**, no. 3, SJ31-SJ40, doi: 10.1190/INT-2016-0214.1.

Di H., M. A. Shafiq, and G. AlRegib, 2017, Seismic fault detection based on multi-attribute support vector machine analysis: 87th Annual International Meeting, SEG, Expanded Abstracts, 2039-2044, doi: 10.1190/segam2017-17748277.1.

Di H., M. A. Shafiq, Z. Wang, and G. AlRegib, 2019, Improving seismic fault detection by a super-attribute- based classification, Interpretation, **7**, no. 3, SE251-267, doi: 10.1190/INT-2018-0188.1.

Dorrington, K. P, and C. A. Link, 2004, Genetic-algorithm/neural-network approach to seismic attribute selection for well-log prediction: Geophysics, **69**, 212-221, doi: 10.1190/1.1649389

Fawcett, T., 2004, ROC graphs: Notes and practical considerations for researchers: Machine Learning, **31**, 1-38.

Galvis, I. S., Y. Villa, C. Duarte, D. Sierra, and W. Agudelo, 2017, Seismic attribute selection and clustering to detect and classify surface waves in multicomponent seismic data by using *k*-means algorithm: The Leading Edge, **36**, 239-248, doi: 10.1190/tle36030239.1.

Goodfellow I., Y. Bengio, and A. Courville, 2016, Deep Learning: MIT Press.

Guo, H., K. J. Marfurt, and J. Liu, 2009, Principal component spectral analysis: Geophysics, **74**, no. 4, P35–P43, doi: 10.1190/1.3119264.

Guyon, I., and A. Elisseeff, 2003, An introduction to variable and feature selection: Journal of Machine Learning Research, **3**, 1157–1182.

Hajmeer M., and I. Basheer, 2002, A probabilistic neural network approach for modeling and classification of bacterial growth/no-growth data: Journal of Microbiological Methods, **51**, 217-226, doi: 10.1016/S0167-7012(02)00080-5.

Hampson, D.P., J. S. Schuelke, and J. A Quirein, 2001, Use of multiattribute transforms to predict log properties from seismic data: Geophysics, **66**, 220- 236, doi: 10.1190/1.1444899.

Haralick, R. M., K. Shanmugam, and I. Dinstein, 1973, Textural features for image classification: IEEE Transactions on Systems, Man and Cybernetics, **SMC-3**, 610-621, doi: 10.1109/TSMC.1973.4309314.

Honorio, B., A. Sanchetta, E. Pereira, and A. Vidal, 2014, Independent component spectral analysis: Interpretation, **2**, no. 1, SA21-SA29, doi: 10.1190/INT-2013-0074.1.

Huber, P.J., 1981, Robust Statistics: John Wiley & Sons.

Hughes, G., 1968, On the mean accuracy of statistical pattern recognizers: IEEE Transactions on Information Theory, **14**, 55–63, doi: 10.1109/TIT.1968.1054102.

Jabbar H. K., and R. Z. Khan, 2015, Methods to avoid over-fitting and under-fitting in supervised machine learning (comparative study), Computer Science, Communication & Instrumentation Devices, 163-172.

Jones, I. F., and I. Davison, 2014, Seismic imaging in and around salt bodies: Interpretation, **2**, no. 4, SL1–SL20, doi: 10.1190/INT-2014-0033.1.

Joshi, A., and M. Appold, 2016, Potential of porosity waves for methane transport in the Eugene Island field of the Gulf of Mexico basin: Marine and Petroleum Geology, **75**, 1-13, doi: 10.1016/j.marpetgeo.2016.04.005.

Kim, Y., R. Hardisty, and K. J. Marfurt, 2019, Attribute selection in seismic facies classification: Application to a Gulf of Mexico 3D seismic survey and the Barnett Shale: Interpretation, **7**, no. 3, SE281–SE297, doi: 10.1190/INT-2018-0246.1.

Kingma, D., and J. L. Ba, 2015, Adam: A method for stochastic optimization: 3rd International Conference for Learning Representations, 1-15.

Lachiche, N., and P. Flach, 2003, Improving accuracy and cost of two-class and multi-class probabilistic classifiers using ROC curves: Proceedings of the 20th International Conferences on Machine Learning, 416-423.

Li, F., and W. Lu, 2014, Coherence attribute at different spectral scales: Interpretation, **2**, no. 1, SA99–SA106, doi: 10.1190/INT-2013-0089.1.

Long Z., Y. Alaudah, M.A. Qureshi, Y. Hu, Z. Wang, M. Alfarraj, G. AlRegib, A. Amin, M. Deriche, S. Al-Dharrab, and H. Di, 2018, A comparative study of texture attributes for characterizing subsurface structures in seismic volumes, Interpretation, **6**, no. 4., T1055-T1066, doi: 10.1190/INT-2017-0181.1.

Lubo-Robles, D., and K. J. Marfurt, 2019, Independent component analysis for reservoir geomorphology and unsupervised seismic facies classification in the Taranaki Basin, New Zealand: Interpretation, **7**, no. 3, SE19–SE42, doi: 10.1190/INT-2018-0109.1

Masters, T., 1995, Advanced algorithms for neural networks: John Wiley & Sons.

Meyer, D. E., E. L. Harvey, T. E. Bulloch, J. C. Voncannon, and T. M. Sheffield, 2001, Use of seismic attributes in 3-D geovolume interpretation: The Leading Edge, **20**, 1377–1400, doi: 10.1190/1.1486768.

Pearson, K., 1894, Contributions to the mathematical theory of evolution: Philosophical Transactions A, **185**, 71–110, doi: 10.1098/rspl.1893.0079.

Posamentier, H. W., and V. Kolla, 2003, Seismic geomorphology and stratigraphy of depositional elements in deep-water settings: Journal of Sedimentary Research, **73**, 367-388, doi: 10.1306/111302730367.

Qi, J., and J. P. Castagna, 2013, Application of a PCA fault-attribute and spectral decomposition in Barnett shale fault detection: 83rd Annual International Meeting, SEG, Expanded Abstracts, 1421–1425, doi: 10.1190/segam2013-0674.1.

Qi, J., T. Lin, T. Zhao, F. Li, and K. J. Marfurt, 2016, Semisupervised multiattribute seismic facies analysis: Interpretation, **4**, no. 1, SB91-SB106, doi: 10.1190/INT-2015-0098.1

Qi, J., and K. Marfurt, 2019, Nonparallelism attributes and data adaptive Kuwahara image processing: 89th Annual International Meeting, SEG, Expanded Abstracts, 1858-1861, doi: 10.1190/segam2019-3216022.1.

Qi, J., B. Zhang, B. Lyu, and K. Marfurt, 2020, Seismic attribute selection for machine-learning-based facies analysis: Geophysics, **85**, no. 2, O17-O35, doi: 10.1190/geo2019-0223.1.

Roden, R., T. Smith, and D. Sacrey, 2015, Geologic pattern recognition from seismic attributes: Principal component analysis and self-organizing maps: Interpretation, **3**, no. 4, SAE59–SAE83, doi: 10.1190/INT-2015-0037.1.

Roy A., A. S. Romero-Peláez, T. J. Kwiatkowski, and K. J. Marfurt, 2014, Generative topographic mapping for seismic facies estimation of a carbonate wash, Veracruz

Basin, southern Mexico: Interpretation, **2**, no. 1, SA31-SA47, doi: 10.1190/INT-2013-0077.1.

Sokolova M., N. Japkowicz, and S. Szpakowicz, 2006, Beyond accuracy, F-score and ROC: A family of discriminant measures for performance evaluation: Australian Joint Conference on Artificial Intelligence, 1015-1021, doi: 10.1007/11941439_114

Sokolova, M., and G. Lapalme, 2009, A systematic analysis of performance measures for classification tasks: Information Processing and Management, **45**, 427-437, doi: 10.1016/j.ipm.2009.03.002

Spearman, C., 1904, The proof and measurement of association between two things: American Journal of Psychology, **15**, 72–101, doi: 10.2307/1412159.

Specht, D. F., 1990, Probabilistic neural networks: Neural Networks, **3**, 109-118, doi: 10.1016/0893-6080(90)90049-Q

Walden, A.T., 1985, Non-Gaussian reflectivity, entropy, and deconvolution: Geophysics, **50**, 2862–2888, doi: 10.1190/1.1441905.

Wang, Z., C. Yin, X. Lei, F. Gu, and J. Gao, 2015, Joint rough sets and Karhunen-Loève transform approach to seismic attribute selection for porosity prediction in a Chinese sandstone reservoir: Interpretation, **3**, no. 4, SAE19–SAE28, doi:10.1190/INT-2014-0268.1.

Wrona, T., I. Pan, R. L. Gawthorpe, and H. Fossen, 2018, Seismic facies analysis using machine learning, Geophysics, **83**, no. 5, O83-O95, doi: 10.1190/geo2017-0595.1.

Wu X., L. Liang, Y. Shi, and S. Fomel, 2019, FaultSeg3D: Using synthetic data sets to train an end-to-end convolutional neural network for 3D seismic fault segmentation: Geophysics, **84**, no.3, IM35-IM45, doi: 10.1190/geo2018-0646.1.

Zhao, T., V. Jayaram, A. Roy, and K. J. Marfurt, 2015, A comparison of classification techniques for seismic facies recognition: Interpretation, **3**, no. 4, SAE29–SAE58, doi: 10.1190/INT-2015-0044.1.

Zhao, T., F. Li, and K. J. Marfurt, 2018, Seismic attribute selection for unsupervised seismic facies analysis using user-guided data-adaptive weights: Geophysics, **83**, no. 2, O31–O44, doi: 10.1190/geo2017-0192.1.

Chapter 2 Figures
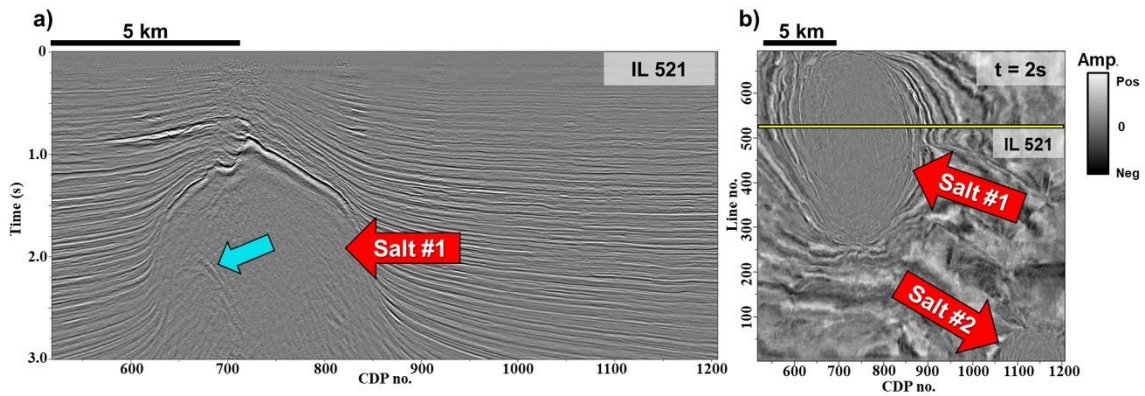
Figure 2.1. Eugene Island seismic survey. (a) Vertical slice along inline 521. Salt diapir 1 is characterized by low-amplitude, discontinuous reflectors. Crossing coherent migration artifacts (the blue arrow) are also visible inside salt diapir 1. (b) Representative time slice at t = 2 s. Another salt diapir (salt diapir 2) also characterized by low-amplitude, discontinuous reflectors is visible in the seismic survey.
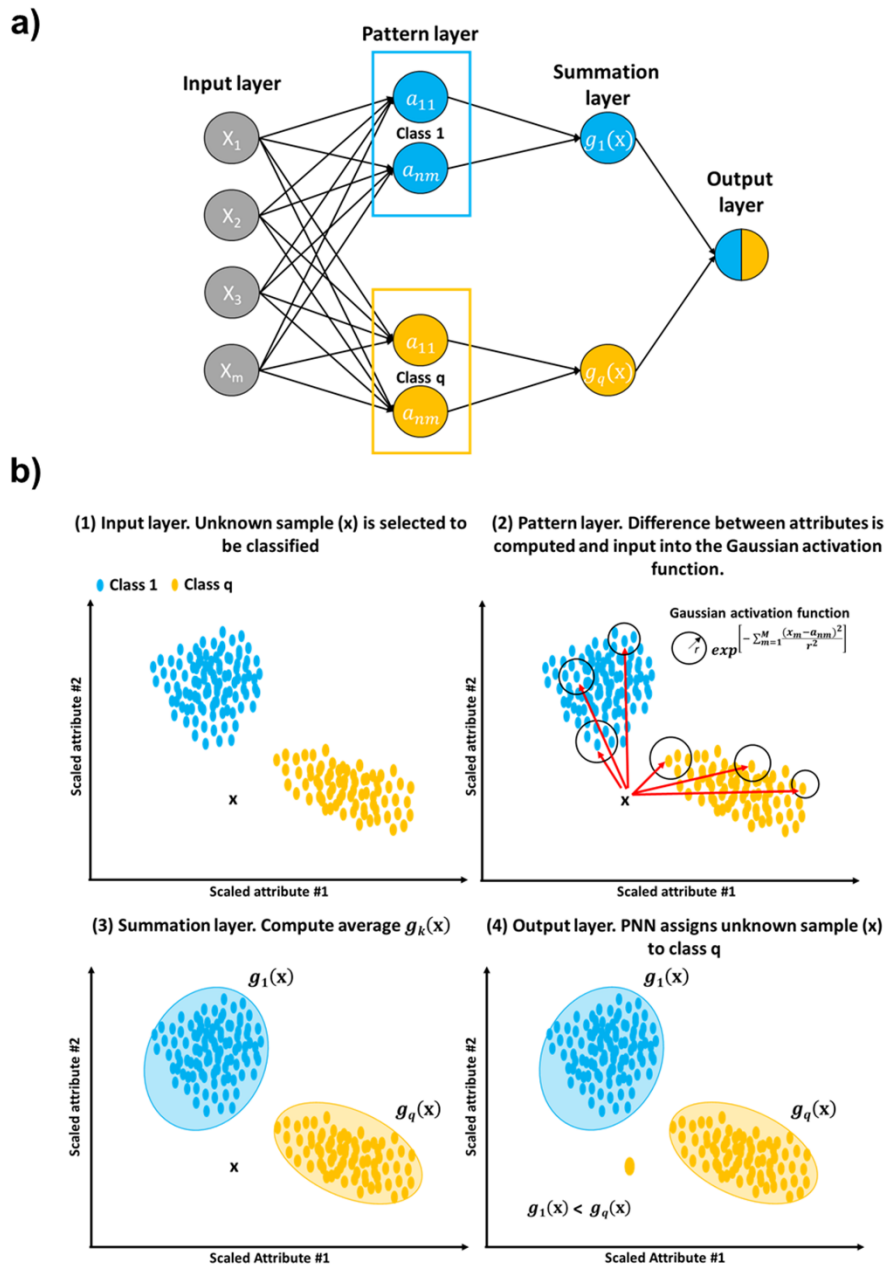
Figure 2.2. PNN framework (a). The PNN is composed of four layers: (1) input layer, (2) pattern layer, (3) summation layer, and (4) output layer. (b) First, an unlabeled sample **x** is selected for classification. The PNN computes the difference between the input sample and the training attributes **a** and applies a Gaussian activation function. Finally, the average estimated density function $g_k(x)$ for each class is computed, and the unlabeled sample **x** is assigned to the class where $g_k(x)$ is maximum.
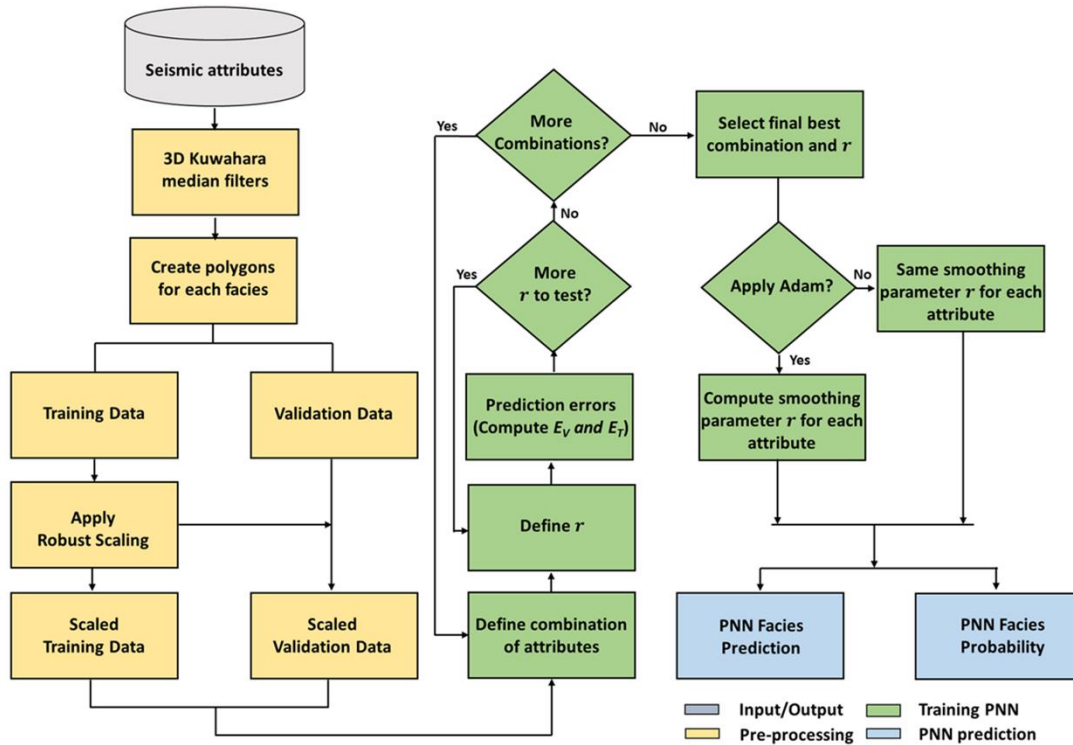
Figure 2.3. Exhaustive PNN workflow. First, I select a suite of candidate seismic attributes based on my geological insight and experience. Also, a 3D Kuwahara filter is applied to block and smooth the seismic attributes' response (Qi et al., 2016). Next, I generate the training and validation data sets by manually selecting a suite of polygons enclosing each target seismic facies. Moreover, a robust scaling scheme is applied to avoid any bias associated with different units between the seismic attributes. Then, I perform an exhaustive search and test all possible combination of seismic attributes with smoothing parameter r ranging from 0.05 to 3.5 and $\Delta r = 0.05$. These combinations are ranked based on their validation error (E_V), and the best combination of seismic attribute and smoothing parameter r is given by the smallest E_V while maintaining a balanced bias-variance trade-off. As an optional step, a first-order gradient optimization technique called Adam (Kingma and Ba, 2015) can be applied to the best combination to relax the fixed smoothing parameter r condition imposed by the exhaustive search algorithm and further minimize the validation error. Finally, using the exhaustive PNN attribute subset, I perform my supervised seismic facies classification, and I compute the probability of each class, which measures the confidence in the classification.
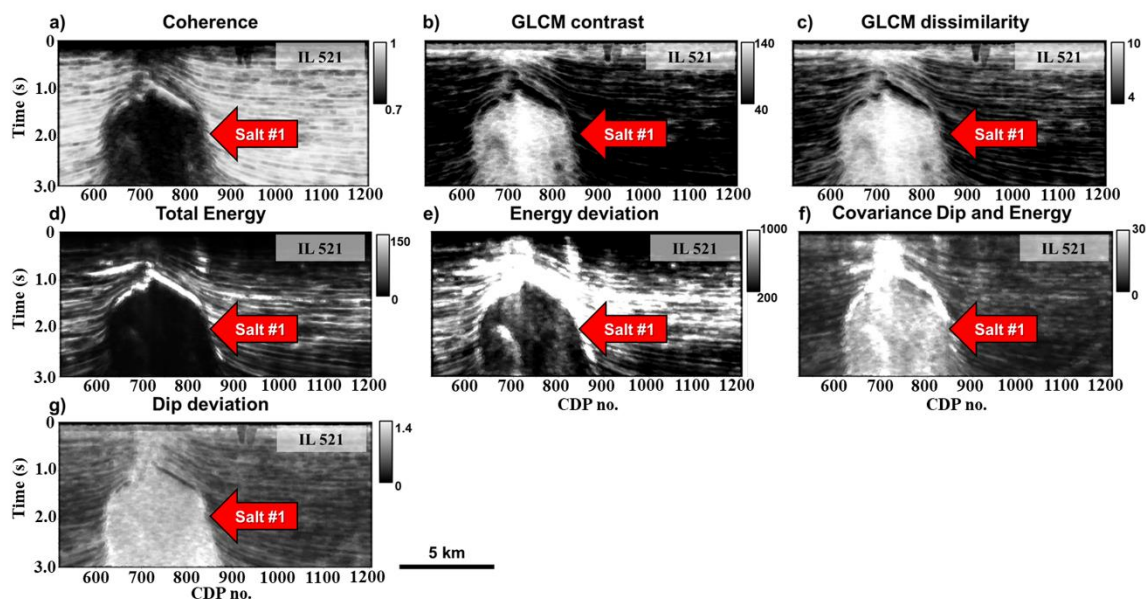
Figure 2.4. Candidate attributes to be used as input in the exhaustive search algorithm selected based on my geological insight. (a) Coherence, (b) GLCM contrast, (c) GLCM dissimilarity, (d) total energy, (e) energy deviation, (f) covariance dip and energy, (g) dip deviation. The selected candidate attributes show different responses when comparing the salt diapir (the red arrow) against the more coherent, higher amplitude background geology. A 3D Kuwahara filter (Qi et al., 2016) is applied to smooth the internal response and sharpen the edges of the salt diapir to improve the discrimination between salt and the nonsalt seismic facies during classification.

45
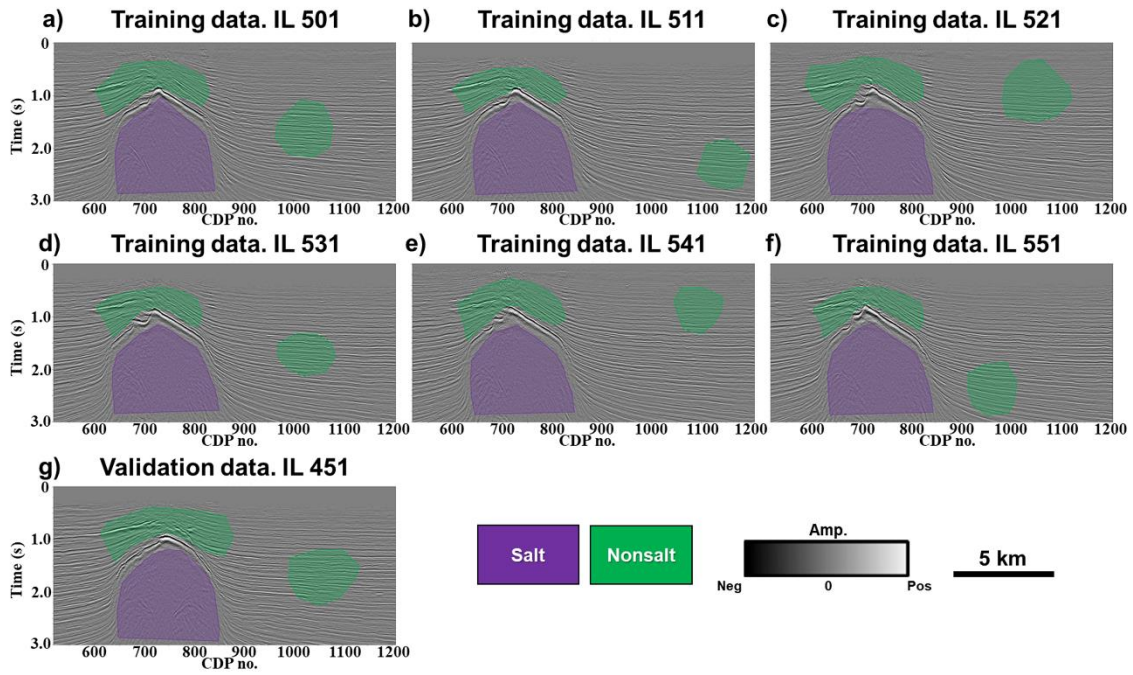
Figure 2.5. Training and validation data sets definition. (a-f) The training data sets consists of a suite of manually picked polygons from inline 501 to 551 with a 10 inline interval enclosing the salt (the purple polygons) and nonsalt seismic facies (the green polygons). (g) Validation data set enclosing the target facies along inline 451.
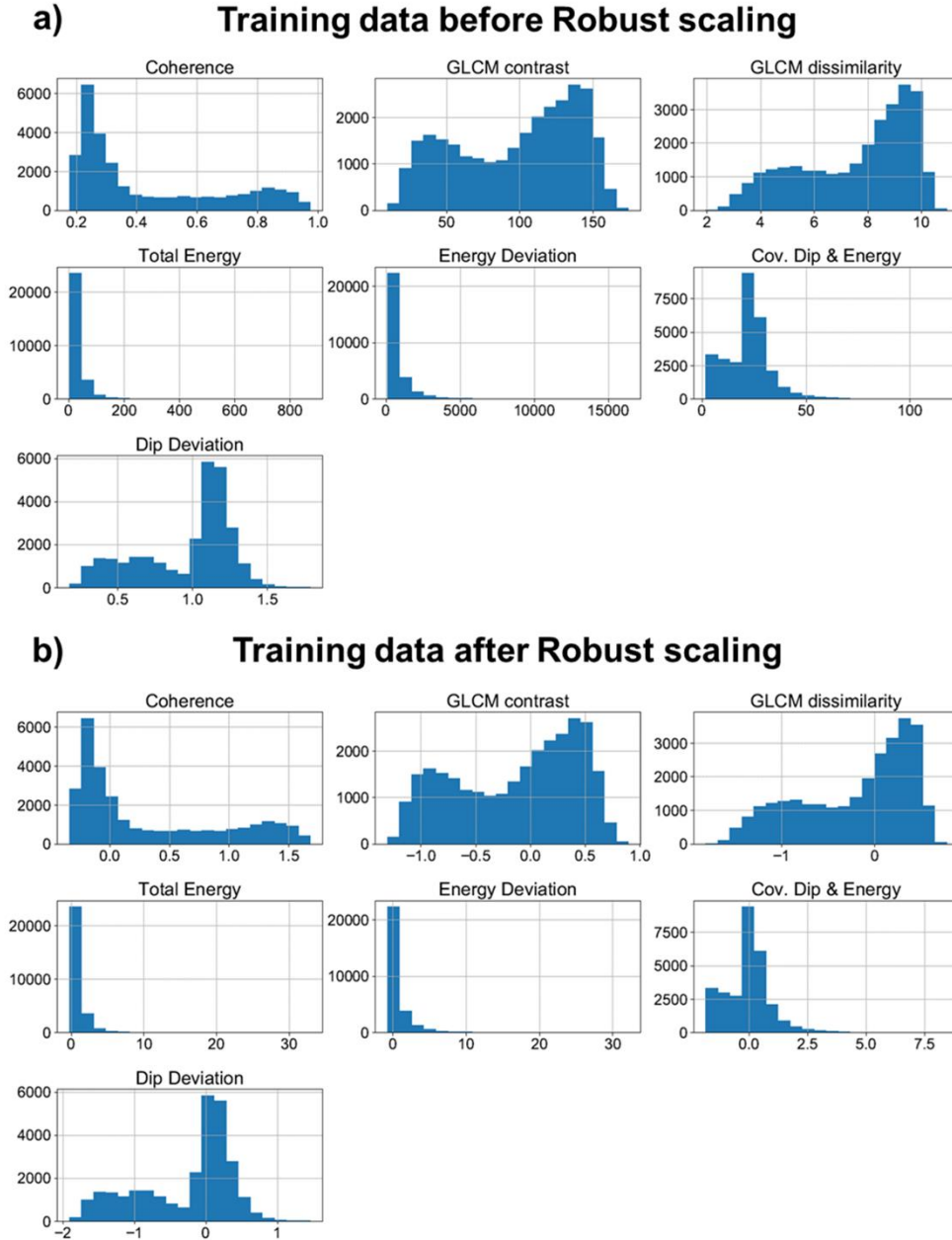
Figure 2.6. Histograms of the training data set (a) before and (b) after robust scaling. The shape of the distributions is maintained after scaling. Candidate attributes show non-Gaussian distributions. Therefore, a robust scaling scheme represents a better approach than Z-score normalization.
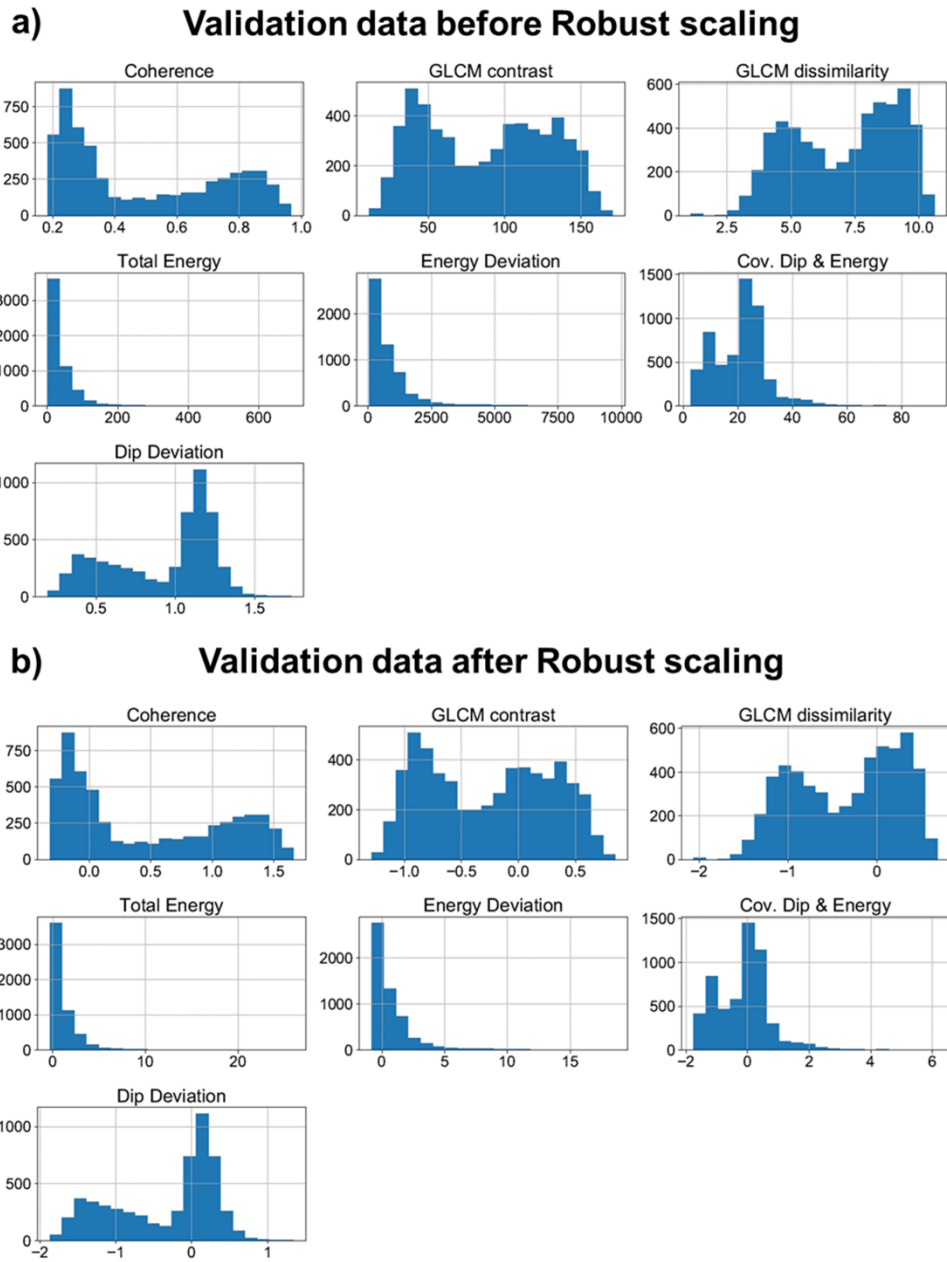
Figure 2.7. Histograms of the validation data set (a) before and (b) after robust scaling. The shape of the distributions is maintained after robust scaling. Distributions of the candidate seismic attributes in the training and validation data sets are very similar; thus, the same intrinsic patterns are captured on both data sets.
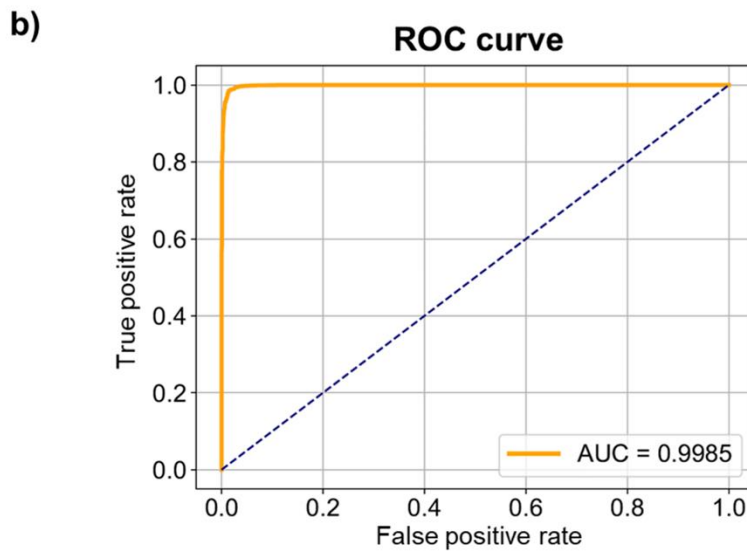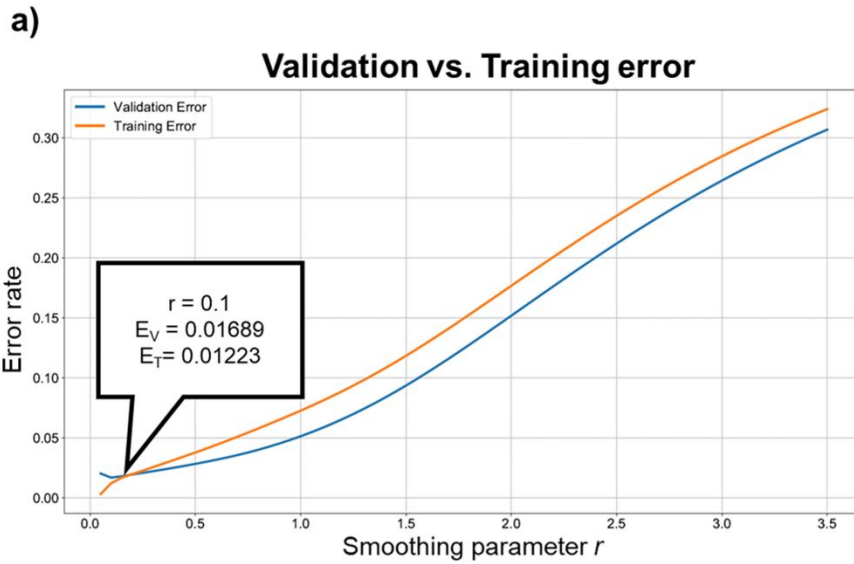
Figure 2.8. (a) Learning curve of combination 1 composed of the coherence, GLCM contrast, total energy, and dip deviation attributes. The ideal smoothing parameter is given by $r = 0.1$. For $r \geq 0.1$, the training (E_T) and validation (E_V) errors are high, possibly implying underfitting. When $r = 0.05$, there is a rapid decrease in E_T and increase in E_V, suggesting overfitting. (b) ROC curve for combination 1. The diagonal blue line represents a random guess classifier that does not distinguish between facies correctly (Fawcett, 2004). Combination 1 shows an AUC close to 1.0 and high true-positive and low false-positive rates implying that the classifier can correctly distinguish salt from the background geology.
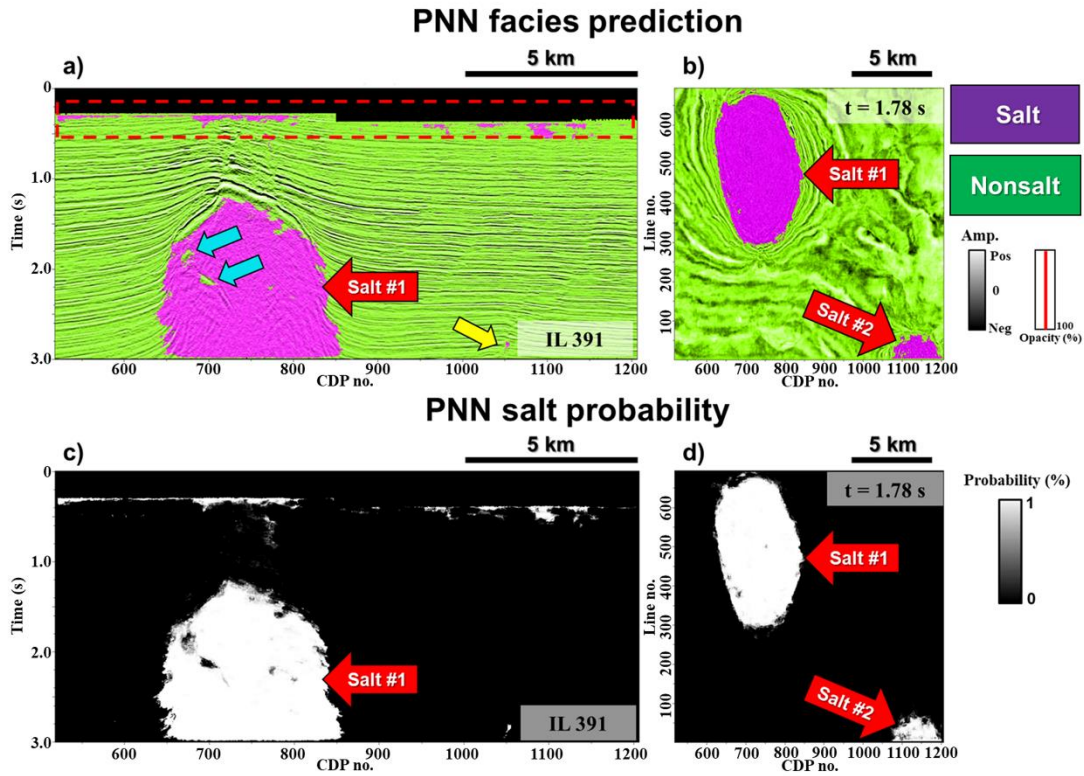
Figure 2.9. PNN facies prediction corendered with the seismic amplitude (a) along inline 391, and (b) at time slice t = 1.78 s. The PNN correctly distinguishes between salt (purple facies; red arrow) and nonsalt seismic facies (the green facies). Also, some voxels associated with coherent migration artifacts (the blue arrows), low-amplitude discontinuities related to normal faults (the yellow arrow), and missing or noisy data in the edges of the survey (the red rectangle) tend to be misclassified as salt (the purple facies). Note that salt diapir 2, which is used as a test data set, is also correctly classified as salt seismic facies by the algorithm (purple facies; the red arrow). PNN facies probability volume (c) along inline 391, and (d) at time slice t = 1.78 s. The extracted purple facies (salt diapirs 1 and 2) show very high probabilities associated with a high performance by the model when differentiating between salt and nonsalt seismic facies.
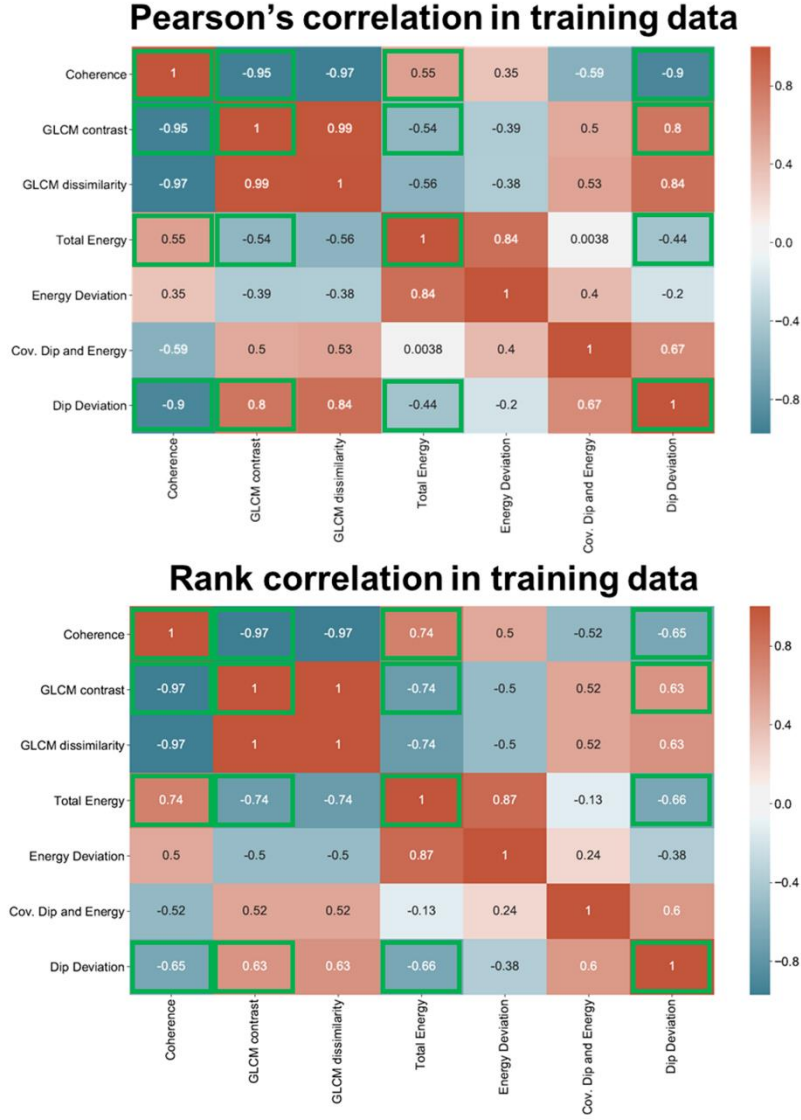
Figure 2.10. Correlation heat map of the training data set. The absolute Pearson's and rank correlations vary from 0.44 to 0.95 and 0.63 and 0.97, respectively, in combination 1. Note that the coherence attribute has a high correlation with the GLCM contrast and dip deviation. Following Guyon and Elisseeff (2003), I hypothesize that high correlated attributes can complement each other because using them together improves the performance of the neural networks when differentiating between salt and nonsalt seismic facies.
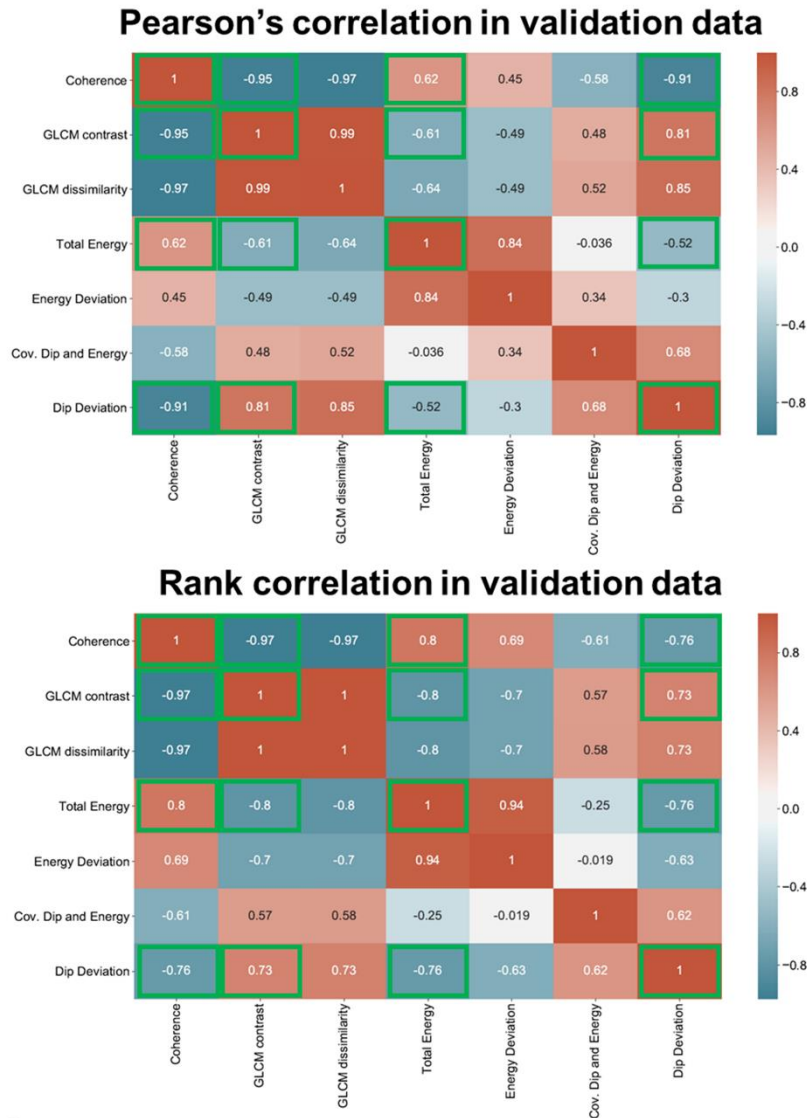
Figure 2.11. Correlation heat map of the validation data set. The absolute Pearson's correlation varies from 0.52 to 0.95, and the Spearman's rank correlation ranges from 0.73 to 0.97 in combination 1. Similar to the correlations obtained from the training data set, the coherence still shows a high correlation with the GLCM contrast and the dip deviation seismic attributes.
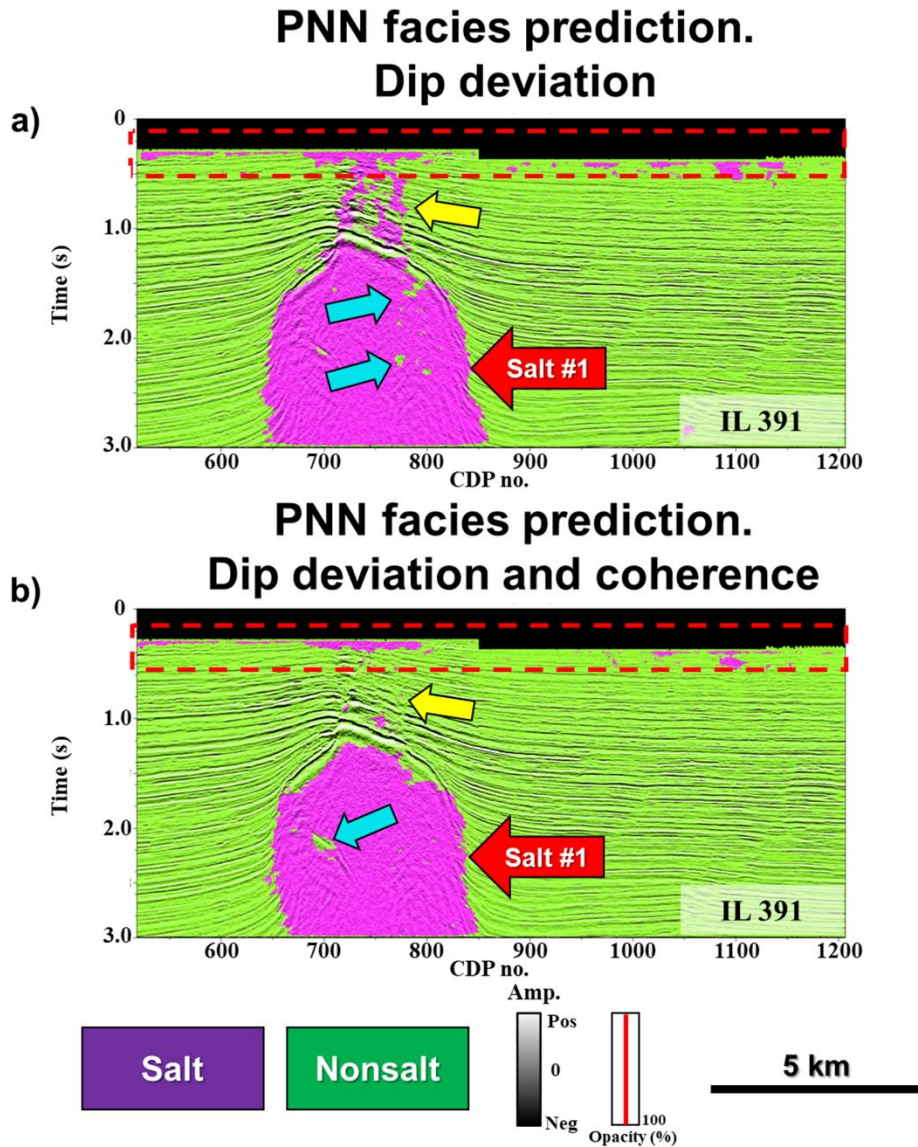
Figure 2.12. PNN facies prediction corendered with the seismic amplitude along inline 391 using (a) dip deviation and (b) dip deviation and coherence as input attributes. In general, the PNN correctly classifies between salt and nonsalt seismic facies. Voxels associated with coherent noise (the blue arrows), normal faults (the yellow arrows), and noisy areas (the red rectangle) that tend to be misclassified as salt are diminished when using the combination of dip deviation and coherence as input compared to the results obtained when using only dip deviation. Note that, although dip deviation and coherence have a high correlation, they complement each other, which results in a better seismic facies classification.
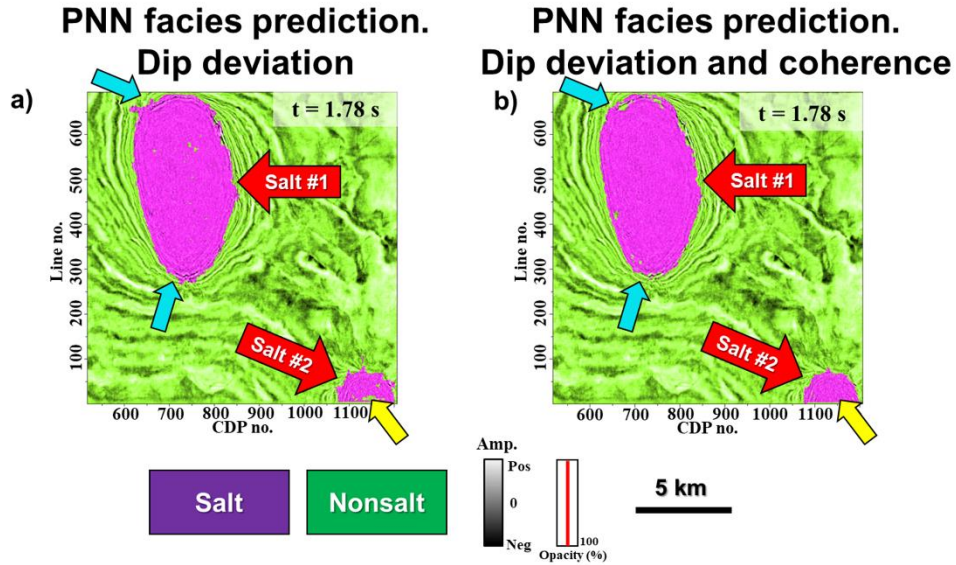
Figure 2.13. PNN facies prediction corendered with the seismic amplitude at time slice $t = 1.78$ s using (a) dip deviation and (b) dip deviation and coherence as input attributes. When using dip deviation and coherence as input, salt diapir 2 shows a better internal definition (the yellow arrows), whereas salt diapir 1 has a better delineation of its edges (the blue arrows). Note that on both examples, the size of the salt diapirs is overestimated because the models tend to classify some conformal sediments as the salt seismic facies.

Validation vs. Training error. All candidate attributes
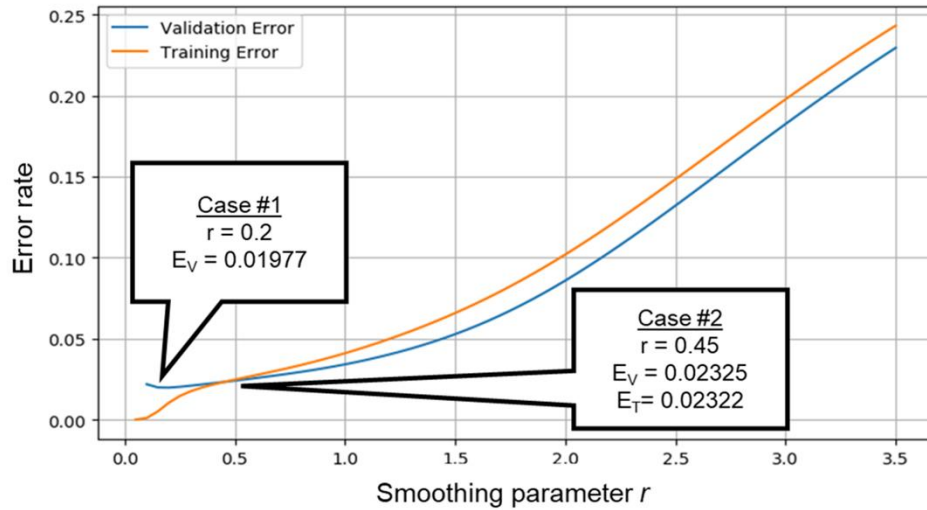
Attributes	r	Accuracy	Recall	Precision	Specifity	AUC
All seven candidate attributes	0.2	0.9878	0.9944	0.9824	0.9807	0.9986
All seven candidate attributes	0.45	0.9856	0.9944	0.9784	0.9762	0.998

Figure 2.14. Learning curve when using all of the candidate attributes as input. For $r > 0.45$, the model shows high training (E_T) and validation (E_V) errors possibly implying underfitting, while for $r < 0.45$, there is a large gap between the errors leading to overfitting possibly related to the Hughes phenomenon (Hughes, 1968). Two cases are generated for analysis: case 1, which is associated with the smallest validation error (E_V), and case 2, which minimizes the gap between the training and validation errors.
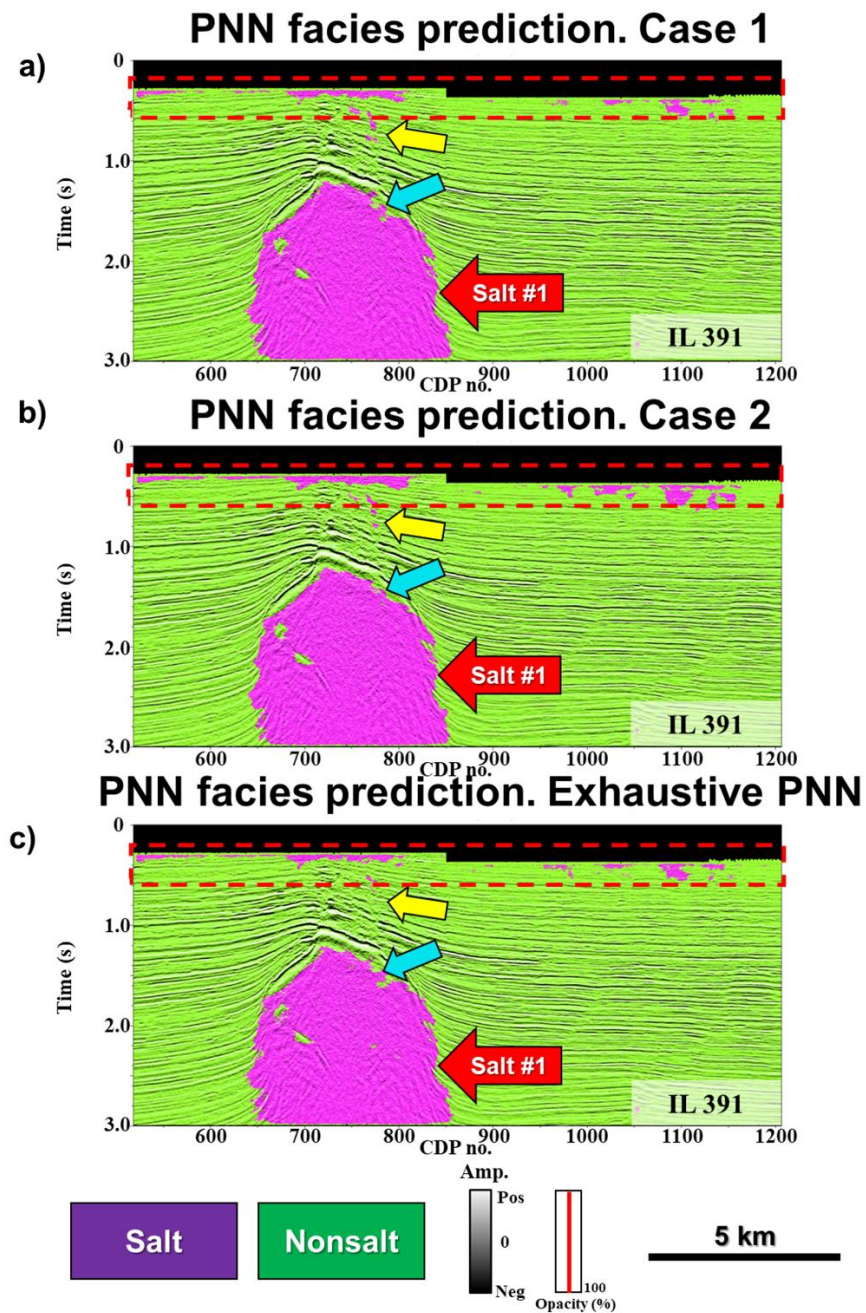
Figure 2.15. PNN facies prediction volumes corendered with the seismic amplitude along inline 391 for (a) case 1, (b) case 2, and (c) exhaustive PNN attribute subset used as input. Note that including more attributes do not show any significant change or improvement in the seismic facies classification (the blue arrows). Moreover, when using the exhaustive PNN attribute subset as input, I observe less voxels related to seismic noise (the red rectangle) and normal faults (the yellow arrows) being misclassified as salt.
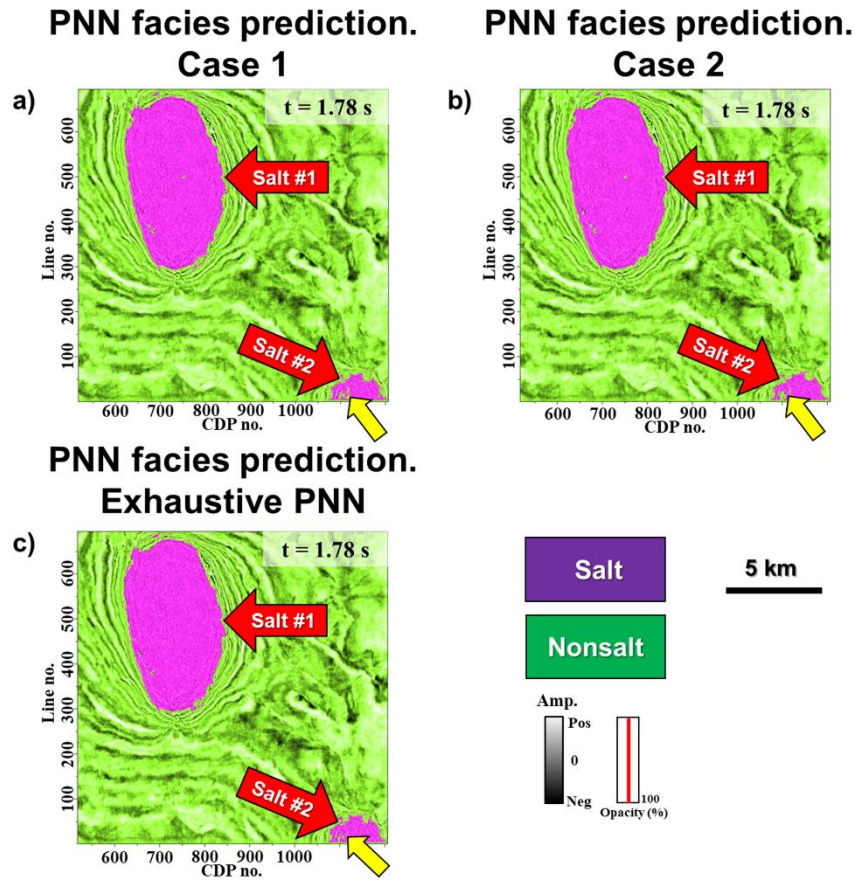
Figure 2.16. PNN facies prediction corendered with the seismic amplitude volume at time slice *t* = 1.78 s for (a) case 1, (b) case 2, and (c) exhaustive PNN attribute subset. Note that the results obtained using the exhaustive PNN attribute subset shows a better internal definition of salt diapir 2, whereas salt diapir 1 does not show any significant change or improvement if more attributes are included. Therefore, using the exhaustive PNN algorithm, I can remove irrelevant attributes and generate a more robust, simpler classifier to perform my seismic facies classification.

Validation error. Adam implementation

Combination	Attributes	r	E_V	E_T	Accuracy (%)	Precision (%)	Recall (%)	Specificity (%)	AUC
1	Coherence, GLCM contrast, total energy, dip deviation.	[0.065 0.075 0.104 0.222]	0.01627	0.01266	98.98	98.58	99.48	98.45	0.9988
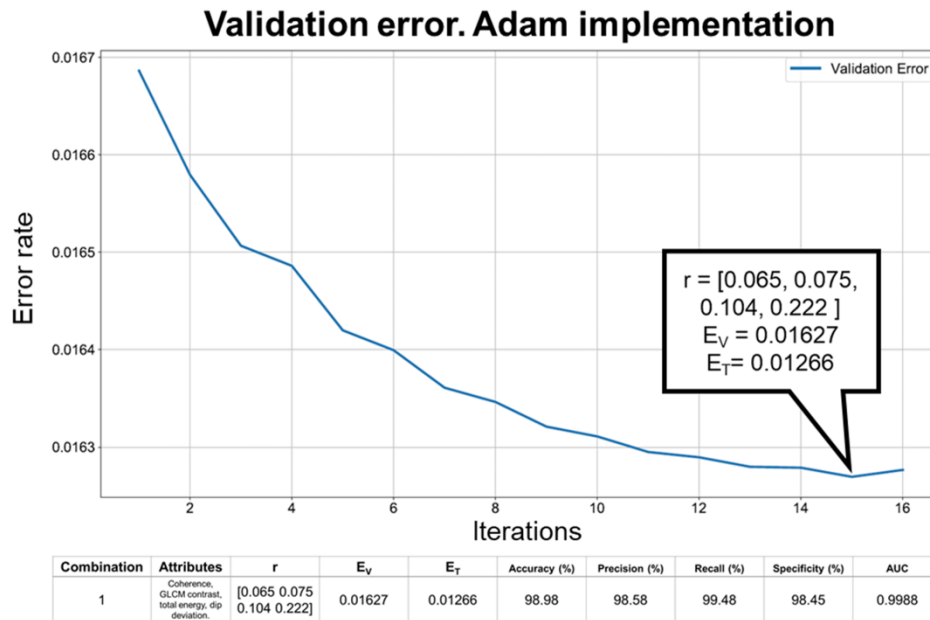
Figure 2.17. Validation error during the implementation of the Adam algorithm. The minimum validation error $E_V = 0.01627$ is obtained at iteration 15th and smoothing parameters r's equal to 0.065, 0.075, 0.104, 0.222. Note that by relaxing the fixed smoothing parameter condition, there is a decrease in the validation error (E_V) and an increase in the evaluation metrics of the model. Finally, at iteration 15th, $E_T = 0.01266$, which guarantees a balanced bias-variance trade-off.
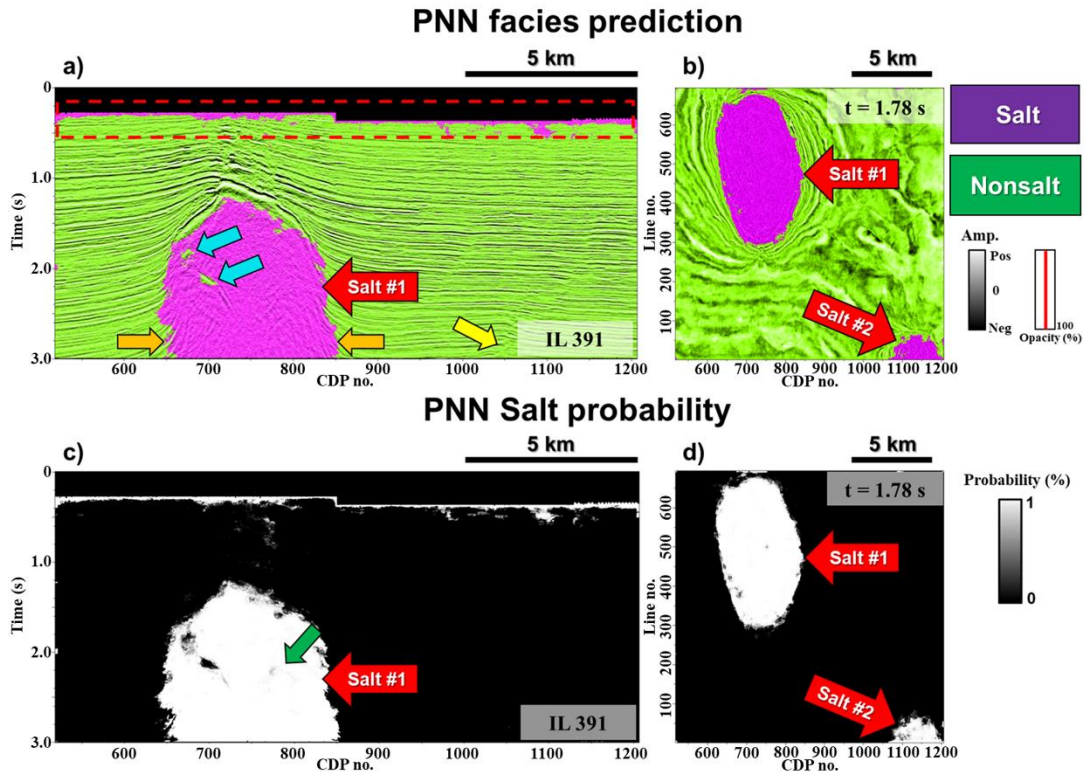
Figure 2.18. PNN facies prediction using Adam corendered with the seismic amplitude (a) along inline 391 and (b) at time slice *t* = 1.78 s. The PNN is still correctly classifying between salt (purple facies; the red arrow) and nonsalt seismic facies (the green facies). Flanks of salt diapir 1 are better delineated, whereas salt diapir 2, which is used as test data set, is correctly classified and has better definition compared to the results obtained using a fixed smoothing parameter *r* for each seismic attribute in combination 1. However, some voxels associated with coherent noise (the blue arrows) and seismic noise towards the edges of the survey (the red rectangle) are still being misclassified as salt. PNN facies probability volume using Adam (c) along inline 391 and (d) at time slice 1.78 s. Salt diapir 1 shows an internal increase in the probabilities (the green arrow), whereas salt diapir 2 still shows high probabilities during the classification.
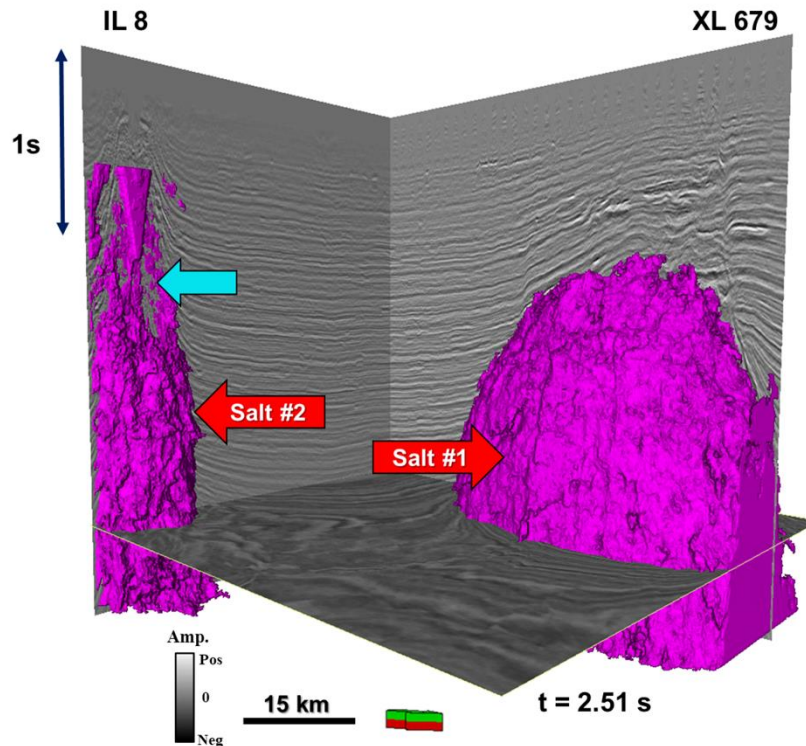
Figure 2.19. Geobody generation extracting salt facies from the PNN facies prediction volume with probabilities higher than 75% obtained from the PNN salt probability volume. Salt diapirs 1 and 2 (purples facies; the red arrows) are extracted with high accuracy from the surrounding conformal reflectors. However, salt diapir 2, which is used as test data set to assess the performance of the classifier, shows some gaps (the blue arrow) possibly related to salt facies misclassified as background geology or salt voxels that show probabilities lower than 75%.

Chapter 2 Tables

Combination	Attributes	r	E_V	E_T	Accuracy (%)	Precision (%)	Recall (%)	Specificity (%)	AUC
1	Coherence, GLCM contrast, total energy, dip deviation.	0.1	0.01689	0.01223	98.91	98.45	99.48	98.3	0.9985
2	Coherence, GLCM contrast, GLCM dissimilarity, total energy, dip deviation.	0.1	0.01693	0.0109	98.93	98.45	99.51	98.3	0.9984
3	Coherence, GLCM contrast, total energy, energy deviation, dip deviation.	0.15	0.01712	0.01167	98.93	98.35	99.62	98.19	0.9985
4	Coherence, GLCM dissimilarity, total energy, dip deviation.	0.1	0.01723	0.01261	98.93	98.48	99.48	98.3	0.9985
5	Coherence, GLCM contrast, GLCM dissimilarity, total energy, energy deviation, dip deviation.	0.15	0.01724	0.01058	98.89	98.31	99.6	98.15	0.9984

Table 2.1. The best five combinations of seismic attributes obtained after running and interpreting the results from the exhaustive PNN algorithm testing a suite of smoothing parameters ranging from $0.05 \leq r \leq 3.5$ with $\Delta r = 0.05$. These combinations show performance evaluation metrics above 98% associated with excellent classifiers. I select combination 1 composed of coherence, GLCM contrast, total energy, and dip deviation attributes, and I select smoothing parameter $r = 0.1$ as the best combination because it has the minimum validation error (E_V), a balanced bias-variance trade-off, and excellent performance evaluation metrics.

Chapter 3: Quantifying the sensitivity of seismic facies classification to seismic attribute selection: An explainable machine-learning study*

Abstract

During the past two decades, geoscientists have used machine learning (ML) to produce a more quantitative reservoir characterization and discover hidden patterns in their data. However, as the complexity of these models increases, the sensitivity of their results to the choice of the input data becomes more challenging. Measuring how the model uses the input data to perform either a classification or regression task provides an understanding of the data-to-geology relationships which indicates how confident I am in the prediction. To provide such insight, the ML community has developed local interpretable model-agnostic explanations (LIME) and Shapley additive explanations (SHAP) tools. In this study, I train a random forest architecture using a suite of seismic attributes as input to differentiate among mass transport deposits (MTDs), salt, and conformal siliciclastic sediments in a Gulf of Mexico data set. I apply SHAP to understand how the model uses the input seismic attributes to identify target seismic facies and examine in what manner variations in the input, such as adding band-limited random noise or applying a Kuwahara filter, impact the model predictions. During my global analysis, I find that the attribute

importance is dynamic, and it changes based on the quality of the seismic attributes and the seismic facies analyzed. For my data volume and target facies, attributes measuring changes in dip and energy show the largest importance for all cases in my sensitivity analysis. I note that to discriminate between the seismic facies, the ML architecture learns a "set of rules" in multiattribute space, and that overlap among MTDs, salt, and conformal sediments might exist based on the seismic attribute analyzed. Finally, using SHAP at a voxel scale, I understand why certain areas of interest were misclassified by the algorithm and perform an in-context interpretation to analyze how changes in the geology impacted the model predictions.

Introduction

Advances in machine-learning (ML) techniques have been increasingly exploited for better reservoir characterization including analyzing changes in seismic facies, predict well-log properties, and detecting faults among other tasks (Hampson et al., 2001; Dorrington and Link, 2004; Roy et al., 2014; Roden et al., 2015; Zhao et al., 2015; Lubo-Robles and Marfurt 2019; Lubo-Robles et al., 2021; Wu et al., 2019; Qi et al., 2020). Although the applications are promising, ML still lacks interpretability. Specifically, one should be able to identify features or attributes that are significant and, more importantly, address the degree to which the output is sensitive to various input attributes.

One of the key questions in interactive and ML interpretation is which combination of attributes is best to differentiate one seismic facies from another. There have been a few studies that have addressed the optimal subset of seismic attributes to perform seismic facies classification. Dimensionality reduction using principal component analysis (PCA) and

independent component analysis allows identification of a lower-dimensional statistically representative set of features in the data (Guo et al. 2009; Honorio et al. 2014; Roden et al. 2015; Lubo-Robles and Marfurt, 2019). Another approach by Chang-kai and Wen-kai (2010) uses support vector machine (SVM) to define weights to each input seismic attribute to generate a smaller subset of attributes useful to identify reservoir facies in their study area.

Using information theory, Amin et al. (2017) determine optimal attributes to use as input to detect salt domes, whereas Wang et al. (2015) apply PCA and joint rough sets to select the optimal attributes for porosity estimation. Kim et al. (2019) apply a suite of filters, wrappers, and embedded attribute selection techniques to determine relevant attributes and reject redundant attributes to increase the performance of the seismic facies classification and reduce its computational cost. Qi et al. (2020) develop a semisupervised approach consisting of applying Gaussian mixture models (GMM) and Bhattacharyya distance to determine the optimal combination of seismic attributes that maximizes the separation between seismic facies. Then, Qi et al. (2020) use this optimal subset as input into a generative topographic mapping (GTM) algorithm to perform a seismic facies classification. Lubo-Robles et al. (2021) couple an exhaustive search algorithm with a probabilistic neural network (PNN) to test all possible combinations of attributes, reject irrelevant attributes, reduce computational cost, and determine the optimal combination of seismic attributes to differentiate between salt and the background siliciclastic sediments in a Gulf of Mexico data set.

However, finding statistically representative features in the data or determining the set of optimal seismic attributes to use as input for seismic facies classification generally

does not map the inputs to the outputs in a manner that allows for easy interpretation of the predictive strength of each of the inputs. To overcome this limitation, local interpretable model-agnostic explanations (LIME), partial dependency plots, individual conditional expectations, and permutation feature importance have been developed in the ML community to get insight and interpret how ML models work (Ribeiro et al., 2016; Molnar, 2021)

Recently, Lundberg and Lee (2017) introduce a new approach, Shapley additive explanations (SHAP), based on Shapley values from game theory that provides local and global explanations for the model and represents the only explainable ML method with a unique solution and properties such as local accuracy, missingness, and consistency throughout the whole data set.

In the oil and gas industry, researchers have started applying SHAP to better understand unconventional reservoirs. Lerza et al. (2020) and Qian et al. (2020) use SHAP to identify which are the most important parameters impacting the estimated ultimate recovery (EUR) of the Vaca Muerta Formation and the Wolfcamp A Formation in the Neuquén Basin (northern Patagonia, Argentina) and Permian Delaware Basin, respectively. Cross et al. (2020c) apply PCA to reduce dimensionality of their input data and SHAP to derive the rock quality index (RQI) and analyze changes in the oil and water production (Cross et al., 2020a, 2020b), whereas Sathaye et al. (2020) apply SHAP to study how features such as proppant per fluid, fluid per foot, geologic components, and well spacing and timing parameters impact the production streams over time. Tran et al. (2020) use real-time drilling

data to infer formation properties and use SHAP values to interpret the relationship between the input drilling variables and the mechanical properties of the formation.

However, to the best of my knowledge, the use of SHAP values in the context of seismic facies classification is lacking in published literature. This paper demonstrates the use of SHAP values to study the impact of a suite of candidate seismic attributes in the prediction of seismic facies. The objectives of this research can be summarized as follows: (1) develop a random forest model for seismic facies classification to identify MTDs, salt, and the background conformal sediments in a Gulf of Mexico data set; (2) apply SHAP to understand the contribution of each of the seismic attributes in the predictions; (3) compute the global importance for each candidate seismic attribute; (4) perform a sensitivity analysis to the addition of band-limited noise or application of a Kuwahara filter for preconditioning the input seismic attributes for subsequent classification; and (5) use SHAP values to perform an in-context interpretation to study how variations in the seismic response affect the model's facies predictions.

I begin my paper with a summary of the SHAP implementation. I also describe the candidate seismic attributes selected as input for classification and generate three different cases for my sensitivity analysis consisting of (1) original seismic attributes, (2) the same attributes after Kuwahara median filtering to block and smooth their response, and (3) the same attributes computed from the seismic data with an additive 2:1 signal-to-noise level. Then, I manually define my training and validation data sets to define three seismic facies, irregular discontinuous reflectors, chaotic reflectors, and high-amplitude continuous

reflectors that represent MTDs, salt, and conformal sediments and perform a hyperparameter search to train and improve the accuracy of the model for classifying these seismic facies.

Then, I apply SHAP to understand and explain the global and local behavior of the model when distinguishing between the target seismic facies in a Gulf of Mexico data set. Finally, by corendering the SHAP values with the seismic amplitude volume, I perform an in-context interpretation to understand how changes in the geology, which are associated with changes in the seismic response, are related to the SHAP values and the model prediction. Appendix A provides mathematical details of adding band-limited random noise to the seismic volume.

Methods

Data set and seismic response of target facies

The 3D seismic survey is from the Gulf of Mexico, offshore Louisiana and covers an area of approximately 8000 km^2 (3089 mi^2) (Qi et al., 2016). The prestack time migrated volume was acquired by PGS, and it is characterized by a bin size of 37.5 x 25 m, sampling interval of 4 ms, and record length of 2 s (Qi et al., 2016, 2020; Kim et al., 2019). For my analysis, I crop the seismic volume into a subvolume consisting of 350 inlines, 841 crosslines, and same record length.

In Figure 3.1, I show the seismic amplitude volume along time slice at t=1.3s. I note the presence of lower amplitude chaotic seismic reflectors as compared with the surrounding sediments that are interpreted as two salt diapirs (the orange arrows). Moreover, the green rectangle encloses six equally spaced lines used to define my training and validation data

sets, whereas the vertical section GG' represents a test line used to interpret how my tree-based architecture generalizes in the presence of previously unseen, unlabeled data. Furthermore, I analyze the amplitude spectrum of my seismic data set (Figure 3.1b). I observe that the volume is characterized by a bandwidth of approximately 77.5 Hz with frequencies ranging from 2.5 Hz to 80 Hz.

Then, to interpret the seismic responses associated with my target seismic facies, I study the seismic amplitude volume along vertical section AA' and generate a suite of magnified vertical sections enclosing the seismic facies (Figure 3.2). I observe the presence of salt diapirs 1 and 2 together with irregular discontinuous reflectors interpreted as a suite of mass transport deposits (MTDs) (the green arrows). Moreover, these geologic features are enclosed by high-amplitude continuous reflectors interpreted as conformal sediments with highly variable dip depending on their proximity to the salt diapirs.

Magnifying salt diapir 1 (the orange rectangle), I note that it is characterized by low-amplitude, chaotic reflectors due to the presence of random incoherent noise. In addition, I observe the presence of crossing coherent noise (the yellow arrow) associated with migration artifacts due to the geometry of the salt and its higher P-wave velocity as compared with the surrounding formations (Jones and Davison, 2014).

Analyzing a magnified vertical section along one of the MTDs (the green rectangle), the MTDs tend to be highly heterogenous and characterized by intercalations of higher amplitude reflectors likely associated with more coherent rotated blocks (the red arrow) and more discontinuous, chaotic, lower amplitude reflectors, perhaps related to more shaley intervals (the blue arrow).

Finally, I study the seismic response of the conformal sediments (background formations). Magnified vertical section 1 (the purple rectangle) shows that, in general, conformal sediments are characterized by high-amplitude, coherent reflectors. However, analyzing magnified vertical section 2 (purple rectangle 2), I note a rapid change in amplitude and dips of these conformal sediments due to proximity of the salt., where they are characterized by a decrease in the quality of the seismic image and lower seismic amplitudes. Furthermore, I note the presence of low-frequency noise possibly associated with migration artifacts due to the proximity to the salt diapirs (the purple arrows).

SHAP

For linear or linearized inverse problems, geophysicists use approximations to the Hessian matrix to determine the sensitivity of an output prediction to an input parameter. To address a similar problem for ML, Lundberg and Lee (2017) developed the SHAP technique to determine why a specific ML model makes a certain prediction (Lundberg et al., 2018a).

SHAP estimates the Shapley values from cooperative game theory, thereby assigning each attribute an importance value based on its impact in the model prediction when the feature is present or not during the SHAP estimation (Lundberg and Lee, 2017; Lundberg et al., 2018a, 2020; Molnar, 2021). To explain complex models, SHAP uses a linear additive feature attribute method as a simpler explanation model:

$$f(a) = g(a') = \emptyset_0 + \sum_{j=1}^{J} \emptyset_j a_j' \tag{1}$$

where, $f(a)$ is the original ML model, $g(a')$ is the simpler linear explanation model, J is the number of simplified input seismic attributes, $\emptyset_j$ are the SHAP values measured across all

possible input permutations, a'_j is the simplified input vector that indicates if a particular

seismic attribute is present or not during the estimation, and $\emptyset_0$ is the base value, which is

computed when no input attribute is considered in the model prediction (Lundberg and Lee,

2017; Lundberg et al., 2018a; Molnar, 2021).

Workflow

To analyze how a tree-based architecture uses a suite of volumetric seismic attributes

to perform a seismic facies classification to distinguish between the three target facies of

interest, measure the importance of each seismic attribute, and conduct a sensitivity analysis

to evaluate how the interpretability of the ML architecture changes under different

perturbations made to the input attributes, I apply SHAP to a random forest architecture

considering three different cases. The cases are: (1) case 1 uses as input the seismic attributes

computed from my original seismic volume; (2) case 2 applies a 3D Kuwahara filter (Qi et

al., 2016; Lubo-Robles et al., 2021) to the original seismic attributes to precondition the

attributes for classification by removing noise, smooth the internal response of the seismic

facies, and sharpen the edges; and (3) case 3 adds band-limited additive white Gaussian noise

(AWGN) with a target signal-to-noise ratio (S/N) of 2 to the seismic volume and recomputes

the seismic attributes while maintaining the same parameters used to compute the attributes

in case 1 (Figure 3.3).

To differentiate between chaotic facies, irregular discontinuous, and parallel to

subparallel continuous reflectors, seismic attributes that measure changes in continuity,

morphology, frequency, and reflector dip and energy should be analyzed. Therefore, I select

coherence, total energy, gray-level co-occurrence matrix (GLCM) entropy, reflector

convergence, spectral bandwidth, GLCM contrast, and nonparallelism attributes such as dip deviation, energy deviation, and covariance of dip and energy gradient as input attributes for my ML model.

Then, I pick a suite of polygons on six coarsely spaced lines enclosing each of the target seismic facies to make the training and validation data sets used for the model generation. In the learning phase of the classifier, these supervised data labeled by the interpreter were split into two parts, with approximately 80% of the voxels belonging to the training data set, and the remaining 20% of the voxels belonging to the validation data, which represent only 0.006% of the seismic volume.

In addition, to remove scale dependency and because seismic attributes are characterized by Poisson or super-Gaussian distributions (Walden 1985; Honorio et al., 2014; Lubo-Robles et al., 2021), I scale my data using a Min-Max scaler (Jain et al., 2005; Pedregosa et al., 2011) in which the scaling parameters are computed only from the training data and are used to scale the training and validation data sets.

Next, considering only the original seismic attributes associated with case 1, I apply a random forest algorithm and fivefold cross validation using the training data set to determine the best hyperparameters for my model. Then, I train my random forest architecture and evaluate its accuracy on the validation data set. Furthermore, to perform an unbiased sensitivity analysis, I apply the same hyperparameters found to cases 2 and 3; thus, only the data input to the ML model is changing.

To compute the SHAP values to explain the outputs of my models, I apply a SHAP TreeExplainer implementation using the training data set (Lundberg and Lee, 2017; Lundberg et al., 2018a), which provides a fast and exact computation of the Shapley values for tree-based ML architectures. The SHAP global feature importance, SHAP local explanation summary plots, and SHAP dependence plots combine several local explanations for each prediction, thus providing a means to understand the global behavior of the model and determine the global importance of each seismic attribute (Lundberg et al., 2018a, 2020; Molnar, 2021).

Finally, using the SHAP force plots, I can analyze how the ML model uses the seismic attributes during classification and study their impact on the model prediction at areas of interest in my seismic facies prediction. By computing the SHAP values throughout my seismic data set and corendering them with the seismic amplitude volume, I perform an in-context interpretation to understand how changes in geology associated with variations in the seismic response are related to the SHAP values and how they affect the facies predictions.

Case 1: Original seismic attributes

Seismic attributes provide the interpreter a means to perform a faster and more comprehensive reservoir characterization. Attributes quantify patterns in the seismic volume. When displayed and integrated with seismic geomorphology, these attributes allow a more complete understanding of the depositional environment (Posamentier and Kolla, 2003; Chopra and Marfurt, 2007). For example, seismic attributes have been widely used as

input for ML architectures to classify seismic facies (Zhao et al, 2015, 2016; Qi et al. 2016; Lubo-Robles and Marfurt, 2019; Lubo-Robles et al. 2021).

GLCM attributes are useful to analyze variations in the geomorphology of stratigraphic features characterized by distinct patterns or textures by statistically measuring vertical and lateral changes in the seismic amplitudes (Haralick et al., 1973; Angelo et al., 2009, Matos et al., 2011; Zhao et al., 2016; Di and Gao, 2017; Qi et al., 2020). In this study, I evaluate GLCM entropy and GLCM contrast attributes, in which the former measures the level of disorder or randomness, and the latter computes changes in the intensity between seismic samples (Chopra and Alexeev, 2006; Chopra and Marfurt, 2007; Yenugu et al., 2010; Di and Gao, 2017).

The coherence attribute helps to differentiate between low energy chaotic reflectors and seismic discontinuities associated with salt and mud diapirs, faults, channels edges and seismic noise from the more homogenous background geology by measuring the similarity between traces inside a 3D analysis window moving throughout the seismic data set (Gersztenkorn and Marfurt, 1999; Chopra and Marfurt, 2007; Li and Lu, 2014). In addition, by measuring the energy associated with the sum of eigenvalues computed from the covariance matrix of the windowed seismic traces (Gersztenkorn and Marfurt, 1999), the total energy attribute is useful to isolate low energy chaotic reflectors from higher energy seismic responses.

The reflector convergence attribute analyzes changes in the inline and crosslines components of the dip, providing a means to quantitatively identify stratigraphic features

such as angular unconformities, lateral changes in thickness, overbank deposits, and diapirism withdrawal (Marfurt and Rich, 2010; Chopra and Marfurt, 2013).

Following Marfurt and Kirlin (2001), Sinha et al. (2005), and Chopra and Marfurt (2014), spectral-decomposition analysis can be used to study changes in stratigraphy, bed thickness, and porosity as well as to identify hydrocarbon-bearing formations. In this paper, I compute the spectral bandwidth attribute after applying continuous wavelet transform spectral decomposition which decomposes the seismic volume into different phase and magnitude components at different frequencies (Chopra and Marfurt, 2016). According to Zhang et al. (2008) and Qi et al. (2020), the spectral bandwidth represents a statistical measure of the spectrum that it is proportional to its standard deviation, offers a more robust estimate of the bandwidth than instantaneous bandwidth, and provides a means to isolate chaotic reflections from other seismic facies.

Finally, I evaluate a suite of nonparallelism attributes, which computes statistical measures of the seismic traces within an analysis window to quantitatively estimate lateral variations in reflector dips and energy (Qi and Marfurt, 2019). The dip deviation and energy deviation attributes measure lateral changes in the dip and energy of the seismic reflections, respectively, and are very useful to distinguish between chaotic and parallel reflectors. Furthermore, the covariance of dip and energy gradient seismic attribute captures both, changes in dips and energy, and is used to isolate rotated, deformed, and chaotic seismic reflections (Qi and Marfurt, 2019).

In Figure 3.4, I show the candidate seismic attributes along line AA'. I observe that the target seismic facies show different attribute responses. Salt diapirs are characterized by

lower coherence and higher entropy and contrast than the higher energy, more coherent background conformal sediments, whereas MTDs exhibit higher variability in their seismic response due to the presence of rotated blocks embedded in a discontinuous chaotic matrix. I also note faster changes in the energy, and dips and higher reflector convergence in seismic reflectors closer to the edges of the salt diapirs. Finally, due to the more noisy, "salt-and-pepper" appearance of the salt, they are characterized by a broader bandwidth response than the other target seismic facies.

Case 2: Applying Kuwahara filter to seismic attributes

For case 2, I apply a 5 x 5 x 5 voxel 3D Kuwahara filter to my seismic attributes computed in case 1. Qi et al. (2016) report that the 3D Kuwahara median filter removed random noise, smoothed the internal response of the seismic facies, and sharpened their edges, which resulted in a better discrimination between seismic facies. The voxel-based filter uses an overlapping window surrounding each voxel in the input seismic attribute space and assigns the median value of the overlapping window characterized by the lowest mean-normalized standard deviation.

Analyzing the Kuwahara-filtered seismic attributes along line AA' (Figure 3.5), I note that they show a strong reduction in the seismic noise, while maintaining the attribute responses observed in the original candidate seismic attributes in case 1. Furthermore, the target seismic facies show a "blocky" appearance with smoother internal responses and sharper edges.

Case 3: Adding band-limited random noise to seismic volume

To perform my sensitivity analysis, I add band-limited AWGN with a target S/N to my seismic volume to interpret how the tree-based model behaves when the noise level of the input candidate seismic attributes increases, such as the signal is two times stronger than the noise (S/N=2). For more information on the mathematical details of adding band-limited AWGN to the seismic volume, please refer to Appendix A.

In Figure 3.6, I show the seismic volume before (Figure 3.6a) and after (Figure 3.6b) adding random noise with a target S/N=2. As expected, I observe an increase in the salt-and-pepper appearance throughout the whole seismic data set when adding random noise (Figure 3.6b). Moreover, when computing the seismic attributes using the noise-contaminated volume (Figure 3.7) and the same parameters as case 1, I observe that some attributes such as coherence, total energy, GLCM entropy, and spectral bandwidth offer a poorer discrimination between seismic facies compared to the original candidate seismic attributes (Figure 3.4), possibly associated with the increasing noise in the more coherent, higher amplitude rotated blocks of the MTDs and the conformal sediments surrounding the salt diapirs.

Definition of training and validation data sets

To define my training data set, I pick a group of polygons enclosing my target seismic facies from line AA' to EE' (Figure 3.8). Voxels associated with low-amplitude chaotic reflectors (the orange polygons), mixture of chaotic and coherent components (the green polygons), and parallel, high-amplitude conformal reflectors (the purple polygons) are extracted from my nine candidate seismic attributes. For the validation data set, I extract the

seismic facies of interest only along line FF' (Figure 3.8) to maintain a splitting ratio close to 80%-20% in which 7191 voxels belong to the training data set, whereas 1335 voxels are associated with the validation data set.

I ensure balance in my data by randomly selecting the same number of voxels belonging to each facies on training and validation data sets. Therefore, in the training data set, 2397 voxels have been assigned to each seismic facies, whereas in the validation data set each facies has 445 samples. Note that the training and validation sets are generated only for a few lines in the data set to leave the rest of the seismic volume as new unseen, unlabeled data set for interpretation.

Random forest and hyperparameter tuning

A random forest is a nonparametric ML technique consisting of an ensemble of randomized decision trees used for classification and regressions tasks. For classification, the final prediction is made by voting for the most predominant class among all tree predictors, whereas for regression the final output is given by averaging the results obtained in each individual tree (Breiman, 2001; Scornet et al., 2015; Genuer et al., 2017). Following Breiman (2001), Biau et al. (2008), Scornet et al. (2015), and Genuer et al. (2017), random forest generates high performance models in which only a small number of hyperparameters require tuning to obtain accurate results that are robust against overfitting and in the presence of noise and outliers in the data.

In this paper, I optimize the hyperparameters of my random forest architecture using a random-search algorithm in which a suite of hyperparameters combinations is randomly sampled from an initial grid space, which provides a simple and efficient means to find the

optimal hyperparameters (Bergstra et al., 2011; Bergstra and Bengio, 2012). I also apply a fivefold cross validation technique in which the data are split in five different random groups, with four groups are used as training data and remaining group used as validation. This process is repeated five times, and the mean accuracy is computed to assess the model performance.

I computed the mean accuracy after running 100 iterations of the random search algorithm, applying fivefold cross validation in each iteration and considering only the training data from case 1 associated with polygons manually picked from line AA' to EE' to extract voxels from the candidate seismic attributes computed using the original seismic amplitude volume. The mean accuracy ranges from a minimum of 86.08% to a maximum of 87.12%. Therefore, because these hyperparameters provide the best results during my search, I use them for my final tree-based architecture.

I now analyze the validation accuracy of my random forest model when evaluating my validation data set picked along line FF' (Figure 3.8) for cases 1-3 (Table 3.1). Please, note that the same hyperparameters found during the hyperparameter search are used in cases 2 and 3 to perform an unbiased sensitivity analysis in which only the input data for the random forest architecture are changing. I observe that applying Kuwahara filtering to the seismic attributes (case 2) provides the highest validation accuracy of 91.46%. Adding random noise with target S/N = 2 results in a decrease of the validation accuracy from 83.6%, associated with the original attributes (case 1), to 81.72%.

Results

SHAP implementation

Global interpretability: SHAP global feature importance and SHAP summary plots

Following Lundberg et al. (2020), combining several local explanations of the model allows interpreters to analyze the importance of each input attribute in the classification. Attributes associated with high average SHAP values have a higher importance in the classification than attributes characterized by low average SHAP values (Lundberg et al., 2020; Molnar, 2021).

In Figure 3.9, I analyze the average SHAP values associated with each candidate seismic attribute for each case study in my sensitivity analysis. In terms of the overall importance, I note that the highest contribution to the classification when using the original data (case 1) (Figure 3.9a) is given by the total energy followed by the dip deviation, energy deviation, coherence, covariance of dip and energy gradient, GLCM contrast, spectral bandwidth, GLCM entropy, and reflector convergence. The attribute importance is almost identical with a few differences when using Kuwahara filtering (case 2) and adding band-limited seismic noise to the data set (case 3), as shown in Figures 3.9b and 3.9c, respectively.

Then, I examine the significance of each input feature to the classification for each of the facies (Figure 3.10). This is the unique and attractive feature of SHAP values, in that it allows the user to assess the contribution of each of the inputs toward each of the classes/labels. For MTD, I find that the attribute importance when using the original data as

input (case 1) is the same as the overall importance (Figure 3.9a) and that relative changes in the attribute importance remain similar for cases 2 (Figure 3.9b) and 3 (Figure 3.9c).

When applying Kuwahara filtering, spectral bandwidth still becomes the third most important attribute for the classification. However, contrary to the overall importance, GLCM entropy is now the sixth most important attribute for the MTD seismic facies. However, when adding band-limited seismic noise, GLCM contrast becomes the fourth most important attribute, and the coherence shows larger impact than the covariance of dip and energy gradient attribute for the MTD seismic facies (Figure 3.10a).

For salt, I now observe that the spectral bandwidth becomes the fifth more important feature when using the original seismic attributes for classification (Figure 3.10b). For case 2, spectral bandwidth becomes the second most important attribute showing a large increase in its average SHAP value, whereas the reflector convergence attribute also shows a slight increase in its importance when applying Kuwahara filtering. For case 3, GLCM contrast shows a drastic increase in its importance, and it becomes the second most important attribute to identify salt seismic facies in the presence of strong noise.

Finally, I analyze the attribute importance for the conformal sediments (Figure 3.10c). Contrary to the MTD and salt seismic facies, dip deviation is now the most important attribute for all cases, followed by the total energy. In addition, for case 1, the coherence and GLCM entropy attributes become the third and sixth most important attribute, respectively, whereas energy deviation takes the fifth place to isolate the background geology from the other target seismic facies.

When considering the 3D-Kuwahara filtered seismic attributes as input, I observe that GLCM entropy and spectral bandwidth become the third and fifth most important attributes in the classification. I also note that the coherence slightly increases its average SHAP value. This behavior also is seen for the MTD seismic facies, whereas for the salt seismic facies coherence only increases its importance in the presence of noise.

In the presence of strong noise (case 3), I observe that the coherence decreases its importance and becomes the sixth most important attribute, whereas the GLCM contrast now takes the fifth position. Furthermore, similar to the MTD and salt seismic facies, GLCM entropy and spectral bandwidth become the worst attributes for classification in the presence of strong noise.

Then, to study how large or small values in attribute space affect how the ML model classifies certain voxels into a particular seismic facies, I analyze the SHAP summary plots (Figure 3.11), which illustrate attribute importance along with the sensitivity of the model classes to variations in the input attributes.

Each dot in the plot represents an individual voxel of the training data set. The *x*-axis represents the SHAP value for each candidate seismic attribute, whereas the *y*-axis represents the attribute importance for each seismic facies in the classification (Lundberg et al., 2020; Molnar, 2021). The blue colors represent low values of the input attribute, whereas the red colors represent higher values. The position of each dot on the plot indicates its importance to the classification of the specific label. For example, when analyzing attribute significance for the MTD using the original set of seismic attributes, high values of total energy are associated with a high probability of the voxel being an MTD, whereas low values represent

a low chance of the voxel being an MTD. Conversely, high values of coherence are associated with a low chance of the voxel being an MTD. This information is provided in Figure 3.11 for all facies and all three cases considered, showing the power and utility of using SHAP values.

For MTD, I observe that the attribute's effects are similar for all cases. In general, high to medium values of total energy, high values of dip deviation, energy deviation, GLCM entropy, and low values of coherence, covariance of dip and energy gradient, GLCM contrast, and spectral bandwidth tend to increase the probability of having a MTD seismic facies. I also note that, in the presence of strong noise, it is more difficult to establish clear attribute's effects for coherence, covariance of dip and energy gradient, spectral bandwidth, and GLCM entropy. In contrast, the reflector convergence, which initially does not have any effect when performing the classification using the original seismic attributes, shows a clear effect in the presence of noise given by high values of reflector convergence pushing toward the MTD seismic facies.

Then, for the salt seismic facies, I note that the attribute's effects still tend to be similar for all cases. I observe that high values of dip deviation, GLCM contrast, and spectral bandwidth, medium to high values of GLCM entropy, and low values of total energy, energy deviation, covariance of dip and energy gradient, and reflector convergence increase the probability of classifying a particular voxel as salt seismic facies. For cases 1 and 2, there are some voxels characterized by low and high coherence that are increasing the probability of having salt seismic facies.

However, in the presence of strong noise, the effect of the coherence attribute in the classification becomes better defined in which low values of coherence are being classified as salt, whereas high values are classified as not salt. Moreover, the spectral bandwidth and GLCM entropy attributes not longer show a clear effect in identifying salt seismic facies.

Finally, for conformal sediments, I observe that low values of dip deviation and energy deviation, high values of coherence and covariance of dip and energy gradient, and medium values of spectral bandwidth increase the probability of having conformal sediments. Furthermore, voxels characterized by either high or low values of GLCM contrast are being classified as conformal sediments.

In addition, I note that medium to high values of total energy are characterized by SHAP values close to zero, meaning that these values are making less impact when the ML model classifies conformal sediments, whereas some voxels characterized by low values of total energy and medium to high values of GLCM entropy tend to be classified as conformal sediments by the algorithm. Finally, as seen in the previous seismic facies when I add band-limited noise to the data set (Figures 3.11c and 3.11f), GLCM entropy and spectral bandwidth still do not show a clear effect to identify conformal sediments.

From the results obtained using the SHAP summary plots, I note that some attributes are common to more than one seismic facies. For example, dip deviation contributes in a similar manner to MTD and salt facies. However, the conformal sediments are related to the dip deviation in a different manner that helps to differentiate it from the two other seismic facies. Using energy deviation and some voxels characterized by low values of GLCM contrast, salt and conformal sediments show overlap between them, whereas the MTD

seismic facies is easily identify using these attributes. In contrast, MTD and conformal sediments show overlap in the seismic responses when using the spectral bandwidth attribute, but salt is clearly distinguished from the other facies when using this attribute.

These commonalities between facies reinforce the idea that using multiple attributes as input represents a good approach for seismic facies classification because, a priori, the strength of the contribution of each attribute to the final classification is unknown and it allows to discriminate among seismic facies that might have similar seismic responses in some attributes but better differentiation when considering other attributes.

Global interpretability: SHAP dependence plots

Although the previous discussion indicated the role of each of the input attributes in the final classification, the discussion was provided in terms of low/high values of the input attributes. SHAP dependence plots for the candidate seismic attributes provide additional information (Lundberg et al. 2020; Lerza et al., 2020) in terms of the actual values of the inputs.

In these plots, each dot represents a voxel from the training data set, the *x*-axis is associated with the attribute's value, and the *y*-axis shows the impact of that voxel in the prediction. Voxels associated with positive SHAP values indicate an increase in the probability of having a particular seismic facies, whereas voxels characterized by negative SHAP values decrease this probability. Also, dispersion in the vertical axis is associated with interaction between the candidate seismic attributes in the model. Finally, the SHAP dependence plots are automatically color coded by a feature that might interact during classification with the attribute that is being plotted in the *x*-axis (Lundberg et al., 2020).

Considering three cases for the sensitivity analysis, three target seismic facies, and nine input seismic attributes, a total of 81 SHAP dependence plots are analyzed. In this paper, I show the SHAP dependence plots for the total energy and dip deviation attributes (Figures 3.12 and 3.13) because these have consistently shown large impact in the classification. Plots for the remaining input attributes and their interpretations can be found as supplemental information (Figures 3.S1-3.S7). In addition, because my main objective includes understanding how changes in the seismic attribute's values increase the probability of the seismic facies during classification, I focus only on the positive SHAP values response in the SHAP dependence plots.

In Figure 3.12, I analyze the dependence plots for the total energy attribute per seismic facies for all cases in my sensitivity analysis. Please note that the attribute's values in the *x*-axis for all SHAP dependence plots are shown without scaling for interpretational purposes. Moreover, Kuwahara filtering is removing outliers in the data (the green arrows) in all the plots.

For MTD seismic facies (Figures 3.12a-3.12c), all plots are color coded by the dip deviation attribute. For positive SHAP values, I observe two trends: (1) values of total energy larger than approximately 400 and high dip deviation and (2) values of total energy larger than 400 and low dip deviation that push towards MTDs, meaning that these values increase the probability of a voxel being classified as MTD.

For the salt seismic facies (Figures 3.12d-3.12f), I note that the SHAP dependence plots are color coded by different attributes. For cases 1 and 2, I observe that, in general, values of total energy lower than 400 with low coherence and high dip deviation increase

the probability of having salt seismic facies (Figures 3.12d and 3.12e). However, in the former case, some voxels characterized by total energy lower than 400 and higher coherence are also pushing towards salt. Finally, when the input data are contaminated with band-limited noise, I note that values of total energy lower than approximately 500 and high values of GLCM contrast increase the probability of a certain voxel being classified as salt.

Finally, for the conformal sediments facies (Figures 3.12g-3.12i), I observe that cases 1 and 3 are color coded by dip deviation (Figures 3.12g and 3.12i), whereas case 2 (Figure 3.12h) is color coded by coherence. Moreover, two trends are visible in all cases. The first trend shows that values of total energy lower than approximately 400-500 with high values of dip deviation and low values of coherence, whereas the second trend shows values of total energy larger than 400-500 with low values of dip deviation and high values of coherence, which increase the probability of a voxel being classified as conformal sediments.

Then, I show the SHAP dependence plots for the dip deviation attribute per seismic facies for all cases (Figure 3.13). For MTD seismic facies, I note that cases 1 and 2 are color coded by the total energy (Figures 3.13a and 3.13b), whereas case 3 (Figure 3.13c) is color coded by GLCM contrast. In addition, I still observe two clear trends that are increasing the probability of having MTDs. The first trend shows larger impact in the classification, and it is characterized by values of dip deviation larger than approximately 2 with high values of total energy and low values of GLCM contrast. In contrast, the second trend has smaller impact, and it shows voxels with dip deviation larger than 2 and low values of total energy and high values of GLCM contrast.

Analyzing the salt seismic facies (Figures 3.13d-3.13f), all SHAP dependence plots are color coded by the total energy attribute. I observe that values of dip deviation larger than approximately 2.5 and lower values of total energy are pushing towards the salt seismic facies. However, some values characterized by higher total energy are also increasing the probability of having salt. Finally, in the SHAP dependence plots for the conformal sediments (Figures 3.13g-3.13i), case 1 is color coded by total energy, whereas cases 2 and 3 are color coded by the coherence attribute. In addition, I still observe two trends that have different impact in the classification, but both are pushing toward the conformal sediments facies: (1) values of dip deviation lower than 2.5 and higher values total energy and coherence and (2) values of dip deviation between 2.5 and 4 with lower values of total energy and coherence.

After analyzing all 81 SHAP dependence plots for all cases and facies in my analysis, I note that, to perform a seismic facies classification to distinguish among MTDs, salt, and conformal sediments, the ML model is "learning" a set of rules in multiattribute space.

In Table 3.2, I summarize the set of rules generated by the model after analyzing the SHAP dependence plots and SHAP summary plots (Figure 3.11). After studying the changes in attribute values for conformal sediments, I observe two well-defined trends. The first trend is associated with lower values of total energy and coherence, and larger values of dip deviation, energy deviation, covariance of dip and energy gradient, GLCM contrast, spectral bandwidth, GLCM entropy, and reflector convergence, whereas the second trend shows a completely different response characterized by large values of total energy and coherence,

and lower values of dip deviation, energy deviation, covariance of dip and energy gradient, GLCM contrast, spectral bandwidth, GLCM entropy, and reflector convergence.

Therefore, based on the attribute response seen for the conformal sediments, I hypothesize that the first trend is possibly associated with overlap between conformal sediments and the MTDs and salt seismic facies related to dipping conformal reflectors located close to the edges of the salt, which are characterized by rapid changes in dip and lower seismic energy due to a decrease in the quality of the seismic imaging, whereas the second trend might be related to flat, higher amplitude conformal sediments located between salt diapirs.

In addition, after summarizing the set of rules for the MTDs, I observe that this facies is actually characterized by one well-defined trend of higher values of total energy, dip deviation, energy deviation, GLCM entropy, and lower values of coherence, covariance of dip and energy gradient, and GLCM contrast. Therefore, I believe that the second trend seen in the SHAP dependence plots and characterized by lower values of dip deviation, total energy, and higher values of GLCM contrast, spectral bandwidth, and covariance of dip and energy gradient might be associated with overlap between MTDs, which are composed of chaotic and coherent components, dipping and/or parallel conformal sediments, and salt seismic facies.

Finally, I note that the SHAP dependence plots can be color coded by different seismic attributes possibly indicating that the interaction among input attributes changes based on the quality of the input data and the seismic facies analyzed. In this paper, I only study the composite SHAP values response to understand the behavior of the model when

performing the seismic facies classification. A complete computation of SHAP interaction values (Lundberg et al., 2020) and the study of the main effect of the attribute and its interaction with other features are needed to fully understand how the interaction between candidate attributes affects the seismic facies classification.

Seismic facies predictions

To further assess how changes in the quality of the candidate input attributes affect the classification in the presence of previously unseen/unlabeled data, I compare the seismic facies prediction volumes using the three trained random forest models for each case along line GG', in which hyperparameters are the same for all models, and only the input data are changing to perform an unbiased comparison.

In Figure 3.14, I show the random forest facies prediction corendered with the seismic amplitude along line GG' for each case using all candidate seismic attributes. I observe that, in general, the ML model classifies correctly among MTDs (the green facies), salt (the orange facies), and conformal sediments (the purple facies). However, the result obtained after applying Kuwahara filtering to the input attributes (Figure 3.14b) shows a smoother facies response, sharper edges, and better classification of previously unseen/unlabeled data than using the original data (case 1) and adding band-limited noise (case 3), in which the facies predictions look noisier and show more misclassifications.

I note that, for cases 1 and 3, there are more gaps, associated with coherent migration artifacts inside salt diapirs (the yellow arrows), being misclassified as MTDs or conformal sediments by the algorithm. Furthermore, noisy data in the edges of the seismic volume with little interpretational values are misclassified as salt seismic facies (the blue arrows) and this

misclassification becomes more prominent in case 3 because of the added band-limited noise.

In addition, I observe that dipping conformal reflectors show some overlap with the MTD and salt seismic facies and that these reflectors are more prone to be misclassified as salt or MTDs (the red arrows) in cases 1 and 3 compared to the results obtained in case 2. Moreover, I observe that high-amplitude, parallel conformal reflectors tend to be well classified in all cases. However, overlaps with the MTD seismic facies are more prominent when adding band-limited AWGN or using the original attributes. Finally, high-amplitude, seismic multiples are being misclassified as MTDs and conformal sediments by the model in all cases (the white arrows).

Then, analyzing the random forest facies prediction corendered with the seismic amplitude at time slice $t = 1.3$ s, I observe that case 2 still shows the best seismic facies map and performance when classifying unseen data. Moreover, I note that conformal sediments misclassified as salt or MTDs are still more prominent in cases 1 and 3.

In Figure 3.15, I show the probability volumes for all seismic facies and cases along line GG'. I note that each seismic facies is classified with high probabilities meaning that my ML models show high performance when differentiating among MTDs, salt, and conformal sediments. Moreover, for correctly classified facies, I do not observe any dimming in the probabilities between cases possibly indicating that facies are being classified with similar confidence by the algorithm. However, similar to the facies predictions, probability volumes for cases 1 and 3 tend to be noisier and show more

misclassifications between the target facies mainly inside and around salt diapirs compared to the results obtained when using the Kuwahara-filtered seismic attributes as input.

Finally, I perform a geobody extraction (Meyer et al., 2001) to isolate and study the 3D distribution of the MTD, salt, and conformal sediments facies using only the seismic facies volume associated with case 2, because it provides the most optimal classification. In Figure 3.16, I show the 3D seismic facies mapping using as criteria voxels characterized by probabilities higher than 70% for each seismic facies. In general, I can accurately extract and isolate the target seismic facies thorough the study area. However, I observe that some voxels inside the salt diapirs are being misclassified as MTDs or conformal sediments (the yellow arrows). Furthermore, I still note that dipping conformal reflectors tend to be misclassified as salt or MTDs by the random forest algorithm (the red arrows).

Although computing probabilities for each facies is a common tool to examine the performance of a ML algorithm in seismic classification tasks, this approach does not provide a means to understand how the model uses the candidate seismic attributes to obtain these probabilities and classify a voxel as a particular seismic facies. Therefore, to further understand my best model associated with case 2, I analyze the SHAP force plots in four voxels of interest that were misclassified by the algorithm. Furthermore, computing the SHAP values throughout my seismic volume, I perform an in-context interpretation and examine how variations in the seismic response affect the facies predictions.

Local interpretability

Following Lundberg at al. (2018b, 2020) and Molnar (2021), SHAP force plots allow the interpreter to study how the seismic attributes affect the model prediction at a particular

voxel, in which SHAP values are considered as "forces" that increase or decrease the probabilities for the target seismic facies. In SHAP force plots, prediction starts from the base value which is given by the average of all probabilities for each seismic facies present in the data set if none of the input attributes are known (Lundberg and Lee, 2017; Molnar, 2021). In addition, positive SHAP values are associated with the red arrows that are increasing the probability, whereas the blue arrows are related to negative SHAP values that are decreasing the probability of having a particular seismic facies. Furthermore, the size of the arrow indicates the impact of a particular seismic attribute in the classification of the voxel. Finally, in this study, each seismic facies starts with a base probability of 33.3%.

In Figures 3.17 and 3.18, I analyze the SHAP force plots in four voxels of interest A, B, C, and D using my best seismic facies classification volume associated with case 2 along line GG'. Considering voxel A (Figure 3.17), I observe that the voxel is located inside salt diapir 1 and that the algorithm misclassified it as MTD facies with a 45% probability, whereas the salt seismic facies and the conformal sediments facies have probabilities of 13% and 42%, respectively.

Using the SHAP force plot at voxel A, I analyze how the algorithm use the seismic attributes to obtain the final probabilities for each seismic facies. For the MTD seismic facies (Figure 3.17a), I note that the voxel starts with a base value of having MTD of 33%. Then, considering the effect of the candidate seismic attributes in the model, I note that the attributes making the most impact for this voxel are the total energy = 704.12, dip deviation = 7.01, spectral bandwidth = 58 Hz, and coherence = 0.7, which are pushing the probability

up, whereas values of GLCM entropy = 0.52 and covariance of dip and energy gradient = 0.77 push down the probability to the final 45%.

Then, for the salt seismic facies (Figure 3.17b), I observe that the coherence, dip deviation, and covariance of dip and energy gradient attributes increase the probability, whereas the total energy and spectral bandwidth are pushing the probability down from the base value of 33% to the final 13%. Finally, for the conformal sediments (Figure 3.17c), the final probability of 42% is obtained by the dip deviation and coherence attributes pushing down, whereas the GLCM entropy, covariance of dip and energy gradient, energy deviation, total energy, and reflector convergence push the probability up.

Comparing these attributes values with the multiattribute relationship described in Table 3.2, I note that, in general, the behavior seen in the SHAP force plots for voxel A, matches well the response seen for all attributes for each seismic facies, with only a few exceptions. In the MTD seismic facies, a value of GLCM entropy = 0.52 is actually decreasing the probability. However, this value is only slightly larger than my threshold. For the salt seismic facies, the covariance of dip and energy gradient which shows a value larger than 0.2 is increasing the probability. However, based on the SHAP dependence plot for the covariance of dip and energy gradient attribute and salt seismic facies (see supplemental information Figures 3.S1-3.S7), I know that some values larger than the threshold can increase the probability of having salt. Finally, I note that the classification for conformal sediments is more challenging because I have to consider that the attribute response for flat, high amplitude and dipping reflectors (possibly showing overlap with MTDs and salt seismic facies) are driving the classification for this seismic facies.

Then, I study voxels B and C, which are located inside the high-amplitude seismic multiples (Figures 3.18a and 3.18b). I observe that these voxels are being misclassified as conformal sediments and MTDs with very high probabilities of 82% and 99%, respectively. Analyzing the SHAP force plot for voxel B and only for the facies with the highest probability, I observe that a value of GLCM contrast = 31.48 increase the probability from the base value of 33.3% to 36.24%, total energy = 1305.18 increase this probability to 40.75%, spectral bandwidth = 44.45 Hz to 45.41%, GLCM entropy = 0.5 to 55.92%, energy deviation = 1.11 to 68.73%, and coherence = 0.94 shows the largest impact in the classification for this voxel and increases the probability to 83%, then the remaining attributes show a composite small impact of 0.1% that decrease the probability to the final 82%.

Then, analyzing the SHAP force plot for MTD seismic facies at voxel C, starting from the base value of 33%, covariance of dip and energy gradient = 0.204 increases the probability to 33.92% (not shown automatically in the SHAP force plot due to its small impact in the classification), coherence = 0.68 to 38.37%, GLCM entropy = 0.53 to 42.91%, energy deviation = 3.46 to 47.64%, GLCM contrast = 52.43 to 52.91%, spectral bandwidth = 54.63 Hz to 62.22%, dip deviation = 5.31 to 76.58%, and, with the largest impact, total energy = 695.02 to a probability of 99.1%, whereas a value of reflector convergence = 0.104 - also not shown automatically in the SHAP force plot due to its small impact – decreases the probability only 0.1% to its final 99%.

When I compare the attribute responses at voxels B and C with Table 3.2, I note that the behaviors match completely the response seen for flat conformal sediments and the MTD

seismic facies, possibly explaining why these voxels have large probabilities of being classified as conformal sediments and MTDs, respectively, because responses associated with dipping reflectors or salt seismic facies are not involved.

Finally, I study voxel D that should have been classified as conformal sediments because it is located inside dipping conformal reflectors surrounding the salt diapirs but was misclassified by the algorithm as MTDs. Analyzing the SHAP force plot for the MTD facies (Figure 3.18c), I note that values of GLCM contrast = 76.7, spectral bandwidth = 60.88 Hz., coherence = 0.51, GLCM entropy =0.54, dip deviation = 4.69, and total energy = 616.21 are pushing the probability up, whereas values of energy deviation = 10.25 push down the probability to its final 76%. In contrast, in the SHAP force plot for the conformal sediments (Figure 3.18d), total energy = 616.21, covariance of dip and energy gradient = 0.39, energy deviation = 10.25, and spectral bandwidth = 60.88 Hz increase the probability, whereas dip deviation = 4.69, GLCM entropy = 0.54, and coherence = 0.51 push the probability down to its final 18% of having conformal sediments.

When I compare the attributes' response at voxel D with Table 3.2, I observe that the response shows a large overlap between MTDs and conformal sediments. The GLCM contrast and total energy attributes match well with the MTD and parallel conformal sediments, and spectral bandwidth, coherence, GLCM entropy, dip deviation, energy deviation match with the response seen for MTDs and the trend 1 for conformal sediments, whereas covariance of dip and energy gradient matches trend 1 seen for conformal sediments and trend 2 for MTDs.

In-context interpretation using SHAP values

By computing the SHAP values for all Kuwahara-filtered seismic attributes and target seismic facies and corendering them with the seismic amplitudes, I can interpret how the ML model "sees" the geology perform and perform an in-context interpretation to understand how changes in the seismic response affect the model prediction.

In Figure 3.19, I show the SHAP values corendered with the seismic amplitudes along line GG' for the total energy, dip deviation, and energy deviation attributes for MTDs, salt, and conformal sediments. Similar to the SHAP force plots, positive SHAP values increasing the probability are characterized by red colors, whereas negative SHAP values decreasing the probability are associated with the blue colors. Analyzing the total energy attribute for MTD seismic facies (Figure 3.19a), I observe that the ML algorithm is correctly identifying MTDs in the area. However, high-amplitude conformal sediments and reflectors with lower amplitudes, lower seismic quality surrounding the salt diapirs also increase the probability of having MTDs (the white arrows).

For salt seismic facies (Figure 3.19b), although some dipping reflectors and noisy areas close to the edges of the salt are increasing the probability for this seismic facies (the orange arrows), the model is, in general, classifying the lower amplitude, chaotic salt diapirs correctly. Finally, the conformal sediments are being correctly isolated by the model (Figure 3.19c). Nevertheless, overlap with MTDs is visible (the yellow arrows).

Analyzing the SHAP values for the dip deviation (Figure 3.19d-3.19f) and energy deviation (Figure 3.19g-3.19i) attributes, I note that the MTD seismic facies still show overlap with lower amplitude, lower seismic quality reflectors around the salt diapirs.

However, in the dip deviation attribute, some overlap with the salt diapirs exists. For the salt seismic facies, the overlap with MTDs is still visible when using the dip deviation attribute. However, in the energy deviation attribute, the salt diapirs are now having a strong overlap with the flat, high-amplitude conformal sediments located inside the mini-basins. Finally, for the conformal sediments seismic facies, I observe that the ML model is correctly identifying the flat, high-amplitude reflectors and some dipping reflectors showing higher amplitudes. However, some dipping reflectors characterized by lower quality in the seismic imaging are now decreasing the probability for this seismic facies.

Then, I analyze the SHAP values corendered with the seismic amplitudes for the coherence, covariance of dip and energy gradient, and GLCM contrast attributes and the target seismic facies along line GG' (Figure 3.20). I observe that the MTD seismic facies still show overlap with lower amplitude dipping reflectors when using these seismic attributes. Moreover, overlap with the salt diapirs is also visible, but only when using the covariance of dip and energy gradient attribute.

For the salt seismic facies, I observe that the ML algorithm correctly isolates the salt diapirs in the study area. However, slight overlap with the MTD and dipping conformal reflectors exists when considering the coherence attribute, while, using the GLCM contrast attribute, the overlap with the MTDs decreases and it is mainly occurring only with the reflectors surrounding the salt diapirs. Finally, for the conformal sediments seismic facies, I observe that, using the coherence and GLCM contrast attributes, the model is identifying parallel and dipping conformal reflectors in the study area. However, some overlap with the salt seismic facies is visible when considering the latter attribute. In addition, when using

97

the covariance of dip and energy gradient, the ML algorithm only correctly classifies the dipping conformal sediments, whereas the flat high-amplitude reflectors are not making an impact in the classification.

Finally, I perform an in-context interpretation along line GG' using the spectral bandwidth, GLCM entropy, and reflector convergence attributes (Figure 3.21). I observe that the reflector convergence attribute does not have a large impact in the classification and does not have clear trends in the study area beyond showing some overlap between the seismic facies. In contrast, I note that MTDs are correctly identified by the model but overlap with conformal sediments and salt diapirs still exist when using the spectral bandwidth and GLCM entropy attributes, respectively. In addition, the salt diapirs are correctly isolated from the rest of the seismic facies when using these seismic attributes. However, noisy areas close to the edges of the survey and dipping reflectors are slightly increasing the probability of being classified as salt. Finally, for the conformal sediments, I observe that they are correctly classified when using the spectral bandwidth attribute, although some overlap with MTDs and salt exists. However, when using the GLCM entropy attribute, only the flat high-amplitude conformal sediments are being correctly identified by the ML model, whereas some dipping conformal reflectors characterized by lower amplitudes are now decreasing the probability.

Discussion

After applying SHAP to the cases proposed to perform my sensitivity analysis, I note that the attribute importance is dynamic, and changes based on the quality of the input data and the seismic facies analyzed. I find that a combination of attributes that measure changes

in energy and dips are the best features to discriminate among MTDs, salt, and conformal sediments.

I observe that the total energy and dip deviation attributes are the most important seismic attributes during the seismic facies classification when applying Kuwahara filtering, although they show a decrease in their average SHAP values. When adding band-limited random noise, the total energy and dip deviation attributes are still the two most important. However, the difference between their average SHAP values is drastically reduced.

The dip deviation attribute shows high robustness in the presence of noise (Figure 3.9c). Because dip is almost always consistent with a seismic wavelet of a coherent reflector, there is little vertical dip deviation contribution except at unconformities and little lateral contribution except at faults, channel infill, and MTDs, whereas within salt, there are interference effects from crossing migrations ellipses characterized by high dip deviation.

When adding noise, the previously coherent (but random) migration ellipses get buried in noise, pushing the dip deviation toward some statistical mean of the random noise and away from the estimates that were biased toward the overlapping/conflicting dip migration ellipses which makes the changes of dip within the salt diapirs more homogenous, thus improving their differentiation from the MTDs and the background conformal sediments.

The total energy attribute exhibits anomalously low values for salt facies and shale-on-shale reflectors, whereas the response for the MTDs is mixed, characterized by intercalations of high and low energy values. When adding band-limited noise to the entire

survey, the root-mean-square (rms) ratio between seismic facies is reduced which produces a reduction in the separation between seismic facies (Figures 3.4 and 3.7).

In contrast, when applying Kuwahara filtering, the mean-normalized standard deviation can be very large when analyzing small means in the data set. This behavior will favor windows with higher mean, which results in less low total energy values after filtering and more overlap between seismic facies (Figures 3.4 and 3.5).

Finally, contrary to the results found when using the original data (Figure 3.9a), the spectral bandwidth and GLCM entropy attributes show a large increase in their importance when applying Kuwahara filtering (Figure 3.9b). For near coherent reflectors, the specular reflections from different migration trace pairs constructively interfere, increasing the amplitude, whereas aliased migration events and high frequency noise destructively interfere, such that their contribution is less than that of the specular reflections and the average bandwidth is moderate (Figures 3.4 and 3.5).

In contrast, the salt is characterized by aliased noise, and there are no specular reflections. Therefore, there is no constructive interference, and the computed spectral bandwidth represents bandwidth of the input traces, which is relatively high. When applying Kuwahara filtering, windows with a higher mean bandwidth are favored over those with a lower mean bandwidth and entropy, so that the salt facies (and the incoherent part of the MTDs) becomes higher bandwidth. In contrast, the specular reflections appear to be just smoothed and blocked. The same argument holds for GLCM entropy, in which high values of GLCM entropy are favored in chaotic areas, while more coherent facies are just smoothed

and blocked. This behavior results in better separation between the target seismic facies and an increase in the importance of these seismic attributes after filtering.

Conclusion

I successfully train and apply a multiattribute random forest classification algorithm to distinguish among MTDs, salt, and conformal siliciclastic sediments in a Gulf of Mexico data set and apply SHAP to understand how the model uses these input candidate seismic attributes to predict the target seismic facies when considering three different cases: (1) using original seismic attributes, (2) applying a Kuwahara median filter to remove noise and smooth the response of the input attributes for subsequent classification, and (3) adding band-limited random noise to the data set. Applying SHAP for global analysis, I determine that the attribute importance changes based on the seismic facies analyzed and the quality of the input data. For these three seismic facies, attributes measuring changes in energy and dip such as total energy and dip deviation show the largest importance in the classification for all cases. In the presence of band-limited random noise, the nonparallelism, GLCM contrast, and reflector convergence attributes offer greater robustness during the classification and are characterized by an increase in their importance. In contrast, when applying a Kuwahara filter for preconditioning the input data, I observe that now the spectral bandwidth and GLCM entropy attributes have the largest increase in their importance. I also find that to perform the classification, the ML model is learning a set of rules in multiattribute space for each seismic facies, in which the thresholds learned by the algorithm might vary depending on the quality of the seismic attributes.

For my data, I find significant overlap in the attribute expression of MTDs, salt, and flat or dipping conformal sediments; however, for different attributes, this overlap may be at different locations allowing multiattribute classification to maximize the distinction between the target seismic facies. In addition, using the seismic facies classifications for each case, I note that the results obtained when applying Kuwahara filtering offer a blockier, more geologically reasonable classification free of inclusions, smoother facies response, and better classification of previously unseen/unlabeled data. Applying SHAP for a local analysis, I analyze at a voxel scale how the model obtains a particular probability. I found that dipping parallel conformal sediments around the edges of the salt characterized by lower amplitudes and a lower S/N tend to be misclassified as MTDs by the algorithm. Coherent noise inside the salt diapirs can be misclassified either as MTDs or conformal sediments. Because the algorithm was not trained to differentiate high-amplitude seismic multiples from the remaining seismic facies, I observe that these tend to be misclassified as MTDs or conformal sediments because the seismic multiples have a similar seismic response. Finally, by corendering the SHAP values with the seismic amplitudes, I perform an in-context interpretation to analyze how changes in the seismic reflectors impact the classification. I conclude that, based on the seismic attribute analyzed, an overlap among MTDs, salt, and conformal sediments exists in the study area.

Acknowledgments

Russell and to Schlumberger for the licenses in Petrel provided to the University of Oklahoma.

Appendix A

Adding band-limited noise to the seismic volume

Following Liu and Lin (2013), the amplitude of the AWGN is given by the Gaussian distribution:

$$N(\mu, \sigma) = \frac{1}{\sqrt{2\pi\sigma^2}} exp^{-\left[(x-\mu)^2/2\sigma^2\right]},$$ (A-1)

where μ is the mean, which is equal to zero and σ^2 is the variance of the distribution which is related to the power of the noise and requires careful estimation.

In addition, to generate random noise with a target noise level and estimate its standard deviation σ, I analyze the relationship between the S/N and the rms amplitudes of the original seismic volume and the noise. The S/N in linear scale is given by:

$$S/N = \frac{A^2_{rms,signal}}{A^2_{rms,noise}}$$ (A-2)

where $A_{rms,signal}$ is assumed to be the rms amplitude of the original seismic volume (Figure 3.1) and $A_{rms,noise}$ is the rms amplitude of the noise to be generated. Therefore, because σ^2 is related to the power of the noise, I approximate the standard deviation σ of the noise to:

$$\sigma = A_{rms,noise} = \frac{1}{\sqrt{S/N}} A_{rms,signal}$$ (A-3)

Moreover, because my seismic amplitude volume is band limited with an approximate bandwidth of 77.5 Hz (Figure 3.1b) and the estimated AWGN is characterized by flat spectrum with amplitudes seen in frequencies larger than 80 Hz (Figure 3.A-1a), I apply an Ormsby filter $O(t)$ to generate a band-limited random noise $\hat{N}$ given by

$$\hat{N} = N * O(t) \tag{A-4}$$

where

$$O(t) = \frac{f_1^2 \pi}{f_2 - f_1} Sinc^2(f_1 t) - \frac{f_2^2 \pi}{f_2 - f_1} Sinc^2(f_2 t) - \frac{f_3^2 \pi}{f_4 - f_3} Sinc^2(f_3 t) + \frac{f_4^2 \pi}{f_4 - f_3} Sinc^2(f_4 t) \tag{A-5}$$

and $f_{1,2,3,4}$ are the corner frequencies. In this study, I use the Ormsby filter with corner frequencies equal to f_1 = 5 Hz, f_2 = 10 Hz, f_3 = 60 Hz, and f_4 = 80 Hz, with a duration T = 500 ms and sampling interval Δt = 4 ms (Figure 3.A-1b).

Finally, I add the band-limited noise $\hat{N}$ (Figure 3.A-1c) to the original seismic volume A as

$$\hat{A} = A + \hat{N} \tag{A-6}$$

where $\hat{A}$ represents the seismic amplitude volume contaminated with random noise and target S/N = 2.

References

Amin A., M. Deriche, M. A. Shafiq, Z. Wang, and G. AlRegib, 2017, Automated salt dome detection using an attribute ranking framework with a dictionary-based classifier: Interpretation, **5**, no. 3, SJ61-SJ79, doi: 10.1190/INT-2016-0084.1.

Angelo, S.M, M. Matos, and K.J. Marfurt, 2009, Integrated seismic texture segmentation and clustering analysis to improved delineation of reservoir geometry: 79th Annual

International Meeting, SEG, Expanded Abstracts, 1107-1111, doi: 10.1190/1.3255046.

Bergstra, J., R. Bardenet, Y. Bengio, and B. Kégl, 2011, Algorithms for hyper-parameter optimization: Proceedings of the 24th International Conference of Neural Information Processing Systems, 2546-2554.

Bergstra, J., and Y. Bengio, 2012, Random search for hyper-parameter optimization: Journal of Machine Learning Research, **13**, 281-305.

Biau, G., L. Devroye, and G. Lugosi, 2008, Consistency of random forests and other averaging classifiers: Journal of Machine Learning Research, **9**, 2015-2033.

Breiman, L., 2001, Random forests: Machine Learning, **45**, 5–32, doi: 10.1023/A:1010933404324

Chang-kai Z., and L. Wen-kai, 2010, Seismic attributes selection based on SVM for hydrocarbon reservoir prediction: 80th Annual International Meeting, SEG, Expanded Abstracts, 1586-1590, doi: 10.1190/1.3513144.

Chopra, S., and V. Alexeev, 2006, Applications of texture attribute analysis to 3D seismic data: The Leading Edge, **25**, 934-940, doi: 10.1190/1.2335155

Chopra, S., and K. J. Marfurt, 2007, Seismic attributes for prospect identification and reservoir characterization, SEG, Geophysical Development Series 481.

Chopra, S., and K. J. Marfurt, 2013, Volumetric estimates of seismic reflector rotation and convergence – Tools for mapping rotation about faults and seismic stratigraphy: The Leading Edge, **32**, 402-408, doi: 10.1190/tle32040402.1

Chopra, S., and K.J. Marfurt, 2014, Churning seismic attributes with principal component analysis: 84th Annual International Meeting, SEG, Expanded Abstract, 2672-2676, doi: 10.1190/segam2014-0235.1.

Chopra, S., and K. J. Marfurt, 2016, Spectral decomposition and spectral balancing of seismic data: The Leading Edge, **35**, 176-179, doi: 10.1190/tle35020176.1.

Cross, T., K. Sathaye, K. Darnell, D. Niederhut, and K. Crifasi, 2020a, Benchmarking operator performance in the Williston Basin using a predictive machine learning model: Presented at the Unconventional Resources Technology Conference, SEG, Global Meeting Abstracts, 3881-3892, doi: 10.15530/urtec-2020-2750

Cross T., K. Sathaye, K. Darnell, D. Niederhut, and K. Crifasi, 2020b, Predicting water production in the Williston Basin using a machine learning model: Presented at the

Unconventional Resources Technology Conference, SEG, Global Meeting Abstracts, 3492-3503, doi: 10.15530/urtec-2020-2756

Cross, T., K. Sathaye, K. Darnell, J. Ramey, K. Crifasi, and D. Niederhut, 2020c, GeoSHAP: A novel method of deriving rock quality index from machine learning models and principal components analysis: Presented at the Unconventional Resources Technology Conference, SEG, Global Meeting Abstracts, 1056-1064, doi: 10.15530/urtec-2020-2743

Di, H., and D. Gao, 2017, Nonlinear gray-level co-occurrence matrix texture analysis for improved seismic facies interpretation: Interpretation, **5**, no.3, SJ31-SJ40, doi: 10.1190/INT-2016-0214.1.

Dorrington, K. P., and C. A. Link, 2004, Genetic-algorithm/neural-network approach to seismic attribute selection for well-log prediction: Geophysics, **69**, 212-221, doi: 10.1190/1.1649389

Genuer, R., J.-M. Poggi, C. Tuleau-Malot, and N. Villa-Vialaneix, 2017, Random forests for big data: Big Data Research, **9**, 28-46, doi: 10.1016/j.bdr.2017.07.003.

Gersztenkorn, A., and K. J. Marfurt, 1999, Eigenstructure-based coherence computations as an aid to 3-D structural and stratigraphic mapping: Geophysics, **64**, 1468-1479, doi: 10.1190/1.1444651

Guo, H., K. J. Marfurt, and J. Liu, 2009, Principal component spectral analysis: Geophysics, **74**, no. 4, P35–P43, doi: 10.1190/1.3119264.

Hampson, D.P., J. S. Schuelke, J.A. Quirein, 2001, Use of multiattribute transforms to predict log properties from seismic data: Geophysics, **66**, 220-236, doi: 10.1190/1.1444899.

Haralick, R. M., K. Shanmugam, and I Dinstein, 1973, Textural features for image classification: IEEE Transactions on Systems, Man and Cybernetics, **SMC-3**, 610-621, doi: 10.1109/TSMC.1973.4309314.

Honorio, B., A. Sanchetta, E. Pereira, and A. Vidal, 2014, Independent component spectral analysis: Interpretation, **2**, no. 1, SA21-SA29, doi: 10.1190/INT-2013-0074.1.

Jain, A., K. Nandakumar, and A. Ross, 2005, Score normalization in multimodal biometric systems: Pattern Recognition, **38**, 2270-2285, doi: 10.1016/j.patcog.2005.01.012

Jones, I. F., and I. Davison, 2014, Seismic imaging in and around salt bodies: Interpretation, **2**, no. 4, SL1-SL20, doi: 10.1190/INT-2014-0033.1.

Kim, Y., R. Hardisty, and K. J. Marfurt, 2019, Attribute selection in seismic facies classification: Application to a Gulf of Mexico 3D seismic survey and the Barnett Shale: Interpretation, **7**, SE281–SE297, doi: 10.1190/INT-2018-0246.1.

Lerza A., J. J. Fernandez, A. Marlats, and D. Gallart, 2020, Case of study: Applying data analytics to reveal most important parameters impacting well production performance in Vaca Muerta unconventional formation: Latin America Unconventional Resources Technology Conference, SEG, Global Meeting Abstracts, 1-16, doi: 10.15530/urtec-2020-1350

Li, F., and W. Lu, 2014, Coherence attribute at different spectral scales: Interpretation, **2**, no. 1, SA99–SA106, doi: 10.1190/INT-2013-0089.1.

Liu, W., and W. Lin, 2013, Additive white Gaussian noise level estimation in SVD domain for images: IEEE Transactions on Image Processing, **22**, 872-883, doi: 10.1109/TIP.2012.2219544

Lubo-Robles, D., T. Ha, S. Lakshmivarahan, K. J. Marfurt, and M. J. Pranter, 2021, Exhaustive probabilistic neural network for attribute selection and supervised seismic facies classification: Interpretation, **9**, no. 2, T421-T441, doi: 10.1190/INT-2020-0102.1

Lubo-Robles, D., and K. J. Marfurt, 2019, Independent component analysis for reservoir geomorphology and unsupervised seismic facies classification in the Taranaki Basin, New Zealand: Interpretation, **7**, no. 3, SE19–SE42, doi: 10.1190/INT-2018-0109.1

Lundberg, S., and S. Lee, 2017, A unified approach to interpreting model predictions: Proceedings of the 31st Conference on Neural Information Processing Systems, 4765-4774.

Lundberg, S. M., G. Erion, H. Chen, A. DeGrave, J. M. Prutkin, B. Nair, R. Katz, J. Himmelfarb, N. Bansal, and S. Lee, 2020, From local explanations to global understanding with explainable AI for trees: Nature Machine Intelligence, **2**, 56-57, doi: 10.1038/s42256-019-0138-9.

Lundberg, S. M., G. G. Erion, and S. Lee, 2018a, Consistent individualized features attribution for tree ensembles: arXiv preprint arXiv:1706.06060

Lundberg, S. M., B. Nair, M. S. Vavilala, M. Horibe, M. J. Eisses, T. Adams, D. E. Liston, D. K.-W. Low, S. Newman, J. Kim, and S.-I. Lee, 2018b, Explainable machine-learning predictions for the prevention of hypoxaemia during surgery: Nature Biomedical Engineering, **2**, 749-760, doi: 10.1038/s41551-018-0304-0.

Marfurt, K. J., and R.L. Kirlin, 2001, Narrow-band spectral analysis and thin-bed tuning: Geophysics, **66**, 1274–1283, doi: 10.1190/1.1487075.

Marfurt, K. J, and J. Rich, 2010, Beyond curvature- Volumetric estimates of reflector rotation and convergence: 80th Annual International Meeting, SEG, Expanded Abstracts, 1467-1472, doi: 10.1190/1.3513118.

Matos, M., M. Yenugu, S. M. Angelo, and K. J. Marfurt, 2011, Integrated seismic texture segmentation and cluster analysis applied to channel delineation and chert reservoir characterization: Geophysics, **76**, no. 5, P11-P21, doi: 10.1190/geo2010-0150.1

Meyer, D. E., E. L. Harvey, T. E. Bulloch, J. C. Voncannon, and T. M. Sheffield, 2001, Use of seismic attributes in 3-D geovolume interpretation: The Leading Edge, **20**, 1377–1400, doi: 10.1190/1.1486768.

Molnar, C., 2021, Interpretable machine learning: A guide for making black box models explainable, https://christophm.github.io/interpretable-ml-book/shap.html, accessed 11 August 2021.

Pedregosa F., G. Varoquaux, A. Gramfort, V. Michel, B. Thirion, O. Grisel, M. Blondel, P. Prettenhofer, R. Weiss, V. Dubourg, J. Vanderplas, A. Passos, D. Cournapeau, M. Brucher, M. Perrot, and E. Duchesnay, 2011, Scikit-learn: Machine learning in Python: Journal of Machine Learning Research, **12**, 2825-2830.

Posamentier, H. W., and V. Kolla, 2003, Seismic geomorphology and stratigraphy of depositional elements in deep-water settings. Journal of Sedimentary Research **73**, 367-388, doi: 10.1306/111302730367.

Qi, J., T. Lin, T. Zhao, F. Li, and K. J. Marfurt, 2016, Semisupervised multiattribute seismic facies analysis: Interpretation, **4**, no. 1, SB91-SB106, doi: 10.1190/INT-2015-0098.1

Qi J., and K. Marfurt, 2019, Nonparallelism attributes and data adaptive Kuwahara image processing: 89th Annual International Meeting, SEG, Expanded Abstracts, 1858-1861, doi: 10.1190/segam2019-3216022.1.

Qi J., B. Zhang, B. Lyu, and K. Marfurt, 2020, Seismic attribute selection for machine-learning-based facies analysis: Geophysics, **85**, no. 2, O17-O35, doi: 10.1190/geo2019-0223.1.

Qian, Y., F. Male, S. A. Ikonnikova, K. Smye, G. McDaid, and E. Goodman, 2020, Permian Delaware basin Wolfcamp a formation productivity analysis and technically recoverable resource assessment: Proceedings of the Unconventional Resources Technology Conference, SEG, Global Meeting Abstracts, 561-570, doi: 10.15530/urtec-2020-3167

Ribeiro, M. T., S. Singh, C. Guestrin, 2016, Why should I trust you? Explaining the predictions of any classifier: Proceedings of the 22nd ACM SIGKDD International Conference on Knowledge Discovery and Data Mining, 1135-1144.

Roden, R., T. Smith, and D. Sacrey, 2015, Geologic pattern recognition from seismic attributes: Principal component analysis and self-organizing maps: Interpretation, **3**, no. 4, SAE59–SAE83, doi: 10.1190/INT-2015-0037.1.

Roy, A., A. S. Romero-Peláez, T. J. Kwiatkowski, and K. J. Marfurt, 2014, Generative topographic mapping for seismic facies estimation of a carbonate wash, Veracruz Basin, southern Mexico: Interpretation, **2**, no. 1, SA31-SA47, doi: 10.1190/INT-2013-0077.1.

Sathaye, K., T. Cross, K. Darnell, J. Reed, J. Ramey, and D. Niederhut, 2020, The impact of interwell spacing over time — A machine learning approach: Unconventional Resources Technology Conference, SEG, Global Meeting Abstracts, 2962-2970, doi: 10.15530/urtec-2020-2800

Scornet, E., G. Biau, and J-P. Vert, 2015, Consistency of random forests: Annals of Statistics, Institute of Mathematical Statistics (IMS), **43**, 1716-1741, doi: 10.1214/15-AOS1321

Sinha S., P. Routh, P. Anno, and J. Castagna, 2005, Spectral decomposition of seismic data with continuous-wavelet transform: Geophysics, **70**, no. 6, P19-P25, doi: 10.1190/1.2127113.

Tran, N. L., I. Gupta, D. Devegowda, V. Jayaram , H. Karami, C. S. Rai, and C. Sondergeld, 2020, Application of interpretable machine-learning workflows to identify brittle, fracturable, and producible rock in horizontal wells using surface drilling data: SPE Reservoir Evaluation and Engineering, **23**, 1328-1342, doi: 10.2118/202486-PA

Walden, A.T., 1985, Non-Gaussian reflectivity, entropy, and deconvolution: Geophysics, **50**, 2862–2888, doi: 10.1190/1.1441905.

Wang, Z., C. Yin, X. Lei, F. Gu, and J. Gao, 2015, Joint rough sets and Karhunen-Loève transform approach to seismic attribute selection for porosity prediction in a Chinese sandstone reservoir: Interpretation, **3**, no. 4, SAE19–SAE28, doi:10.1190/INT-2014-0268.1.

Wu X., L. Liang, Y. Shi, and S. Fomel, 2019, FaultSeg3D: Using synthetic data sets to train an end-to-end convolutional neural network for 3D seismic fault segmentation: Geophysics, **84**, no.3, IM35-IM45, doi: 10.1190/geo2018-0646.1.

Yenugu, M., K. J. Marfurt, and S. Matson, 2010, Seismic texture analysis for reservoir prediction and characterization: The Leading Edge, **29**, 1116-1121, doi: 10.1190/1.3485772

Zhang, K, K. J. Marfurt, and Y. Gao, 2008, Volumetric application of skewed data: 78th Annual International Meeting, SEG, Expanded Abstracts, 919-923, doi: 10.1190/1.3063789.

Zhao, T., V. Jayaram, A. Roy, and K. J. Marfurt, 2015, A comparison of classification techniques for seismic facies recognition: Interpretation, **3**, no. 4, SAE29–SAE58, doi: 10.1190/INT-2015-0044.1.

Zhao, T., J. Zhang, F. Li, and K. J. Marfurt, 2016, Characterizing a turbidite system in Canterbury Basin, New Zealand, using seismic attributes and distance-preserving self-organizing maps: Interpretation, **4**, no.,1, SB79-SB89, doi: 10.1190/INT-2015-0094.1.

Chapter 3 Figures
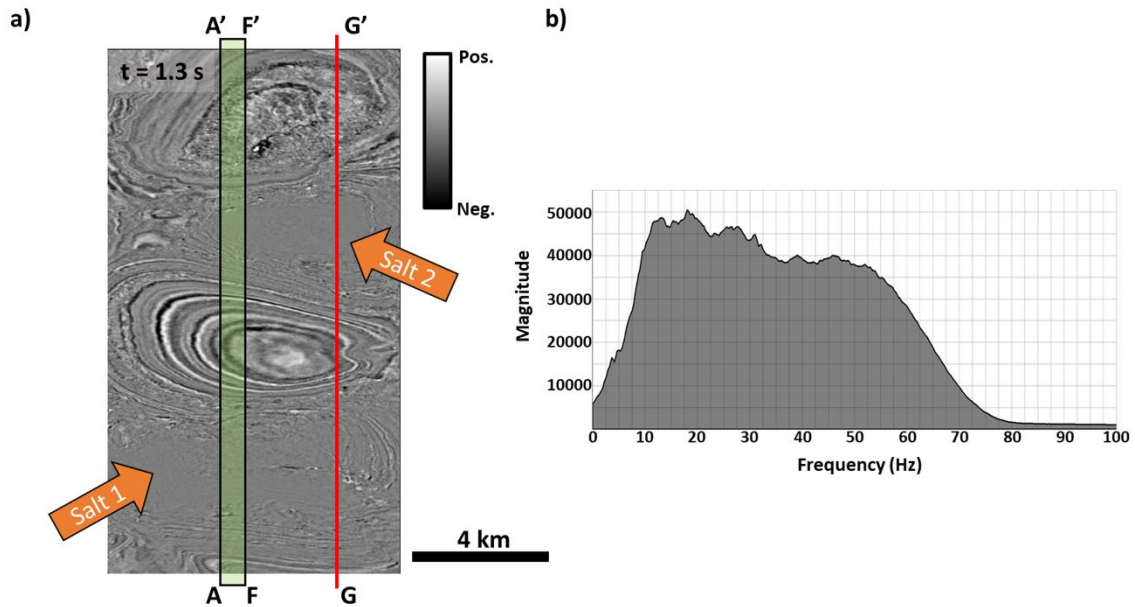
Figure 3.1. The 3D seismic survey used in the study is located in the Gulf of Mexico, offshore Louisiana. (a) Seismic amplitude volumes at time slice $t = 1.3$ s. Chaotic seismic reflectors seen in the area are interpreted as two salt diapirs (the orange arrows). Six equally spaced lines are used to generate the training and validation data sets (the green rectangle), and vertical section GG' is used to analyze how the random forest architecture predicts in the presence of previously unseen data. (b) Amplitude spectrum of the seismic volume. The data set is characterized by frequencies ranging from 2.5 Hz to 80 Hz and seismic bandwidth of approximately 77.5 Hz.
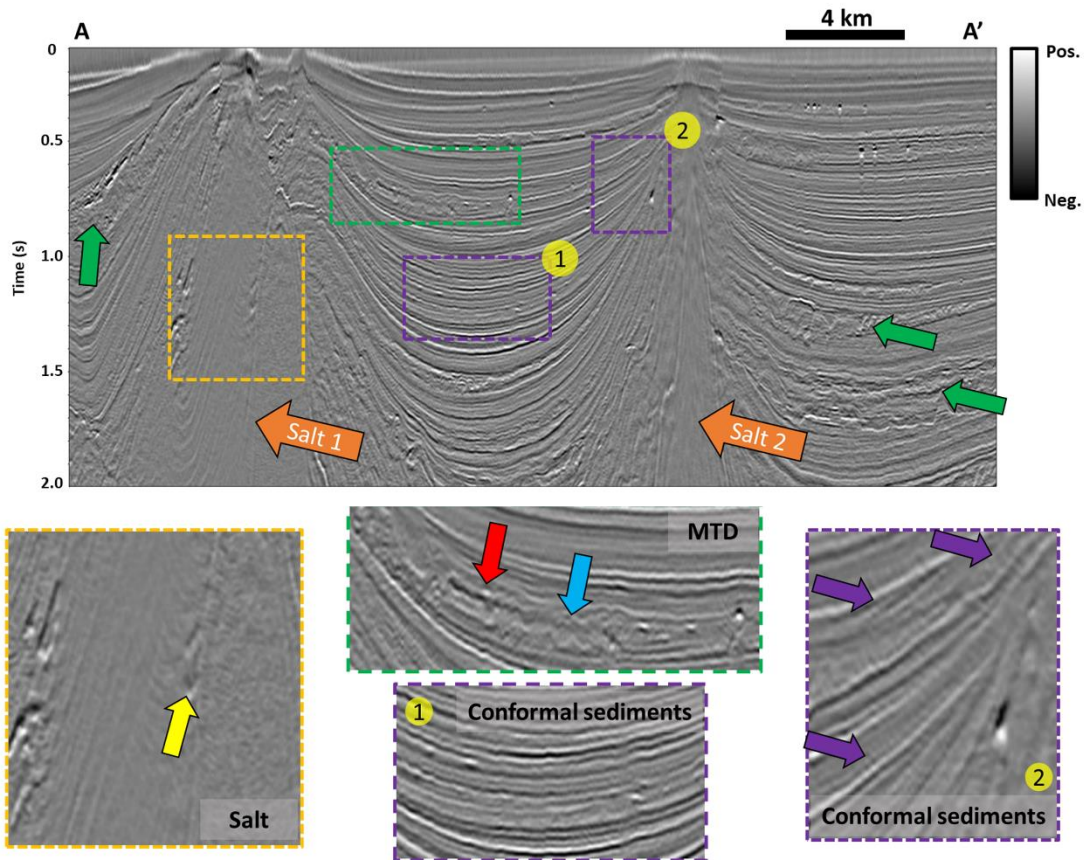
Figure 3.2. Seismic response of target seismic facies MTD, salt, and conformal sediments using a suite of magnified vertical sections along AA'. Salt diapirs (the orange arrows) are characterized by low-amplitude chaotic reflectors associated with random coherent noise. In addition, crossing coherent noise is visible inside salt diapirs (the yellow arrow) related to migration artifacts due to higher P-wave velocities compared with the surrounding strata and the geometry of the salt (Jones and Davison, 2014). MTDs (the green arrows) tend to be highly heterogenous with intercalations of more coherent, rotated blocks (the red arrow) and lower amplitude, discontinuous, and chaotic reflectors possibly related to shaley intervals (the blue arrow). Finally, the conformal sediments or background formations are characterized by high-amplitude coherent reflectors (the purple rectangle 1). However, conformal sediments close to the edges of the salt show a rapid change in the amplitudes and dips and low-frequency noise (the purple arrows). These conformal sediments are characterized by lower seismic amplitudes and a reduction in the quality of the seismic image (the purple rectangle 2).

112

Figure 3.3. Sensitivity analysis, seismic facies classification, and application of SHAP values for model interpretation workflow. Three cases are generated to analyze how different perturbations made to the input attributes affect the classification: case 1 considers the seismic attributes computed from the original volume; case 2 applies a 3D Kuwahara filter (Qi et al., 2016; Lubo-Robles et al., 2021) to remove noise, sharpen the edges between seismic facies, and smooth their internal response; and case 3 adds band-limited AWGN with S/N = 2 to the entire survey and recomputes the seismic attributes using the same parameters as case 1. I select a suite of candidate seismic attributes based on my geologic insight and experience to differentiate between the target seismic facies. Then, I generate the training and validation data sets by manually picking a group of polygons enclosing each of the target seismic facies. Moreover, I apply a Min-Max scaler (Jain et al., 2005; Pedregosa et al., 2011) to remove scale dependency in the seismic attributes. Then, considering the seismic attributes from case 1, I perform a hyperparameter search and apply fivefold cross validation to find the most optimal hyperparameters to train a random forest architecture. The same hyperparameters are used for cases 2 and 3 to make an unbiased sensitivity analysis. Finally, I apply a SHAP TreeExplainer (Lundberg and Lee, 2017; Lundberg et al., 2018a) to compute the SHAP values and explain the outputs of the models. The SHAP global feature importance, SHAP local explanation summary plots, and SHAP dependence plots provide a means to determine the global importance of each seismic attribute and understand the global behavior of the model (Lundberg et al., 2018a, 2020; Molnar, 2021). Using SHAP force plots, I study how seismic attributes are used by the random forest model to perform a seismic facies prediction at voxels of interest in the study area. In addition, by corendering the SHAP values with the seismic amplitude volume, I analyze how variations in the seismic response might affect the facies predictions.

Case 1: Seismic attributes
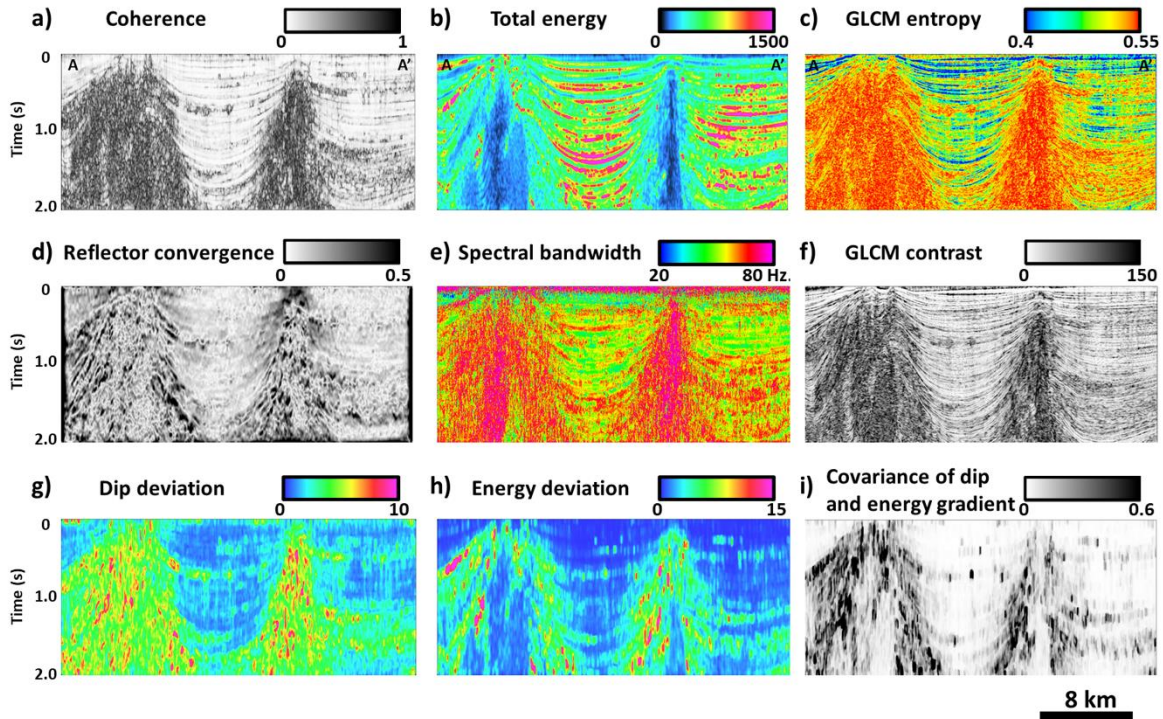
Figure 3.4. Original seismic attributes for case 1 along line AA'. (a) Coherence, (b) total energy, (c) GLCM entropy, (d) reflector convergence, (e) spectral bandwidth, (f) GLCM contrast, (g) dip deviation, (h) energy deviation, and (i) covariance of dip and energy gradient. I observe that the salt diapirs are characterized by lower coherence, and higher entropy, contrast, and spectral bandwidth than the higher energy, more coherent background conformal sediments. MTDs exhibit higher variability in their seismic response due to the presence of rotated blocks embedded in a discontinuous chaotic matrix. Finally, rapid changes in dips, energy, and reflector convergence are visible close to the edges of the salt diapirs.

114

Case 2: Kuwahara-filtered seismic attributes
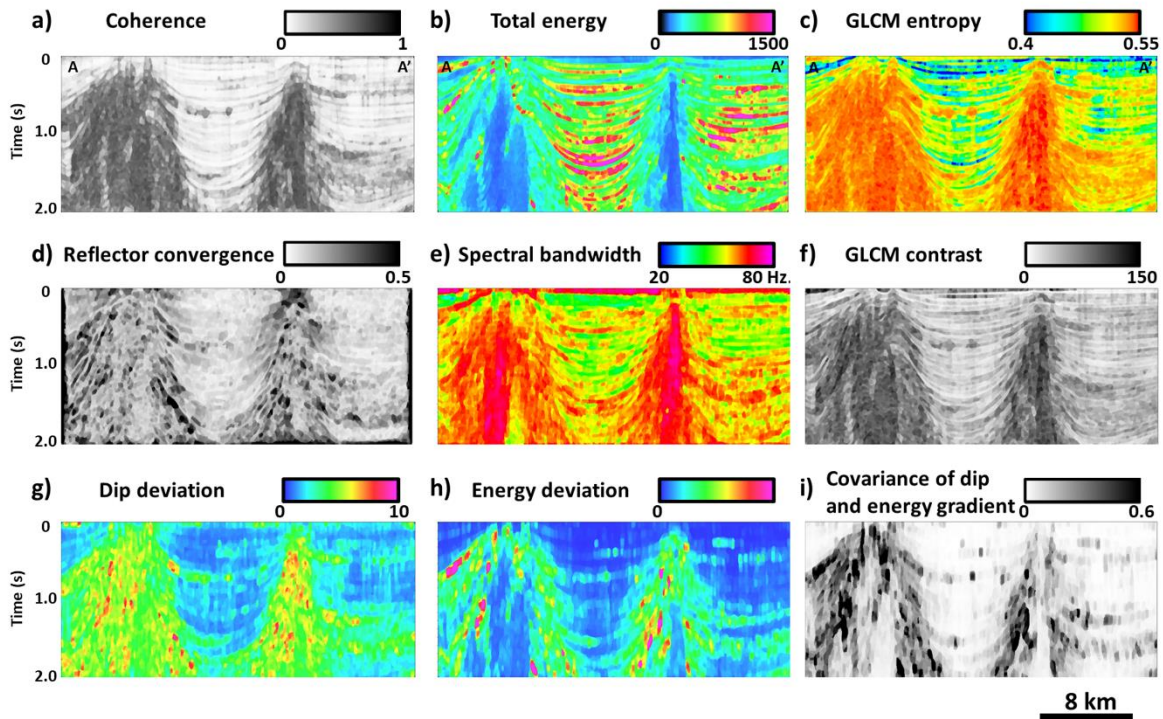
Figure 3.5. Seismic attributes along line AA' after applying Kuwahara filtering. (a) Coherence, (b) total energy, (c) GLCM entropy, (d) reflector convergence, (e) spectral bandwidth, (f) GLCM contrast, (g) dip deviation, (h) energy deviation, and (i) covariance of dip and energy gradient. Seismic noise has been strongly reduced by the Kuwahara filter in the entire survey. Moreover, the target seismic facies are blocked and show smoother internal response and sharper edges.
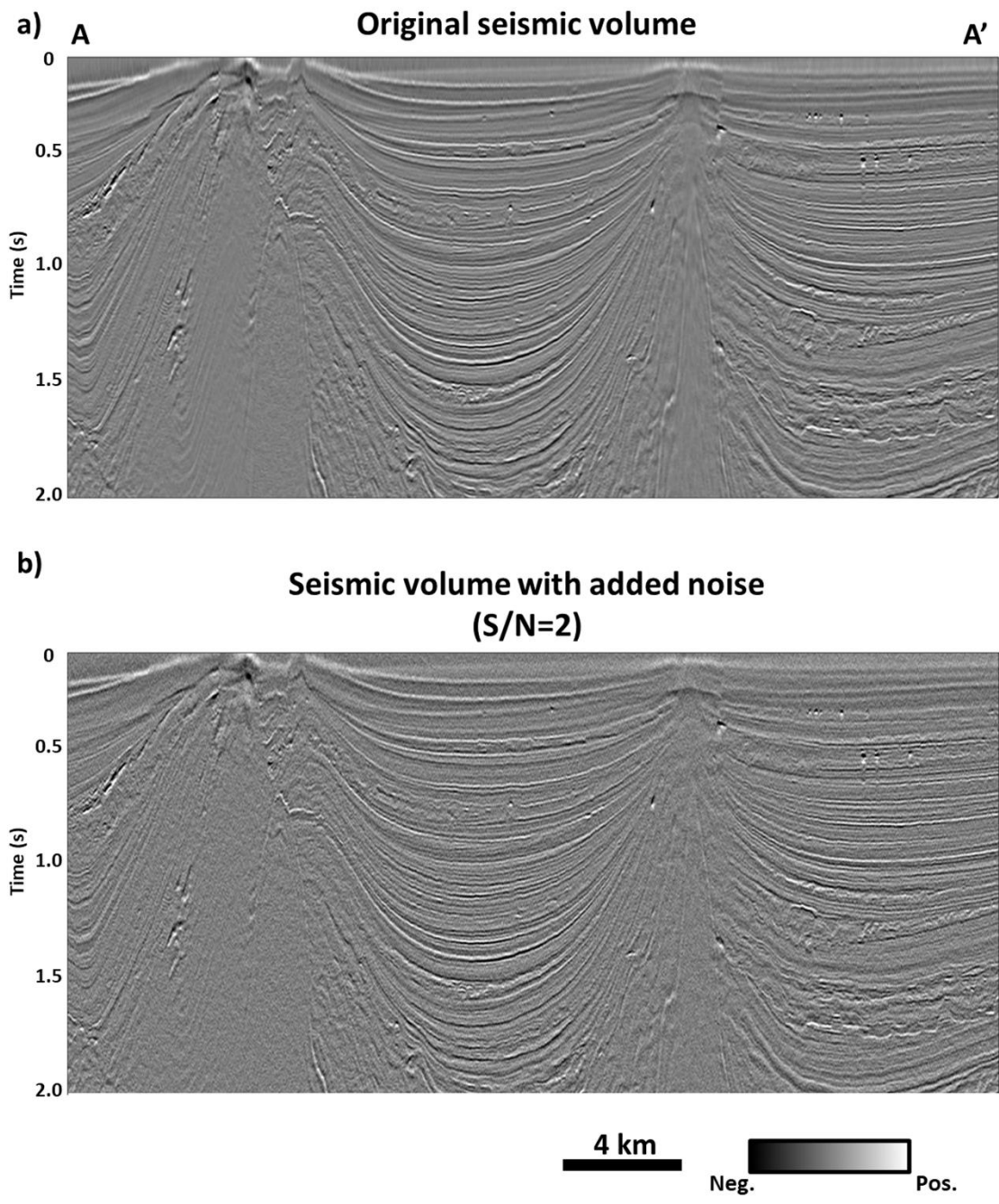
Figure 3.6. Seismic volume (a) before and (b) after adding band-limited AWGN with S/N = 2. As expected, an increase in the salt-and-pepper appearance in the entire seismic volume is seen when adding random noise.
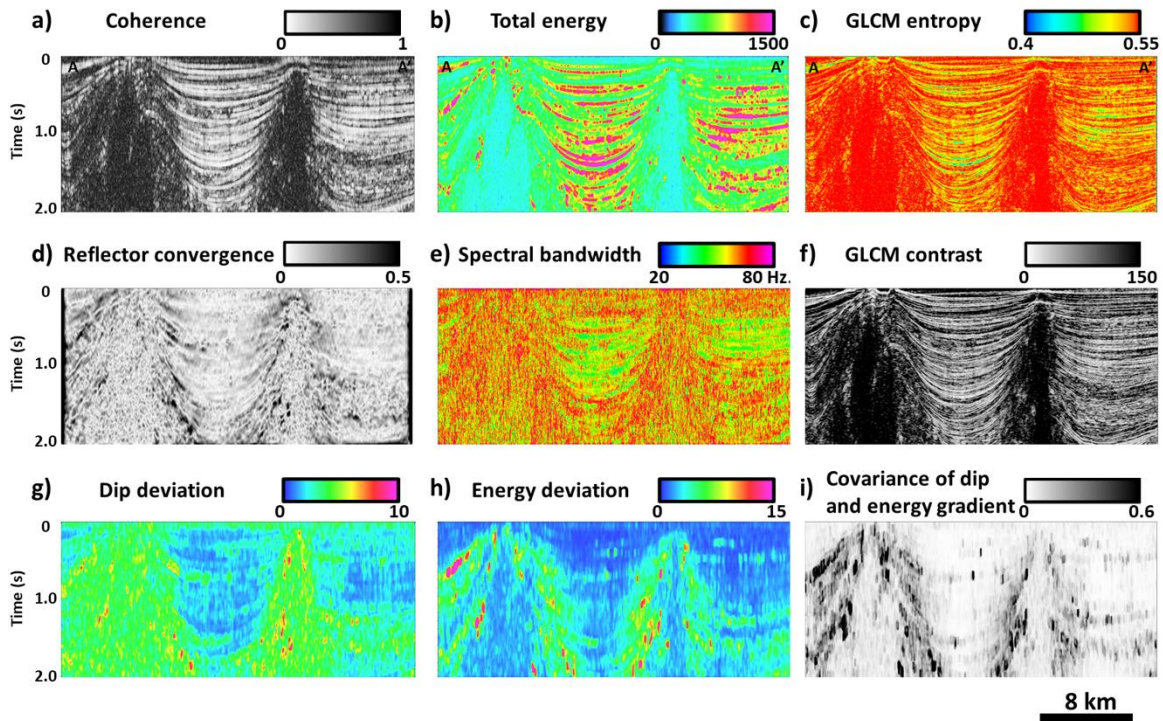
Figure 3.7. Seismic attributes along line AA' after adding band-limited random noise to the entire seismic volume. (a) Coherence, (b) total energy, (c) GLCM entropy, (d) reflector convergence, (e) spectral bandwidth, (f) GLCM contrast, (g) dip deviation, (h) energy deviation, and (i) covariance of dip and energy gradient. Due to the increasing noise in the MTDs and background geology, there is a poorer discrimination between seismic facies compared with the original candidate seismic attributes in case 1.
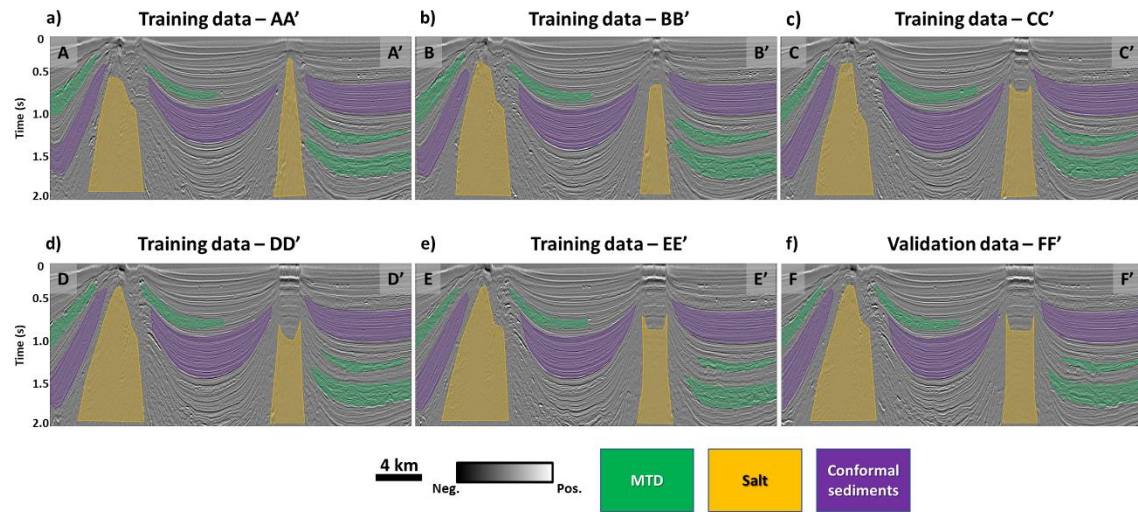
Figure 3.8. Training and validation data sets definitions. (a-e) The training data are generated by manually picking a suite of polygons enclosing the MTD (the green polygons), salt (the orange polygons), and conformal sediments (the purple polygons) seismic facies. (f) Validation data set along line FF' enclosing the target seismic facies.
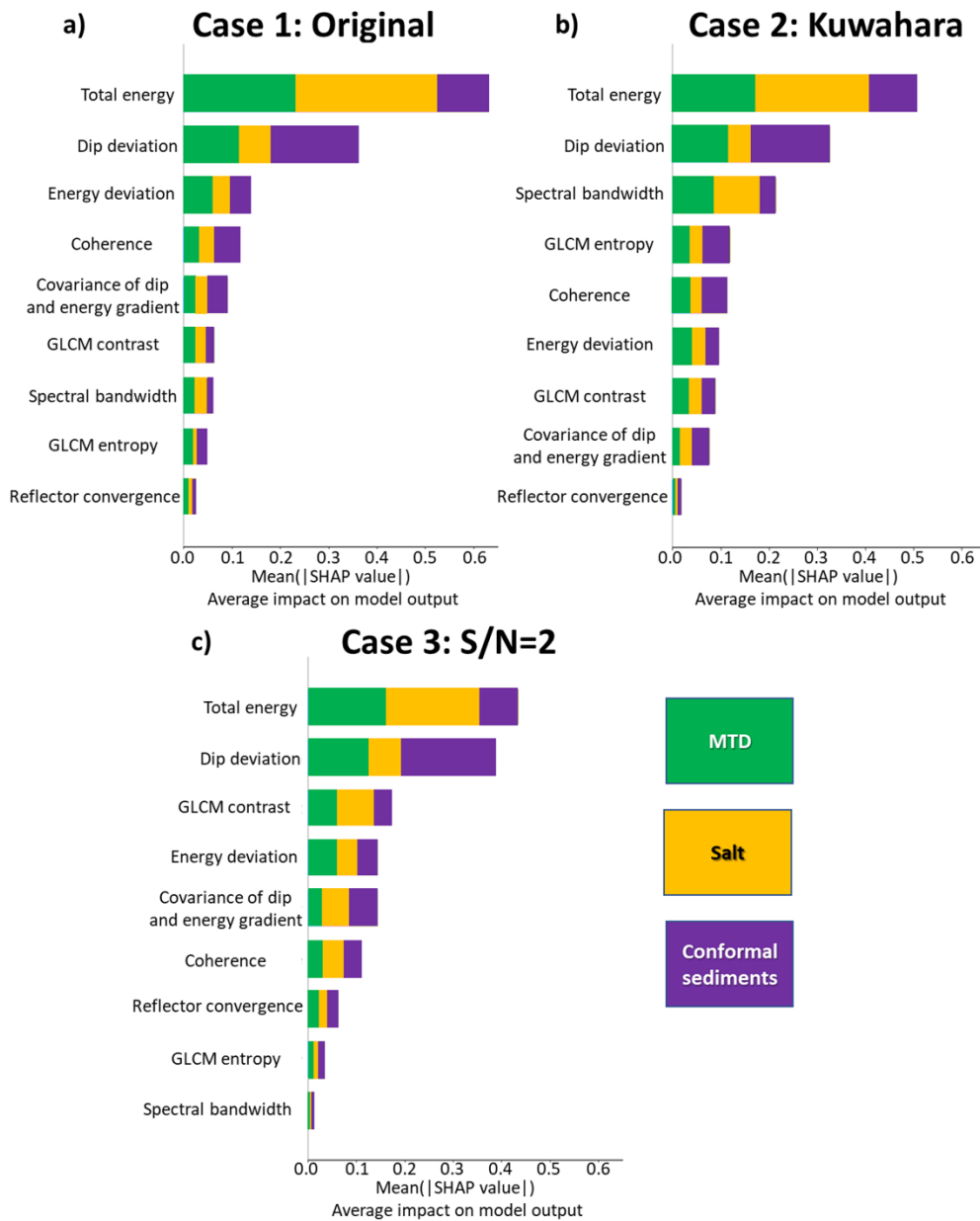
Figure 3.9. Average SHAP values for each candidate seismic attribute and each case study. The highest contribution to the classification is given by the total energy followed by the dip deviation, energy deviation, coherence, covariance of dip and energy gradient, GLCM contrast, spectral bandwidth, GLCM entropy, and reflector convergence when using the original data (case 1). Moreover, the attribute importance is very similar with a few differences when considering cases 2 and 3.
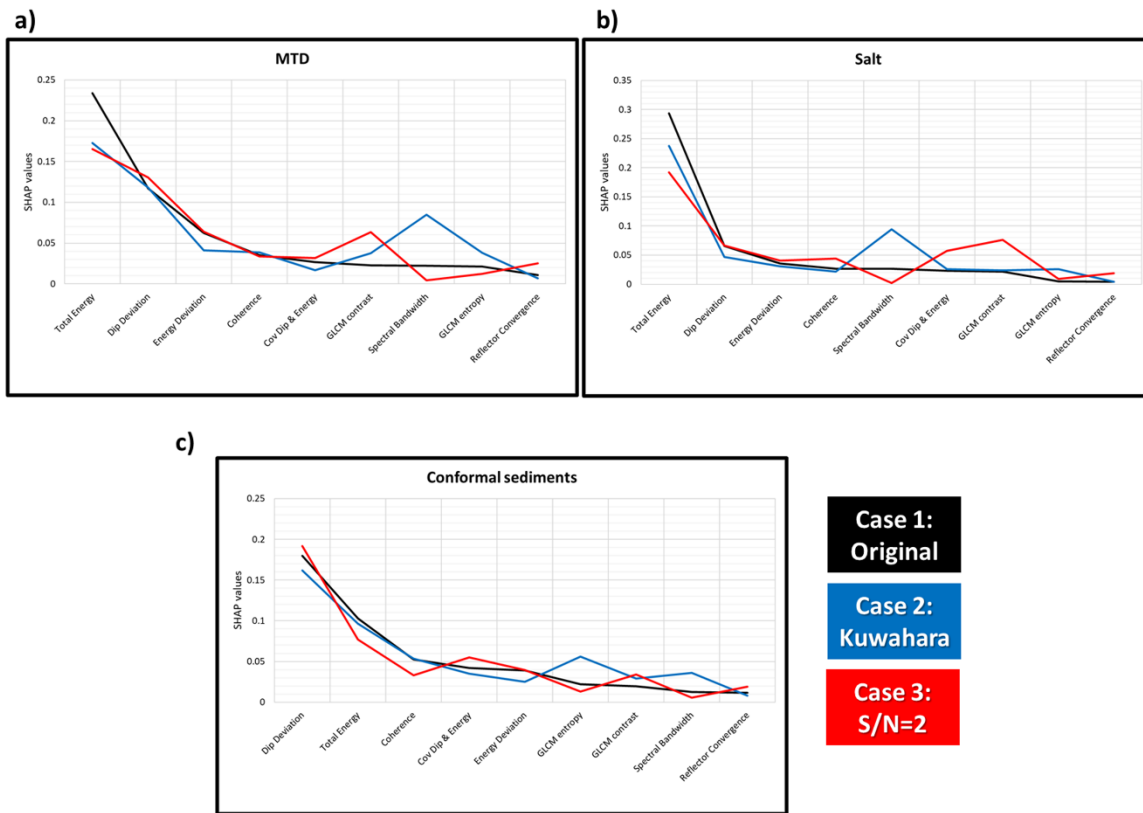
Figure 3.10. Importance of each seismic attribute to the classification for each seismic facies. For case 1, the MTD and salt facies show that the most important attributes are given by the total energy, followed by the dip deviation. However, for conformal sediments, dip deviation becomes the most important attribute followed by the total energy. For MTD, the attribute importance when considering case 1 is the same as the overall importance (Figure 3.9a) and relative changes in the attribute importance remain similar for cases 2 (Figure 3.9b) and 3 (Figure 3.9c). For salt, spectral bandwidth becomes the second most important attribute for the classification when applying Kuwahara filtering, while the GLCM contrast shows a large increase in its importance in the presence of strong random noise (case 3). Finally, for conformal sediments, GLCM entropy and spectral bandwidth become the third and fifth most important attributes in the classification when analyzing case 2. Moreover, when adding band-limited noise, the GLCM contrast shows a slight increase in its importance and becomes the fifth most important attribute, whereas the coherence shows a decrease in its importance.

Figure 3.11. The SHAP summary plots. Each dot represents an individual voxel of the training data set. The *y*-axis is associated with the attribute importance for each seismic facies, whereas the *x*-axis represents the SHAP value for each seismic attribute in the classification (Lundberg et al., 2020; Molnar, 2021). I observe that the attribute's effects are similar for all cases with only some differences. (a-c) For MTD, high to medium values of total energy, high values of dip deviation, energy deviation, and GLCM entropy, and low values of coherence, covariance of dip and energy gradient, GLCM contrast, and spectral bandwidth tend to increase the probability of having MTDs. (d-f) High values of dip deviation, GLCM contrast, and spectral bandwidth, and low values of total energy, energy deviation, coherence, covariance of dip and energy gradient, and reflector convergence increase the probability for the salt seismic facies. (g-i) Finally, for conformal sediments, low values of dip deviation and energy deviation, high values of coherence and covariance of dip and energy gradient, medium values of spectral bandwidth, and low to high values of GLCM contrast are increasing the probability.

SHAP dependence plots: Total Energy
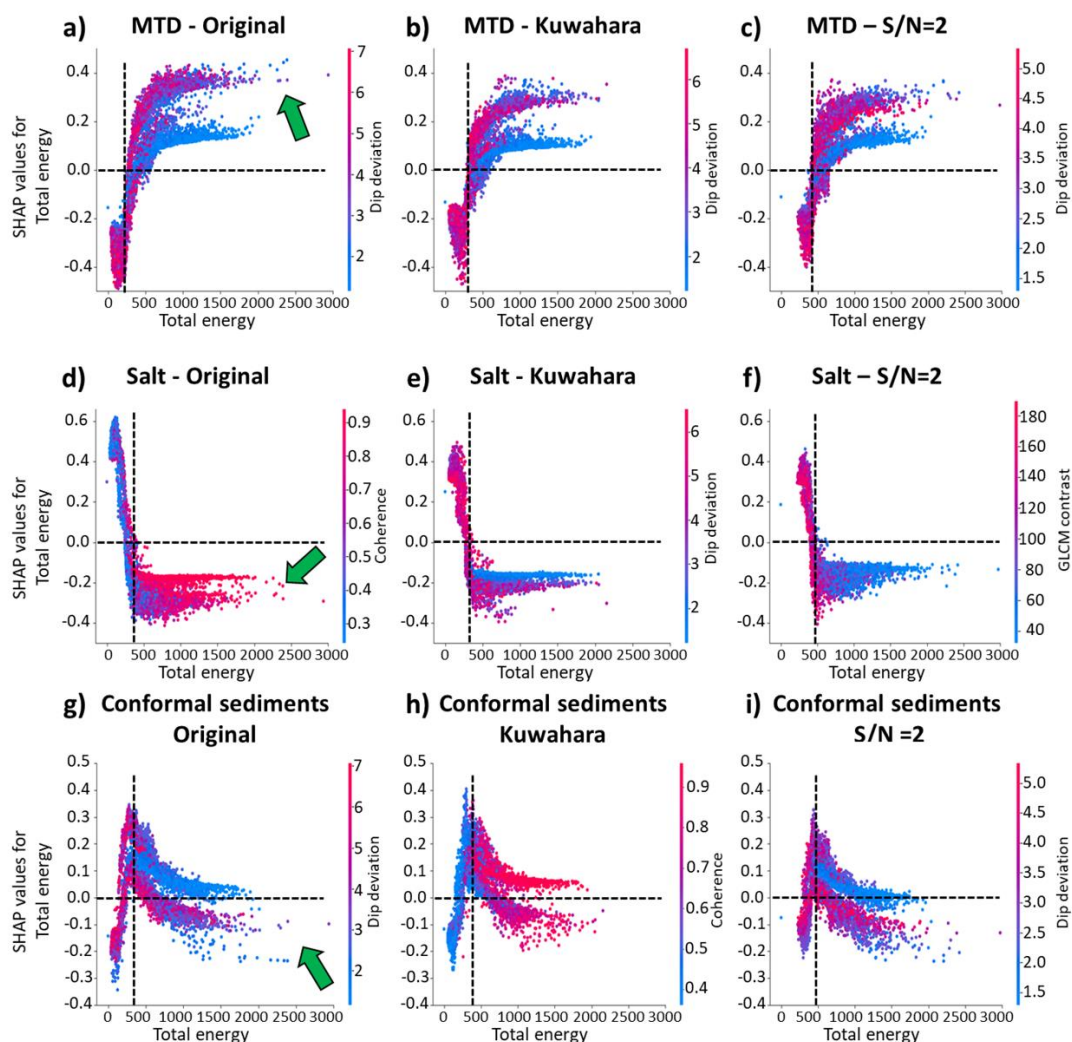
Figure 3.12. The SHAP dependence plot for total energy. Kuwahara filtering removes outliers in the data (the green arrows). (a-c) Two trends increasing the probability of having MTDs are visible: (1) values of total energy larger than approximately 400 and high dip deviation and (2) values of total energy larger than 400 and low dip deviation. (d-f) Values of total energy lower than 400 with low coherence and high dip deviation increase the probability of having salt seismic facies for cases 1 and 2, whereas values of total energy lower than approximately 500 and high values of GLCM contrast are increasing the probability for this seismic facies in the presence of noise (case 3). (g-i) For conformal sediments, (1) values of total energy lower than approximately 400-500 with high values of dip deviation and low values of coherence and (2) values of total energy larger than 400-500 with low values of dip deviation and high values of coherence are increasing the probability. Please note that the attribute's values in the *x*-axis are shown without scaling for interpretational purposes.

SHAP dependence plots: Dip deviation
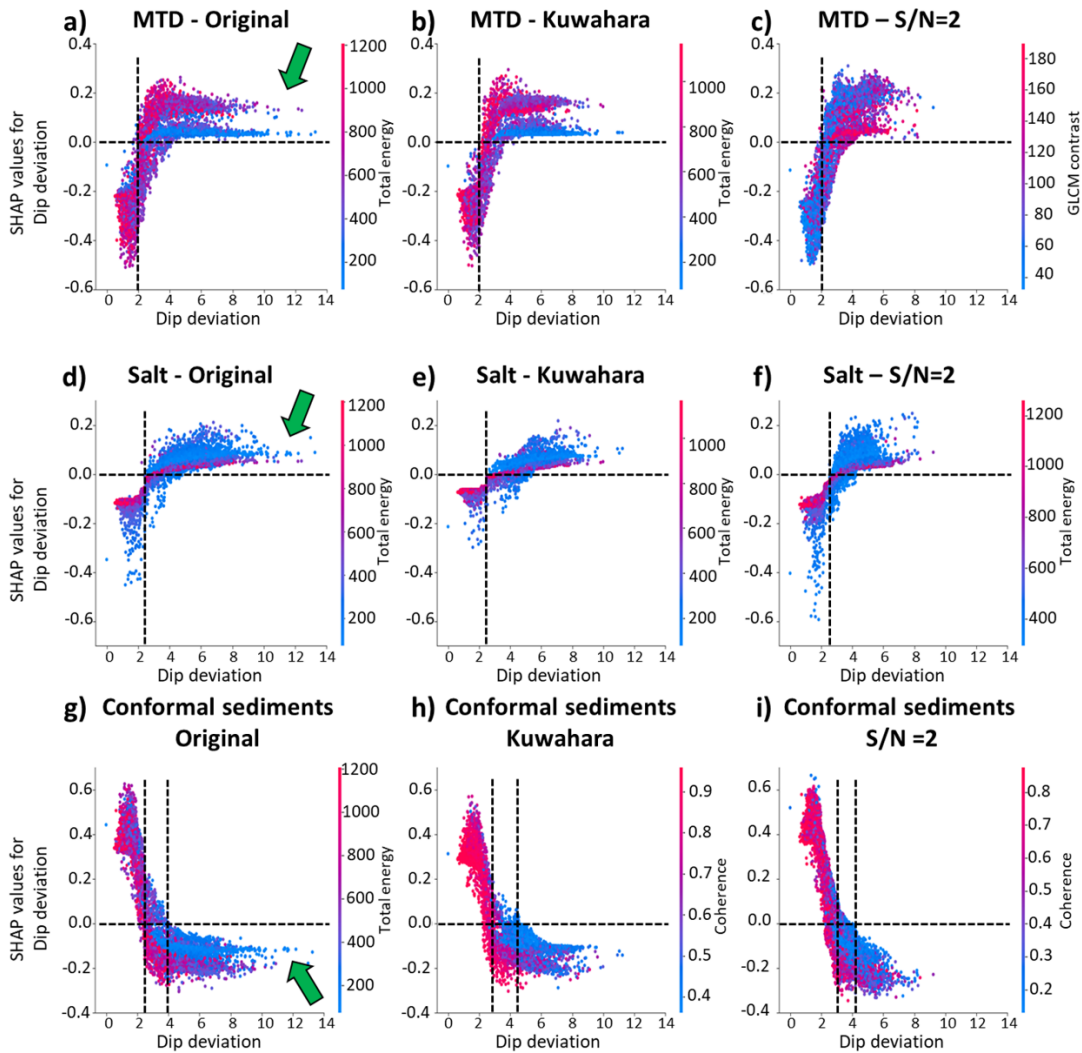
Figure 3.13. The SHAP dependence plot for dip deviation. Kuwahara filtering removes outliers in the data (the green arrows). (a-c) For MTD seismic facies, the trends of (1) values of dip deviation larger than approximately 2 with high values of total energy and low values of GLCM contrast and (2) values of dip deviation larger than 2 and low values of total energy and high values of GLCM contrast are increasing the probability. (d-f) For the salt seismic facies, values of dip deviation larger than approximately 2.5 and lower values of total energy are increasing the probability of a voxel being classified as salt. Moreover, some voxels characterized by higher total energy also increase the probability. (g-i) Two trends increasing the probability of having conformal sediments are visible: (1) values of dip deviation lower than 2.5 and higher values total energy and coherence and (2) values of dip deviation between 2.5 and 4 with lower values of total energy and coherence. Please note that the attribute's values in the *x*-axis are shown without scaling for interpretational purposes.
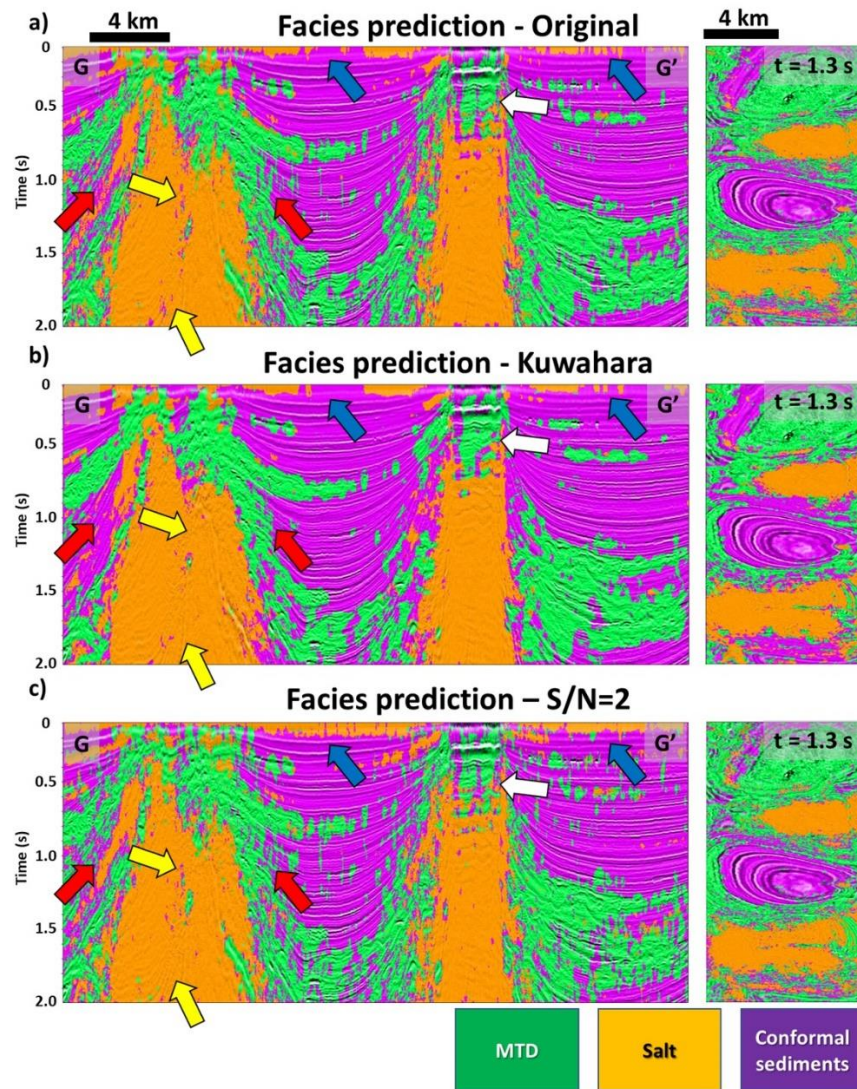
Figure 3.14. Random forest facies prediction corendered with the seismic amplitude along line GG' and at time slice $t = 1.3$ s for (a) case 1 using original seismic attributes, (b) case 2 applying Kuwahara filtering, and (c) case 3 adding band-limited random noise to the entire survey. In general, the ML model correctly classifies among MTDs (the green facies), salt (the orange facies), and conformal sediments (the purple facies). However, the results obtained for case 2 offer a smoother facies response, sharper edges, and better classification of previously unseen voxels compared to cases 1 and 3. Coherent migration artifacts inside salt diapirs (the yellow arrows) are misclassified as MTDs or conformal sediments, whereas noisy data in the edges of the survey (the blue arrows) tend to be misclassified as salt. Note that dipping conformal reflectors show some overlap with the MTD and salt seismic facies. These reflectors are more prone to be misclassified as salt or MTDs (the red arrows) in cases 1 and 3. At time slice $t = 1.3$ s, case 2 still offers the most optimal facies prediction with less conformal sediments voxels being misclassified as MTDs or salt.

124

Probability volumes
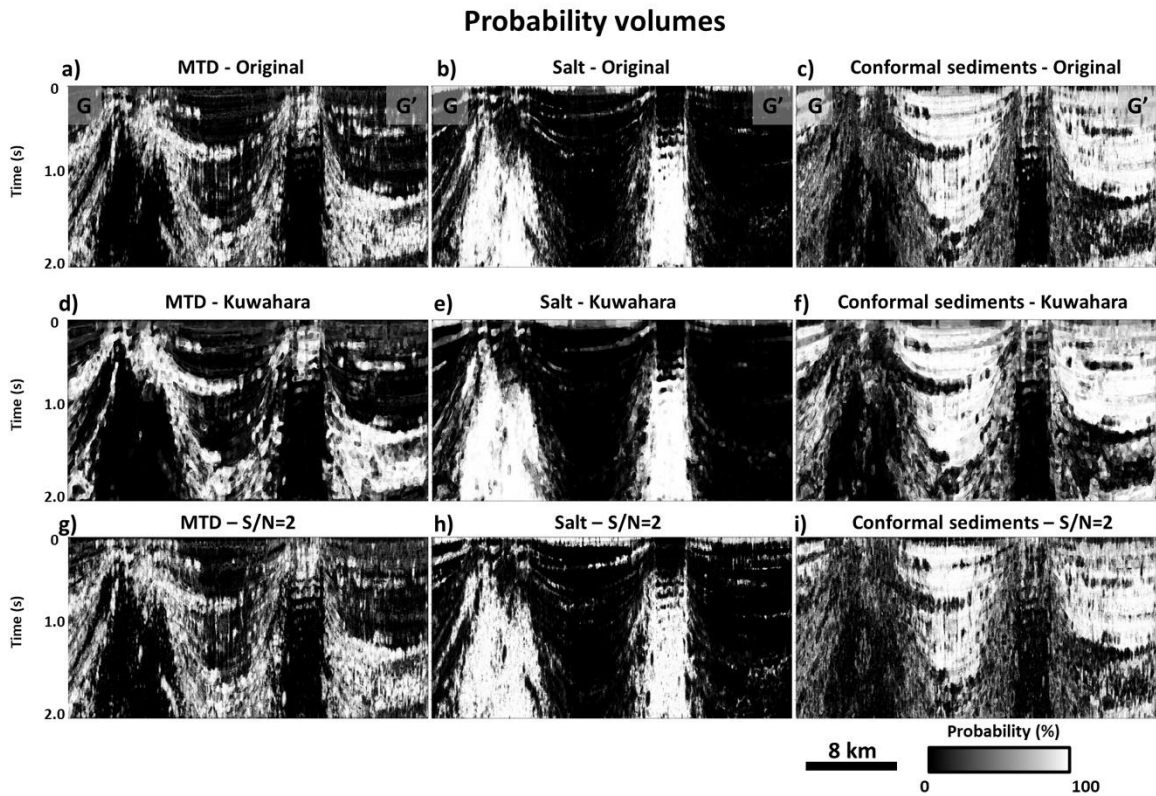
Figure 3.15. Random forest probability volumes along line GG' for all cases and seismic facies. (a) Case 1 using original seismic attributes, (b) case 2 applying Kuwahara filtering, and (c) case 3 adding band-limited random noise to the entire survey. In general, the ML model shows high probabilities for MTDs, salt, and conformal sediments with no dimming in the probabilities for correctly classified facies possibly indicating that facies are being classified with similar confidence by the algorithm in all cases. However, results obtained after applying Kuwahara filtering show less noise and less misclassifications inside and around salt diapirs compared to cases 1 and 3.
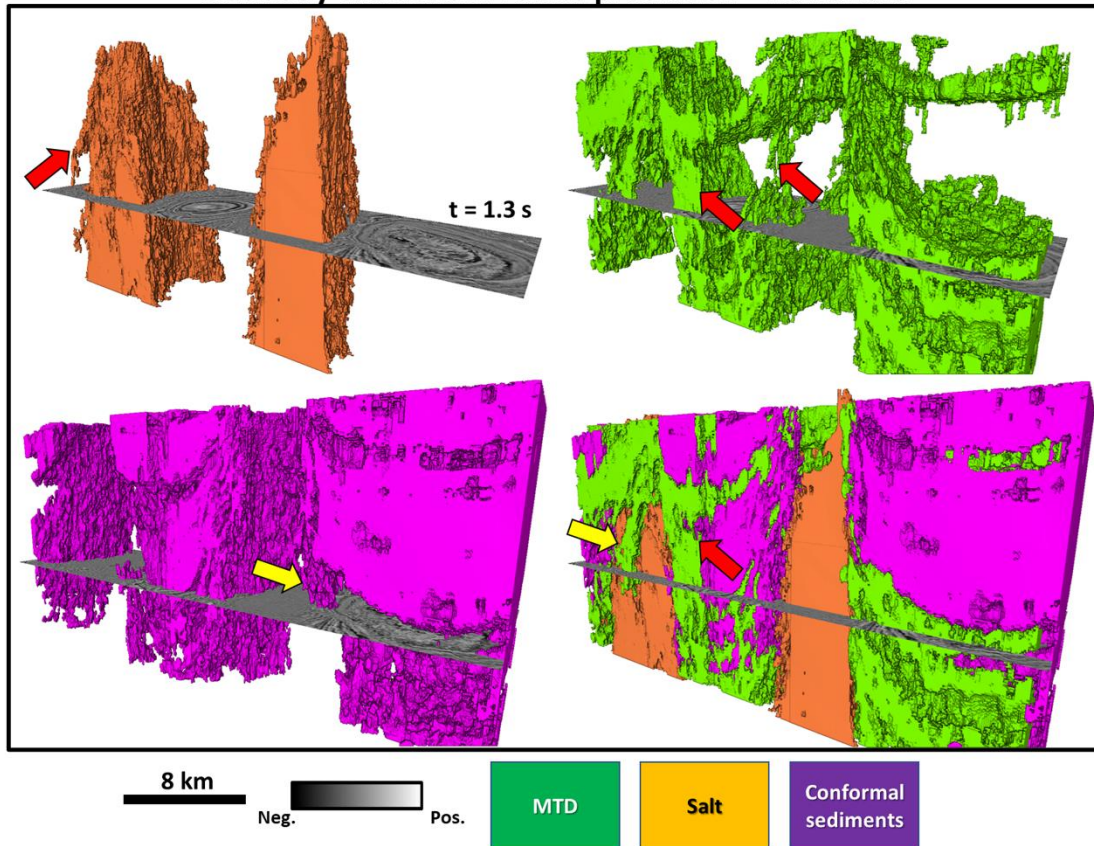
Figure 3.16. Geobody extraction of target seismic facies MTDs, salt, and conformal sediments using the seismic facies prediction associated with case 2 and probabilities higher than 70% for each facies. I can isolate the target seismic facies accurately throughout the study area. Dipping conformal reflectors close to the edges of the salt are being misclassified as salt or MTDs facies (the red arrows), whereas gaps inside the salt diapirs can be misclassified as MTD or conformal sediments (the yellow arrows).
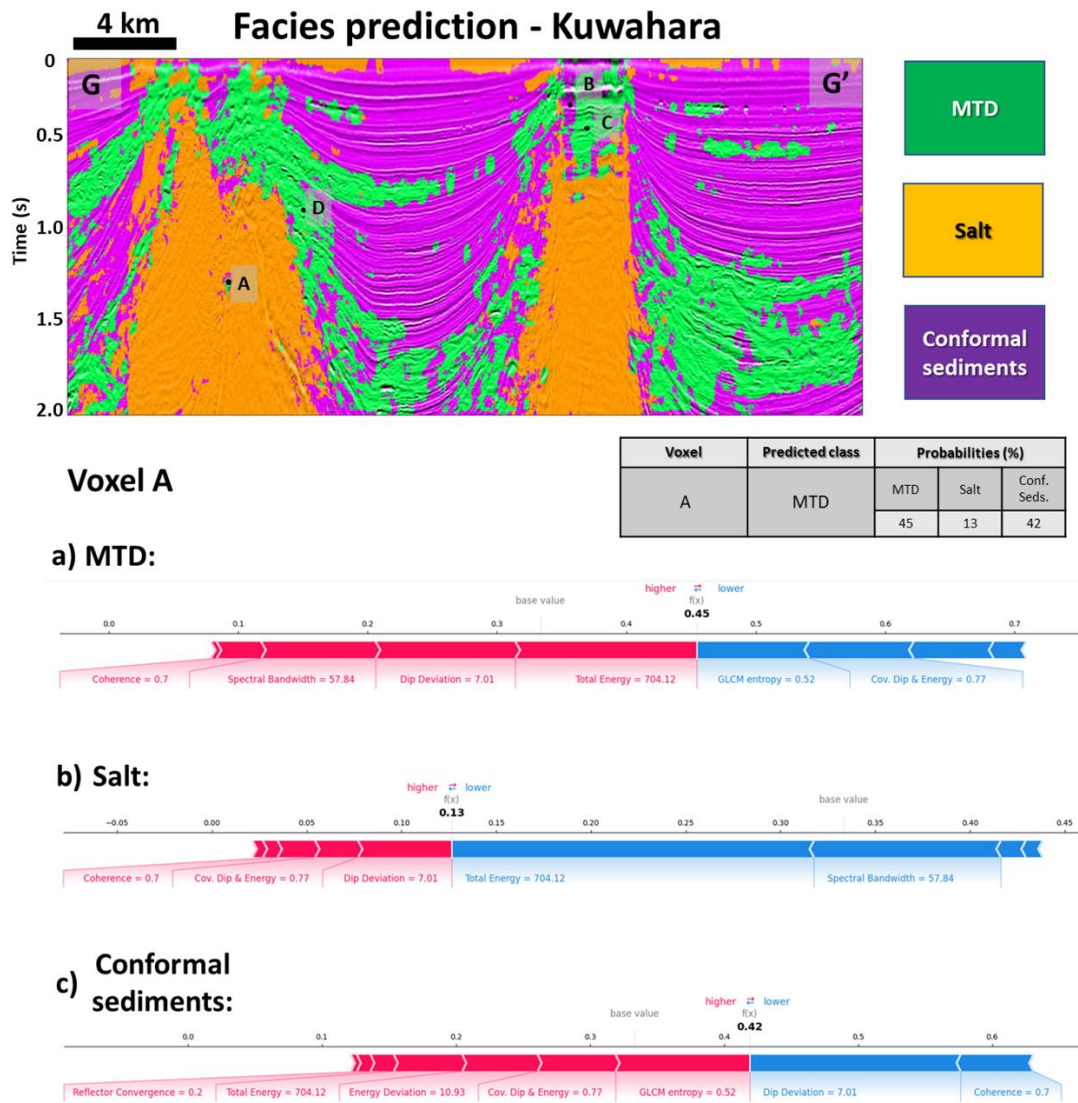
Figure 3.17. The SHAP force plot for voxel of interest A along vertical section GG'. Voxel A is located inside a salt diapir and was misclassified as MTD by the algorithm with a 45% probability. (a) For MTD, the voxel starts with a base value of 33%. Considering the effect of the candidate seismic attributes in the model, I note that the total energy, dip deviation, spectral bandwidth, and coherence increase the probability of having MTD, whereas GLCM entropy and covariance of dip and energy gradient push down the probability to the final 45%. (b) For salt, the coherence, dip deviation, and covariance of dip and energy gradient attributes increase the probability, whereas the total energy and spectral bandwidth are pushing the probability down from the base value of 33% to the final 13%. (c) For conformal sediments, the GLCM entropy, covariance of dip and energy gradient, energy deviation, total energy, and reflector convergence push the probability up, whereas the dip deviation and coherence attributes decrease the probability to 42%. Please note that the attribute values are shown without scaling for interpretational purposes.
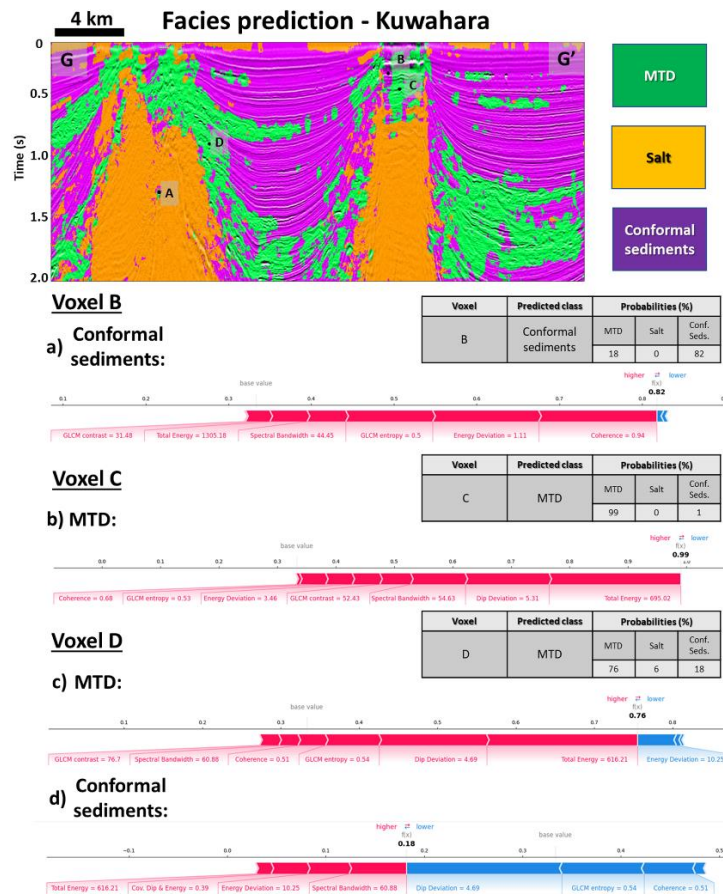
Figure 3.18. The SHAP force plot along line GG'. (a-b) Voxel B and C are associated with high-amplitude seismic multiples, but they were misclassified by the algorithm as conformal sediments and MTD with 82 and 99% probabilities, respectively. For voxel B, GLCM contrast, total energy, spectral bandwidth, GLCM entropy, energy deviation, and coherence increase the probability from the base value of 33% to 83%, whereas the remaining attributes show a composite impact of 0.1% that decrease the probability to the final 82%. Voxel C starts a base value of 33%. Then, the covariance of dip and energy gradient (not shown automatically in the SHAP force plot due to its small impact in the classification), coherence, GLCM entropy, energy deviation, GLCM contrast, spectral bandwidth, dip deviation, and total energy push the probability up to 99.1%, whereas the reflector convergence attribute (also not shown automatically in the SHAP force plot due to its small impact) decreases the probability to its final 99%. (c) Voxel D associated with dipping conformal sediments close to the edges of the salt was misclassified as MTD. For the MTD seismic facies, GLCM contrast, spectral bandwidth, coherence, GLCM entropy, dip deviation, and total energy pushing the probability up, whereas energy deviation pushes down the probability to its final 76%. (d) For the conformal sediments facies, total energy, covariance of dip and energy gradient, energy deviation, and spectral bandwidth push the probability up, whereas dip deviation, GLCM entropy, and coherence decrease the probability to its final 18%.
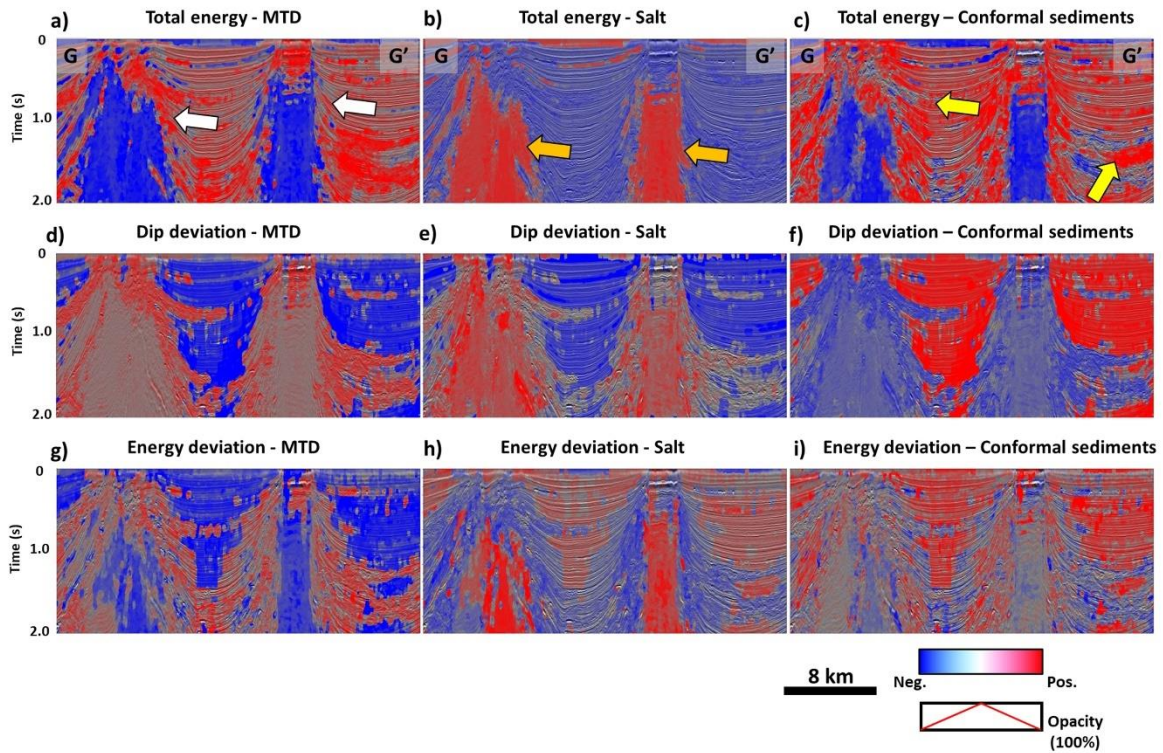
Figure 3.19. The SHAP values corendered with the seismic amplitudes along line GG' for the total energy, dip deviation, and energy deviation attributes for MTDs, salt, and conformal sediments. Note that positive SHAP values increase the probability and are characterized by the red colors, whereas negative SHAP values are associated with the blue colors and decrease the probability. (a-c) Total energy attribute. In general, the ML model correctly distinguishes between the target seismic facies. However, high-amplitude conformal sediments and reflectors with lower amplitude, lower seismic quality around the diapirs increase the probability of having MTDs (the white arrows). Some dipping reflectors and noisy areas close to the diapirs increase the probability of a voxel being classified as salt (the orange arrows), whereas overlap between conformal sediments and MTD is visible (the yellow arrows). (d-f) Dip deviation attribute. Overlap between MTD and salt is visible. In addition, MTDs still show overlap with the reflectors surrounding the diapirs (g-i) Energy deviation attribute. Salt diapirs show a strong overlap with the flat, high-amplitude conformal sediments located inside the mini-basins. Finally, using the dip and energy deviation attributes, dipping reflectors decrease the probability of having conformal sediments.

Figure 3.20. The SHAP values corendered with the seismic amplitudes along line GG' for the (a-c) coherence, (d-f) covariance of dip and energy gradient, and (g-i) GLCM contrast attributes for MTDs, salt, and conformal sediments. For the MTD seismic facies, overlap with the lower amplitude dipping reflectors surrounding the salt is still visible. In addition, the salt diapirs and MTD show overlap when considering the covariance of dip and energy attribute. For the salt seismic facies, salt diapirs tend to be isolated correctly by the model. However, overlap between the diapirs and the MTDs and dipping conformal reflectors exists when considering the coherence attribute, but using the GLCM contrast attribute, the overlap with the MTDs tends to decrease. Finally, for the conformal sediments, some overlap with the salt seismic facies is visible when considering the GLCM contrast attribute. In addition, the flat high-amplitude reflectors are not making an impact in the classification when considering the covariance of dip and energy gradient.

130
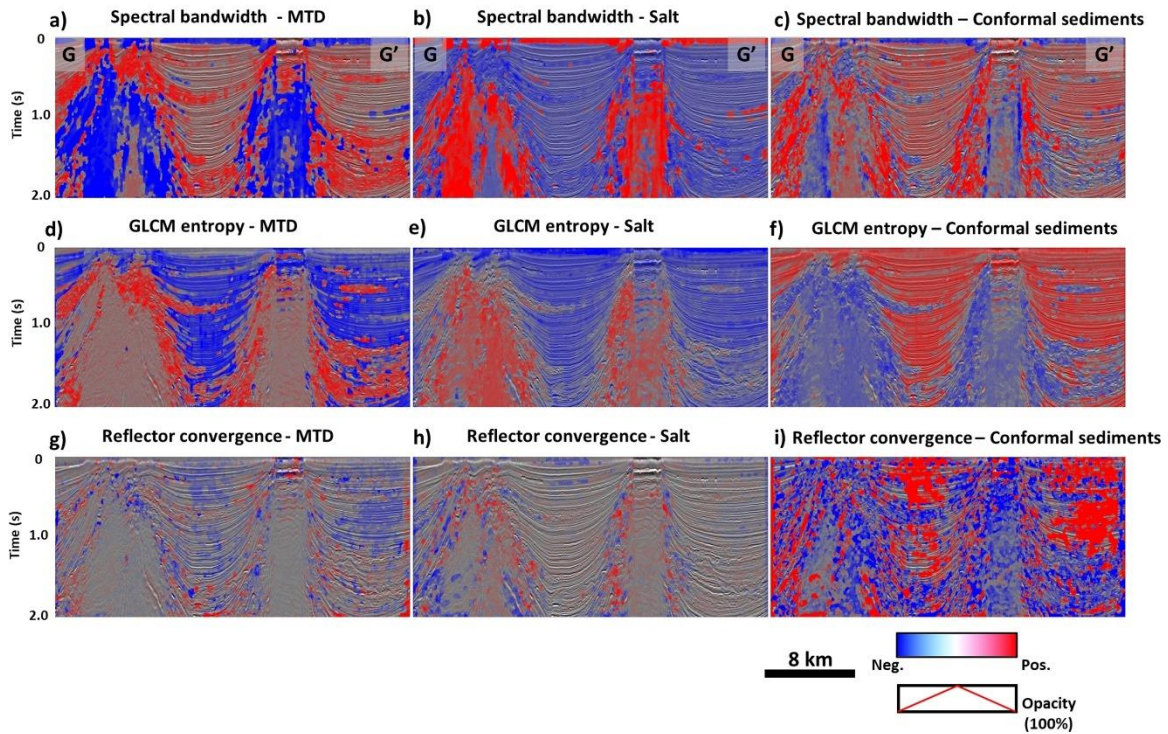
Figure 3.21. The SHAP values corendered with the seismic amplitudes along line GG' for the (a-c) spectral bandwidth, (d-f) GLCM entropy, and (g-i) reflector convergence attributes for MTDs, salt, and conformal sediments. Note that the reflector convergence attribute does not have a large impact in the classification and does not have clear trends to differentiate between the target seismic facies. Overlap between MTDs and the conformal sediments is visible for the spectral bandwidth attribute, whereas the GLCM entropy attribute shows some overlap between the salt diapirs and MTDs. For the salt seismic facies, noisy areas close to the edges of the survey and dipping reflectors increase the probability of voxels being classified as salt. Finally, for conformal sediments, slight overlap with MTDs and salt is seen when using the spectral bandwidth attribute. Considering the GLCM entropy attribute, dipping conformal reflectors characterized by lower amplitudes decrease the probability of having conformal sediments.

131
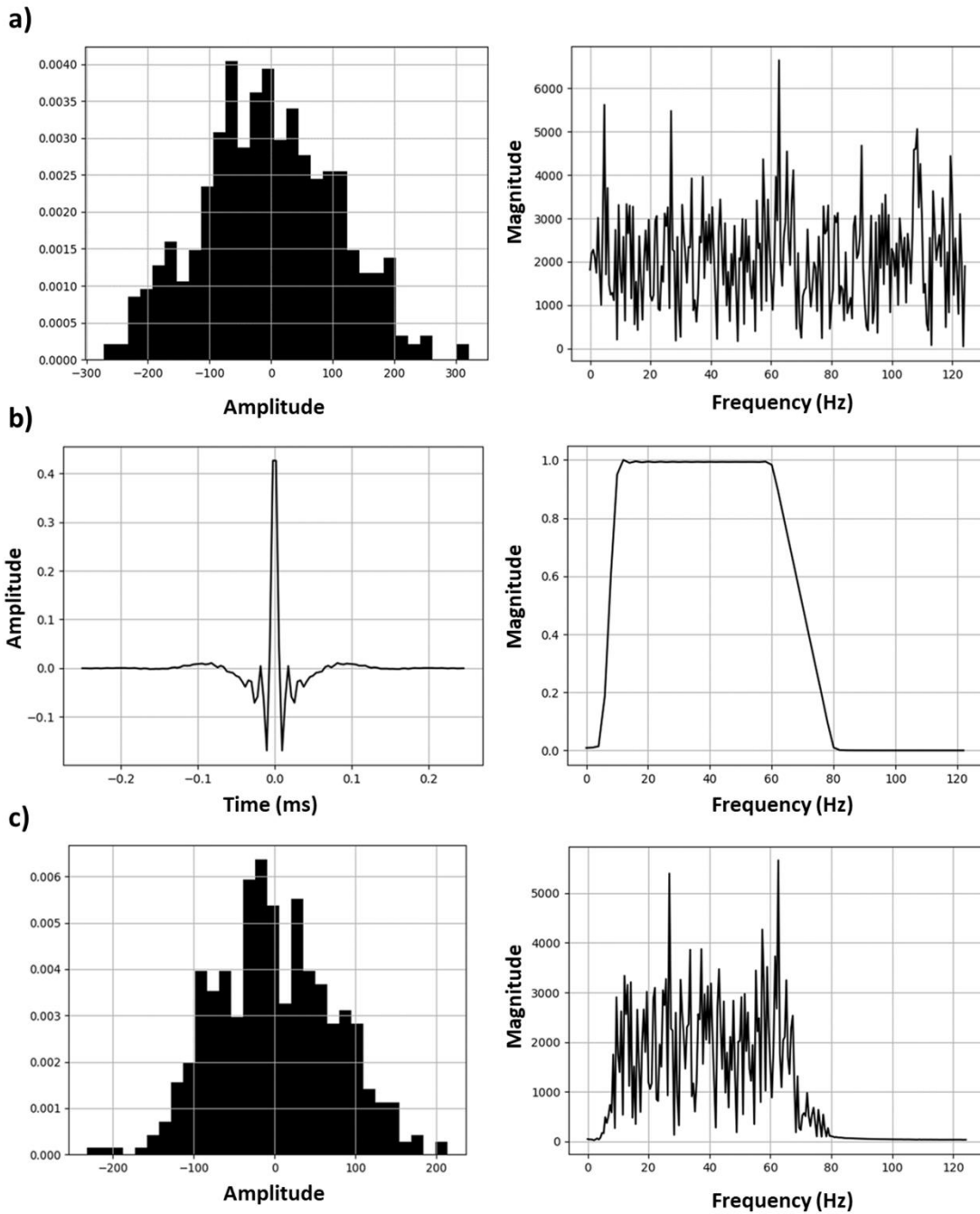
Figure 3.A-1. Adding band-limited noise to the seismic volume. (a) The estimated AWGN $N(\mu,\sigma)$ shows a flat spectrum, and it is characterized by frequencies larger than 80 Hz. (b) Ormsby filter $O(t)$ applied to $N(\mu,\sigma)$ with corner frequencies $f_1 = 5$ Hz, $f_2 = 10$ Hz, $f_3 = 60$ Hz and $f_4 = 80$ Hz, duration of T=500 ms, and sampling interval $\Delta t = 4$ ms. (c) Band-limited noise $\widehat{N}$ and target S/N = 2. Note that the estimated AWGN does not show amplitudes for frequencies larger than 80 Hz.
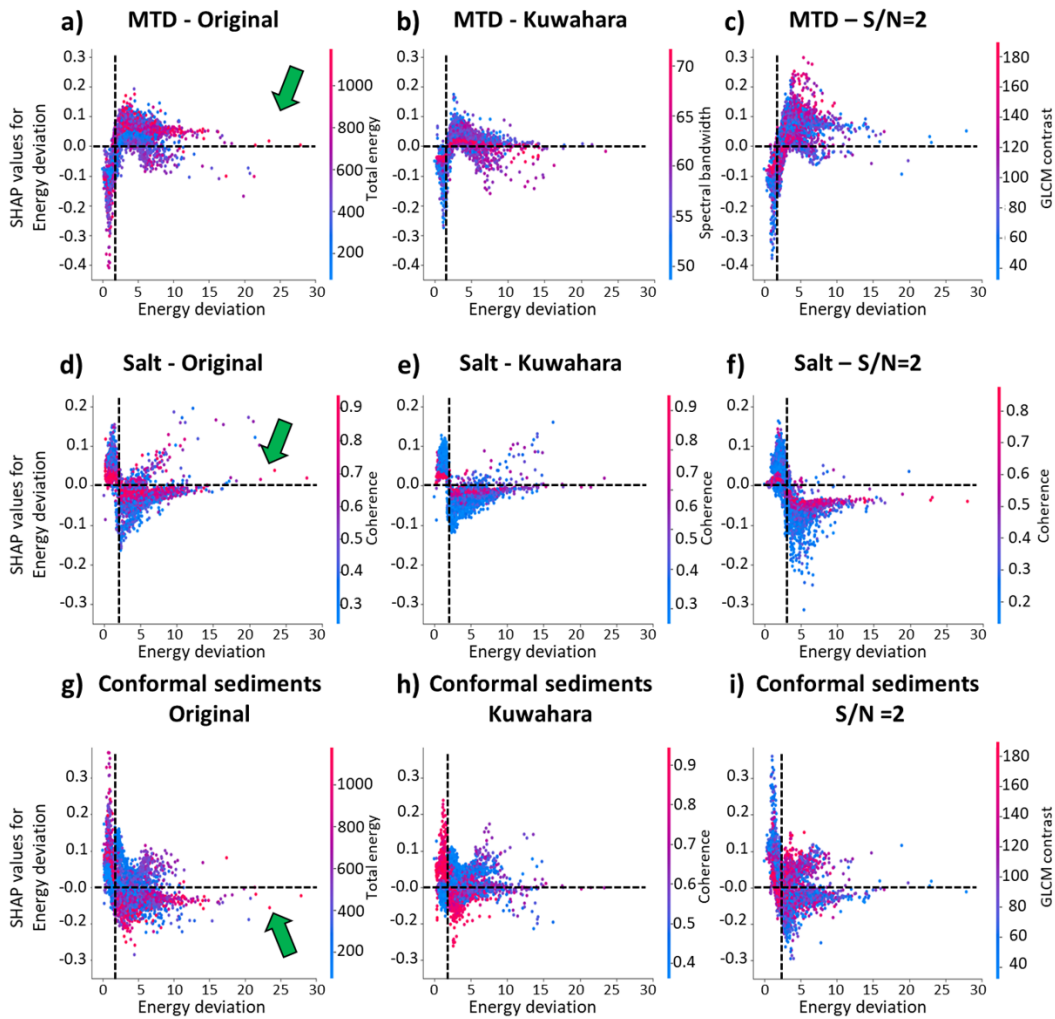
Figure 3.S1. The SHAP dependence plot for energy deviation. (a-c) For MTD, two trends are still increasing the probability of having MTDs: (1) values of energy deviation larger than approximately 2.5 with lower values of total energy, higher values of spectral bandwidth, and low to high values of GLCM contrast and (2) voxels showing energy deviation larger than 2.5 with higher values of total energy, lower values of spectral bandwidth, and low to high values of GLCM contrast. (d-e) For the salt seismic facies, values of energy deviation smaller than 2.5 for cases 1 and 2 and smaller than approximately 4 when adding band-limited noise, and low values of coherence are pushing towards salt. However, some values characterized by low energy deviation, high coherence and some voxels showing energy deviation larger than 2.5 are also increasing the probability of a voxel being classified as salt. (g-i) Finally, for conformal sediments, two well-defined trends are still visible: (1) values of energy deviation smaller than approximately 2.5 and high values of total energy, coherence, and GLCM contrast and (2) values of energy deviation larger than 2.5 with low values of total energy, coherence, and GLCM contrast.

SHAP dependence plots: Coherence
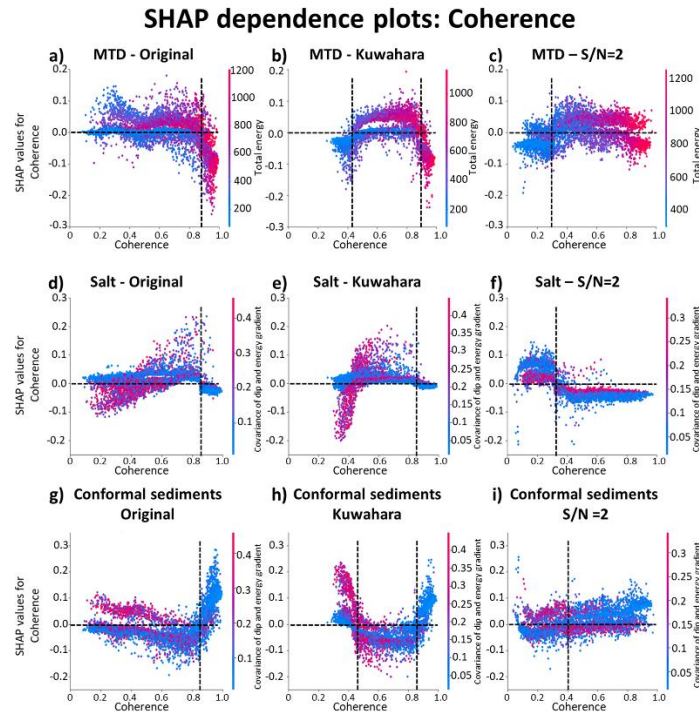
Figure 3.S2. The SHAP dependence plot for coherence. (a-c) In the MTD seismic facies, values of coherence smaller than approximately 0.9 and high values of total energy are pushing towards MTD seismic facies, whereas values of coherence smaller than 0.9 and low total energy increase the probability of having MTD, but the latter offers less impact in the classification with SHAP values closer to zero. In contrast, for cases 2 and 3, I note that values of coherence between 0.35-0.45 to approximately 0.9 and low to high values of total energy are pushing towards MTD, whereas now values of coherence lower than approximately 0.35-0.45 are, in general, decreasing the probability. (d-f) For salt, the distribution of SHAP values is changing for cases 2 and 3. For cases 1 and 2, voxels showing values of coherence lower than approximately 0.85 and low to high values of covariance of dip and energy gradient are increasing the probability of having salt. For case 3 a better-defined trend for the salt seismic facies is visible with values of coherence smaller than 0.3 and low to high values of covariance of dip and energy gradient increasing the probability. (g-i) For conformal sediments, two trends for this seismic facies are still seen. For case 1, values of coherence smaller than 0.85 with higher values of covariance of dip and energy gradient and values of coherence larger than 0.85 with low values of covariance of dip and energy gradient are increasing the probability of a voxel being classified as conformal reflectors. When applying Kuwahara filtering, values of coherence smaller than 0.45 with low to high values of covariance of dip and energy gradient, and values of coherence larger than 0.85 with low values of covariance of dip and energy gradient are pushing towards the conformal sediments. Finally, when the input data are contaminated with band-limited noise, the first trend is characterized by values of coherence smaller than 0.4 and high values of covariance of dip and energy gradient, whereas the second trend is associated with values of coherence larger than 0.4 and lower covariance of dip and energy gradient.
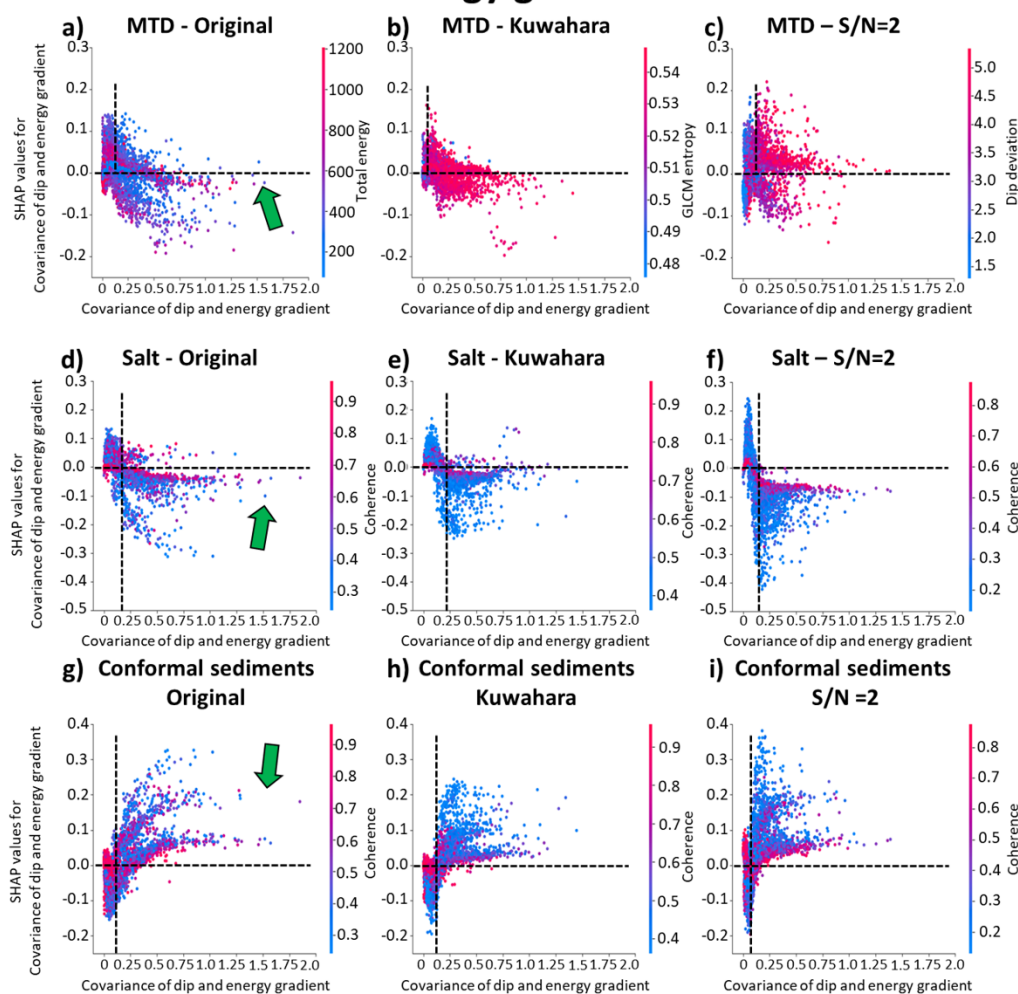
Figure 3.S3. The SHAP dependence plot for covariance of dip and energy gradient. (a-c) For the MTD seismic facies, two trends are still visible: (1) voxels characterized by covariance of dip and energy gradient lower than approximately 0.15 with higher total energy and GLCM entropy, and lower dip deviation and (2) voxels associated with covariance of dip and energy gradient larger than 0.15 with lower total energy, and higher GLCM entropy and dip deviation are increasing the probability of having MTDs. (d-f) For the salt seismic facies, values of and covariance of dip and energy gradient smaller than 0.15-0.2 with lower values of coherence are pushing towards salt. However, some values larger than 0.15-0.2 also increase the probability for this seismic facies. (g-i) Finally, for the conformal sediments, two well-defined tends increasing the probability of a voxel being classified as conformal reflectors are seen: (1) values of covariance of dip and energy gradient smaller than 0.1-0.2 and higher values of coherence and (2) values of covariance of dip and energy gradient larger than 0.1-0.2 with lower values of coherence.

Figure 3.S4. The SHAP dependence plot for GLCM contrast. (a-c) For MTD, two trends are still visible, but there is some vertical overlap between them for cases 1 and 2. For these cases, values of GLCM contrast lower than approximately 90 and low to high values of covariance of dip and energy gradient and total energy are pushing towards MTDs. In contrast, for case 3, there is more vertical separation between the trends in which values of GLCM contrast smaller than 140 and low to high values of dip deviation are increasing the probability. (d-f) In cases 1 and 2 for the salt seismic facies, values of GLCM contrast larger than approximately 75-80 and low to high values of covariance of dip and energy gradient are increasing the probability of having salt. Moreover, when adding band-limited AWGN, a better definition of the trend for this seismic facies is seen in which values of GLCM contrast larger than approximately 140 with lower total energy are increasing the probability. (g-i) For the conformal sediments facies, two trends that are pushing towards this facies are still seen. For cases 1 and 2, the first trend is characterized by values of GLCM contrast lower than approximately 75-80 and lower values of energy deviation and covariance of dip and energy gradient, whereas the second trend show values of GLCM contrast larger than 75-80 and higher values of energy deviation and covariance of dip and energy gradient. For case 3, a similar trend than case 2 is seen, but now the threshold for the GLCM contrast is increasing to approximately 110.

SHAP dependence plots: Spectral bandwidth
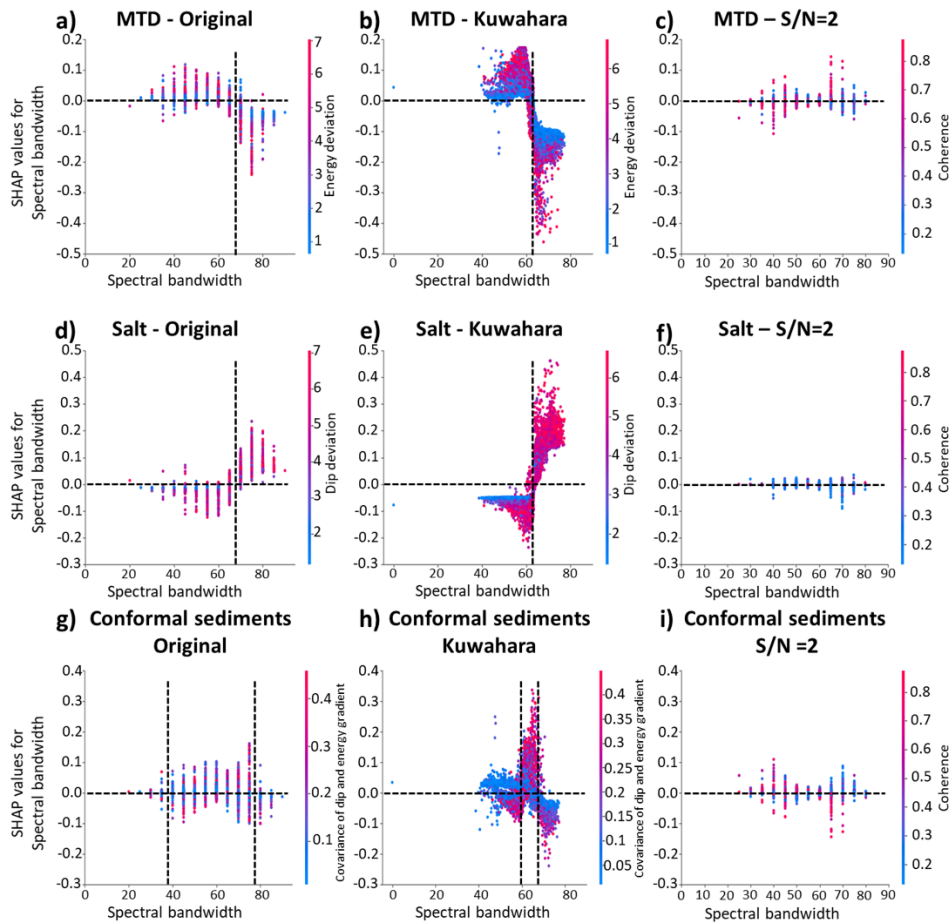
Figure 3.S5. The SHAP dependence plot for spectral bandwidth. When applying Kuwahara filtering the spectral information is compressed and clustered for all facies. (a-c) For MTD, frequencies lower than 70 Hz with low to high values of energy deviation are increasing the probability in case 1, while applying Kawahara filtering, frequencies lower than 65 Hz and low to high values of energy deviation are increasing the probability of having MTDs. (d-f) For the salt seismic facies, frequencies larger than 70 Hz and high dip deviation tend to push towards this seismic facies. Moreover, for case 2, frequencies larger than 65 Hz and high values of dip deviation increase the probability of having salt. (g-i) Finally, for conformal sediments, an overlap with the MTD facies is visible with frequencies between 40 and 65 Hz and low to high values of covariance of dip and energy gradient increasing the probability of having a voxel classified as conformal sediments. For case 2, two well-defined trends push towards the conformal sediments facies: (1) frequencies between 60 to 70 Hz with high values of covariance of dip and energy gradient and (2) frequencies lower than 60 Hz and low values of covariance of dip and energy gradient. Note that in the presence of strong noise, all trends and impact are lost when using the spectral bandwidth attribute with frequencies pushing towards SHAP values close to zero.

SHAP dependence plots: GLCM entropy
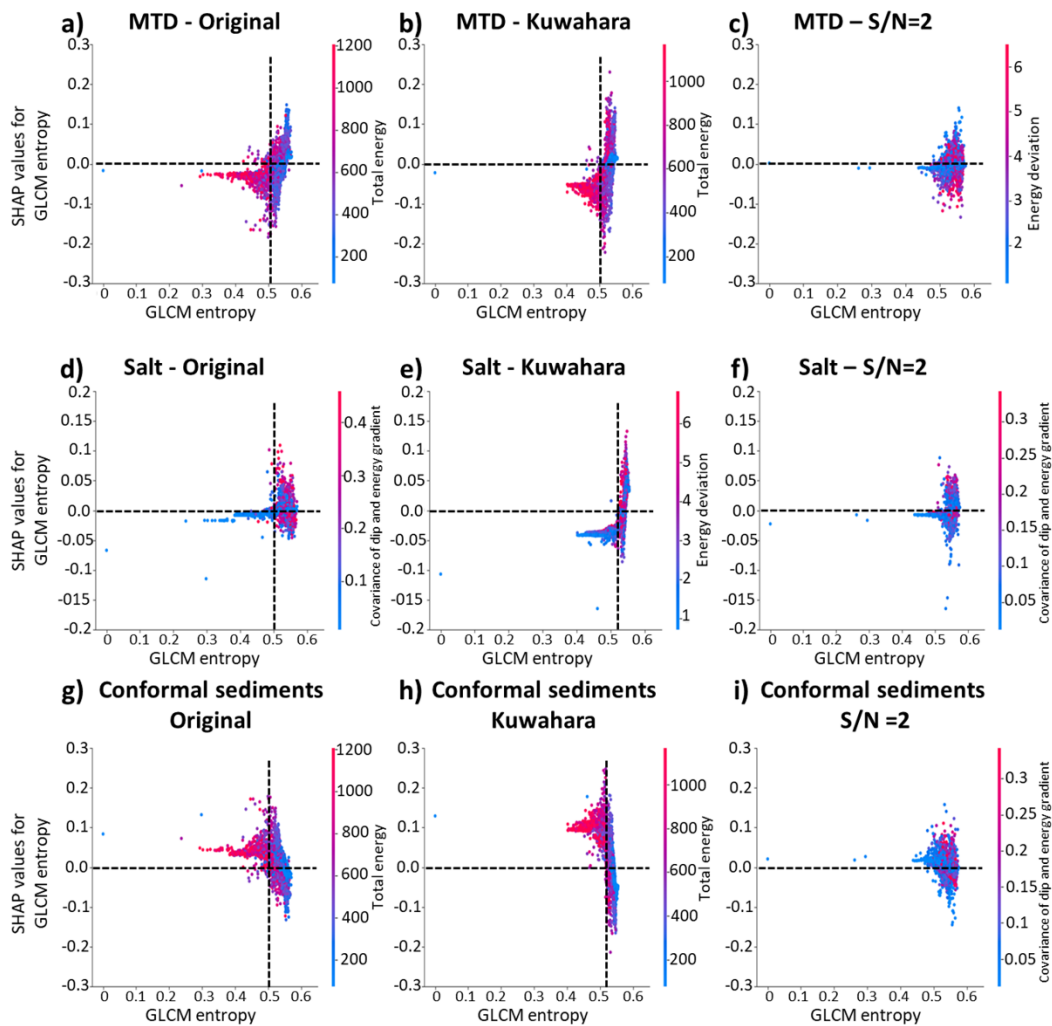
Figure 3.S6. The SHAP dependence plot for GLCM entropy. Trends are not that well-defined compared to other attributes and MTDs and conformal sediments show overlap between them (a-c) For the MTD seismic facies, values of GLCM entropy larger than 0.5 with high values of total energy increase the probability (d-f) For salt, values of GLCM entropy larger than 0.5 with low to high values of covariance of dip and energy deviation are increasing the probability for cases 1 and 2 (g-i) Finally, for conformal sediments, values of GLCM entropy smaller than 0.5 with high values of total energy are increasing the probability. Note that some voxels characterized by GLCM entropy larger than 0.5 and lower total energy can also increase the probability of having MTD or conformal sediments. Moreover, applying Kuwahara filtering, trends for these seismic facies remain very similar to considering case 1, but the data look more compressed and clustered, making the trends better defined. Finally, similar to the spectral bandwidth attribute, trends using the GLCM entropy are lost in the presence of strong noise.

SHAP dependence plots: Reflector convergence

Figure 3.S7. SHAP dependence plot for reflector convergence. Using the original data, there is a strong overlap between facies and analyzing possible trends for this attribute is a challenging task. However, applying Kuwahara filtering or adding band-limited AWGN, these trends become slightly better defined for all seismic facies. However, some overlap between seismic facies still exists. (a-c) For MTD seismic facies, values of reflector convergence larger than approximately 0.25-0.3 with high values of covariance of dip and energy gradient have higher impact in the classification and increase the probability. However, some values characterized by reflector convergence lower than 0.25-0.3 and lower values of covariance of dip and energy gradient also increase the probability for this facies. (d-f) For salt, voxels characterized by reflector convergence lower than 0.3 and low values of coherence and high values of dip deviation increase the probability. (g-i) For the conformal sediments facies, two trends increasing the probability are seen: (1) values of reflector convergence larger than approximately 0.2 with low values of coherence and total energy, and (2) values of reflector convergence smaller than 0.2 and higher values of coherence and total energy.

Chapter 3 Tables

	Case 1	Case 2	Case 3
Mean accuracy (%)	83.6	91.46	81.72

Table 3.1. Validation accuracy for cases 1, 2, and 3 using the data extracted from polygons manually picked along line FF'. The highest validation accuracy of 91.45% is obtained after applying Kuwahara filtering to the seismic attributes (case 2). The original seismic attributes (case 1) and adding random noise with S/N = 2 (case 3) offer validation accuracies of 83.6% and 81.72%, respectively. Note that the same hyperparameters for the random forest architecture are used for all cases.

Attribute	MTD trend 1	MTD trend 2	Salt	Conformal sediments trend 1	Conformal sediments trend 2
Total energy	> 400	> 400	< 400	< 400-500	> 400-500
Dip deviation	> 2	> 2	> 2.5	2.5-4	< 2.5
Energy deviation	> 2.5	> 2.5	< 2.5 < 4.0 (S/N=2)	> 2.5	< 2.5
Coherence	<0.9 0.4 – 0.9 (Kuwahara) 0.35-0.9 (S/N=2)	<0.9 0.4 – 0.9 (Kuwahara) 0.35-0.8 (S/N=2)	< 0.85 (original and Kuwahara) < 0.3 (SNR=2)	< 0.85 <0.45 (Kuwahara) <0.4 (S/N=2)	> 0.85 > 0.85 (Kuwahara) > 0.4 (S/N=2)
Covariance of dip and energy gradient	< 0.15	> 0.15	< 0.15-0.2	> 0.1-0.2	< 0.1-0.2
GLCM contrast	< 90 <140 (S/N=2)	< 90 <140 (S/N=2)	> 75-80 > 140 (S/N=2)	> 75-80 > 100-110 (S/N=2)	< 75-80 < 100-110 (S/N=2)
Spectral bandwidth	<60-65 Hz.	<60-65 Hz.	> 65-70 Hz.	60-70 Hz	< 60-65 Hz.
GLCM entropy	> 0.5	> 0.5	> 0.5	> 0.5	< 0.5
Reflector convergence	< 0.25-0.3	> 0.25-0.3	< 0.3	> 0.2	< 0.2

Table 3.2. Multiattribute space rules learned by the ML model to distinguish among MTDs, salt, and conformal sediments obtained after analyzing all 81 SHAP dependence plots for all cases and seismic attributes. For conformal sediments, I observe two well-defined trends. The first trend is characterized by lower values of total energy and coherence, and larger values of dip deviation, energy deviation, covariance of dip and energy gradient, GLCM contrast, spectral bandwidth, GLCM entropy and reflector convergence, whereas the second trend shows a completely different response characterized by large values of total energy and coherence, and lower values of dip deviation, energy deviation, covariance of dip and energy gradient, GLCM contrast, spectral bandwidth, GLCM entropy, and reflector convergence, which are possibly associated with dipping conformal reflectors located close to the edges of the salt, and flat, higher amplitude conformal sediments located between salt diapirs, respectively. For MTD, one well-defined trend associated with higher values of total energy, dip deviation, energy deviation, GLCM entropy, and lower values of coherence, covariance of dip and energy gradient, and GLCM contrast is visible. The second trend also increasing the probability of having MTDs might be associated with overlap between this seismic facies and dipping and/or parallel conformal sediments and salt.

Chapter 4: Identification of bottom-simulating reflectors (BSRs) using seismic attributes and machine learning

Abstract

The impact of naturally abundant gas hydrates on climate is not completely understood. Moreover, mapping the lateral distribution and thickness of gas hydrates and associated free gas using even the best quality seismic surveys can be quite difficult. Because the stability of gas hydrates within the Gas Hydrate Stability Zone (GHSZ) is controlled by temperature and pressure, and because their impedance can be significantly different than those of the sedimentary matrix in which they occur, I often am able to identify a bottom simulating reflector (BSR) at the base of the GHSZ that cuts across the stratigraphic reflectors. For the same reason, when the stratigraphic reflectors are parallel to the ocean bottom, the BSR is easily confounded with a strong stratigraphic reflector. Seismic attributes and machine learning (ML) applied to seismic facies analysis have been successful in quantitatively mapping patterns associated with karst collapse, mass transport complexes, and volcanic intrusions that are tedious for human interpreters to pick. These techniques enhance geologic features of interest and discover hidden relationships in the data, respectively. However, selecting an optimal combination of seismic attributes and training data to perform a robust seismic facies classification is highly dependent on the interpreter's skills. In this study, I apply principal component analysis (PCA) to select a suite of geometric and spectral attributes to be used as input for self-organizing maps (SOM) to identify BSRs and surrounding facies in a seismic volume located in the Blake Ridge, offshore South Carolina, USA. PCA decomposes a multiattribute input into a suite of linear uncorrelated

142

components sorted by their variability. However, variability tends to have little relationship with geology. Therefore, I evaluate PCA as an attribute selection technique under three different training data selection strategies: 1) using unbiased training data extracted throughout a 3D grid spanning the entire data volume, 2) using biased training data that fall in BSR polygons defined by the interpreter, and 3) using biased training data that are extracted from polygons defined by the interpreter enclosing four main seismic patterns associated with the BSR; high-amplitude, high frequency continuous reflectors; low-amplitude, sigmoid to chaotic reflectors; and high-amplitude discontinuous reflectors. I found that combining geometric and spectral attributes such as total energy, coherence, GLCM entropy, and peak magnitude as input for SOM represents an effective method to detect BSRs. Moreover, significant overlap with clusters associated the BSRs and surrounding seismic facies might exist in the study area. However, using a smaller subset of samples representing the target four seismic facies when applying PCA to select input attributes for SOM offers optimal BSRs identification, whereas overlap between the BSRs and surrounding facies is reduced.

Introduction

Gas hydrates, which are mainly composed of methane and water, are abundant in nature and commonly occur in shallow subsurface oceanic settings in continental margins and permafrost, where low temperature and high-pressure settings contribute to their formation. However, the impact of gas hydrates in climate change is not completely understood. Geological mechanisms such as changes in sea level and sea floor erosion can produce variations in temperature and pressure potentially releasing methane to the ocean

and atmosphere (Lee et al., 1994; Kennett et al., 2000; Holbrook, 2002; Dickens, 2003; Davies et al., 2021).

Although gas hydrates are naturally abundant, there is not a general technique for its detection in the subsurface. One way to identify the presence of gas hydrates consists of analyzing changes in seismic amplitude data to map bottom-simulating reflectors (BSRs). BSRs are usually characterized by high amplitude, phase-shifted reflectors parallel to the sea floor that delineate the base of the Gas Hydrate Stability Zone (GHSZ), which represents a region where pressure and temperature conditions are favorable for gas hydrate development (Lee et al., 1994; Shipboard Scientific Party, 1996; Hornback et al., 2003, 2008). However, neither all gas hydrates might produce BSRs at the base of the GHSZ neither all BSRs guarantee the presence of hydrates in the area (Kuramoto et al., 1992; Wood and Ruppel, 2000; He et al., 2006).

Shipley et al. (1979) identify BSRs on seismic data over continental slopes across North, Central, and South America, Yoo et al. (2013) integrate well and seismic data to map gas hydrates in the Ulleung Basin, East Sea. Plaza-Faverola et al. (2012) combined stratigraphic and structural analysis using pre-stack depth migrated seismic data to study gas hydrate concentrations and fluid flow in the southern Hikurangi margin, New Zealand.

Seismic attributes are common tools in the exploration and development of hydrocarbon resources and are used to perform a more complete reservoir characterization by quantitively enhancing and differentiating the geologic features and reservoir properties in a depositional environment (Posamentier and Kolla, 2003; Chopra and Marfurt, 2007). Using full waveform inversion to compute a P-wave velocity model which is coupled with

the coherence attribute to be used as proxies for primary saturation and secondary porosity respectively, Jaiswal (2016) estimates the total hydrate saturation in the Krishna-Godavari Basin, offshore India. Bedle (2019) uses rock physics modelling to estimate the amplitude variation with angle (AVA) responses to better delineate strong and weak BSRs, whereas Clairmont et al. (2021) use a sparse-spike decomposition algorithm to compute the quality factor as a means to study attenuation effects in seismic data to differentiate hydrates from free gas in the Pegasus Basin, New Zealand.

Machine learning (ML) techniques have become widely popular for pattern recognition in the past two decades. For seismic facies identification, seismic attributes are common inputs to ML algorithms. Roy et al. (2014) compute a suite of seismic inversion volumes and apply generative topographic mapping to identify different rock types in a carbonate wash in the Veracruz Basin, southern Mexico. Chopra and Marfurt (2019) apply a suite unsupervised machine learning techniques to a multi-attribute seismic input to study the facies distribution in a channel system in a seismic volume from the Barents Sea. Recently, Lubo-Robles et al. (2022) train a random forest algorithm and apply Shapley additive explanations to quantify the sensitivity of a given facies to changes in the seismic attributes and understand how these variations affect the ML algorithm predictions to differentiate salt, mass transport deposits, and conformal siliciclastic sediments in a Gulf of Mexico seismic volume.

In general, ML can be broken into supervised and unsupervised algorithms. A limitation of supervised algorithms is that if I lack adequate supervision data (or in my case, an understanding of the expression of gas hydrates) I run the risk of miscategorizing seismic

145

features not included in the training data. A limitation of unsupervised learning is that while the algorithm attempts to represent all the features in the data, it does so (typically) using a least-squares algorithm, such that features that represent less than 1% of the voxels in a 3D survey may be not be represented at all (Roden and Chen, 2017).

To identify strong and weak BSRs in the Pegasus Basin, New Zealand, Chenin (2020) performs an unsupervised facies analysis using instantaneous and AVA attributes as input to self-organizing maps (SOM). However, to the best of my knowledge, there are no published studies in which modern geometric seismic attributes are combined with spectral attributes to perform an unsupervised classification and map BSRs.

Moreover, selection of training data and optimal combination of seismic attributes to perform a robust seismic facies classification is a challenging task. In recent years, an increasing number of studies have been conducted to address this situation (Wang et al., 2015; Amin et al., 2017; Kim et al., 2019; Qi et al., 2020; Lubo-Robles et al., 2021). Zhao and Marfurt (2017) analyze a suite of training data configurations for SOM to interpret the main geologic features present in a turbidite channel system in the Canterbury Basin, New Zealand. Roden et al. (2015) apply principal component analysis (PCA) to all data samples in a multi-dimensional input to generate a suite of principal components - sorted by their variability - as a means to analyze the ability of individual seismic attributes to differentiate features in the seismic data volume.

Unfortunately, higher variability in PCA may have little relationship to geology (Guo et al., 2009; Roden et al., 2015). Lubo-Robles and Marfurt (2019) found that small-scale geologic features associated with lower reflectivity tend to be more difficult to interpret in

the first principal components than in subsequent components representing the remaining variability of the data.

Although PCA and SOM are unsupervised classification algorithms, the selection of training data biases the result. If I use training data that statistically represents the entire seismic survey, it may underrepresent smaller, localized features of interest. I therefore hypothesize that training data that are biased towards the target BSR feature, or alternatively, equally represent the BSR to the background or a small suite of other geologic features will provide a superior classification result.

I begin this study by describing the geological setting of the Blake Ridge, followed by the mechanics of PCA for attribute selection. Then, I compute a suite of candidate geometric and spectral attributes and apply PCA considering my three alternative training data selection strategies. I evaluate the classification using both PCA and SOM. I provide mathematical details on how to implement PCA for seismic attribute selection in the Appendix.

Geologic background

Gas hydrates are ice-like solids mainly composed of methane and water which can form within the Gas Hydrate Stability Zone (GHSZ), which is characterized by low temperature and high-pressure conditions and are common in permafrost and continental margins within sediments located at approximately several hundred meters beneath the sea floor (Lee et al., 1994; Shipboard Scientific Party, 1996; Collet and Ladd, 2000; Hornback et al., 2003, 2008). Because the pressure and temperature gradients are almost orthogonal to

147

the sea floor, hydrates form parallel to the sea floor where the abrupt change in impedance result on seismic data in a bottom-simulating reflector (BSR). However, if variations in seismic impedance are not strong enough, BSRs might not be observed in seismic data even if gas hydrates are present (Wood and Ruppel, 2000; He et al., 2006).

The BSR is usually characterized by a high amplitude reflector that tends to follow the shape of the sea floor, cross-cutting stratigraphic reflectors, and show phase reversal from the sea floor (Shipboard Scientific Party, 1996; Holbrook et al., 2002; Hornback et al., 2003, 2008). Moreover, when BSRs are generated due to the presence of gas hydrates, they delineate the base of the GHSZ. Above the BSRs, sediments contain hydrate and water in their pore space, whereas below the BSRs, sediments are filled with free gas because hydrates cannot remain stable due to changes in temperature and pressure (Shipley et al., 1979; Lee et al., 1994; Shipboard Scientific Party, 1996; Hornback et al., 2003, 2008).

The Blake Ridge is a large Tertiary to Quaternary contourite drift located off the coast of South Carolina, USA (Shipboard Scientific Party, 1996; Collet and Ladd, 2000; Hornback et al., 2003, 2008). Based on well data, the Blake Ridge is characterized by gas hydrates within the pore space of clay-rich hemipelagic sediments resulting in a relatively high amplitude, continuous BSR (Shipboard Scientific Party, 1996; Collet and Ladd, 2000; Hornback et al. 2003).

In addition, according to Holbrook et al. (2002), Hornback et al. (2003, 2008), the Blake Ridge is a sediment-wave field, and its morphology is controlled by ocean currents in the Western Boundary Undercurrent (WBUC). Sediments deposited towards the east are

eroded by the WBUC, whereas eroded sediments redeposited on the western side of the ridge.

Methods

Data set and seismic response of main geologic features

The 3D Blake Ridge seismic survey is located offshore South Carolina, USA and covers an area of approximately 350 km^2 (135 mi^2). The volume consists of 95 inlines and 1306 crosslines with bin size of 75 x 37.5 m, sampling interval of 2 ms, and record length from 3.4s to 5.998s. In this study, I pick the sea floor seismic reflection and create a phantom horizon ranging from approximately 4.5 to 5.5s to bracket the seismic reflections associated with the main geologic features of interest (the yellow rectangle) and discard lower signal-to-noise ratio (S/N) areas at increasing time that provide little interpretation value during the seismic attribute computation (Figure 4.1).

Figure 4.2a shows a representative vertical section along inline 41. I observe four well-defined seismic reflection patterns: (1) The BSR characterized by strong leading negative amplitude cross-cutting strata (the white arrows). Moreover, it is highly continuous towards the southwest and becomes more discontinuous towards the northeast possibly associated with gas migration due to erosion affecting the sediment waves (Holbrook et al., 2002; Hornback et al., 2008). Above the BSR, I observe (2) high-amplitude, high frequency continuous reflectors and (3) lower-amplitude, chaotic to sigmoid seismic reflections. In addition, some high-amplitude reflectors are visible (the yellow arrows). Finally, (4) I observe high-amplitude discontinuous reflectors underlying the BSRs (the orange arrows).

In Figure 4.2b, I show an idealized model of the gas hydrate environment in the Blake Ridge based on inline 41. The BSR tend to follow the shape of the sea floor, whereas the GHSZ encloses the region from the BSR up to the sea floor and it is associated with temperature and pressure conditions favorable for gas hydrate development. Finally, trapped free gas can be found below the BSRs.

Principal component analysis (PCA)

Seismic attributes can be correlated both through their mathematical implementation and through geology. Each additional candidate attribute adds another "dimension" to the problem. To reduce the dimensionality of my data volume I wish to remove those parts of the data that are highly correlated to the others. Principal component analysis (PCA) is a linear mathematical technique that constructs linear combinations of attributes that better represent the data. The first step is to compute and then remove the M-dimensional mean and normalize for differences in units and distribution of each attribute (Ha et al., 2021).

After these adjustments, the first eigenvector is a straight line in N-dimensional space that least-squares fits the cloud of data. The M-dimensional data vectors projected onto the first eigenvector is called the first principal component of the data. The corresponding first eigenvalue represents the energy of the first principal component. After subtracting the first principal component, the process is repeated, thereby decomposing the input into uncorrelated components sorted by their energy (Guo et al., 2009; Chopra and Marfurt, 2014; Roden et al., 2015; Zhao et al., 2015; Lubo-Robles and Marfurt, 2019).

By construction, the principal components are ordered by the amount of energy represented (the eigenvalue). For this reason, the values represented by the first two principal

components is the best two-dimensional representation (i.e., represents the most energy) that I can generate. However, the best representation of all the data available may not be the best representation I can use to discriminate between a BSR and all of the other surrounding features in the seismic data volume (Figure 4.2).

To use PCA to study the individual impact of attribute **a** on the jth eigenvector, $\boldsymbol{S}_j$, I evaluate the squares of each coefficient in the eigenvectors $\mathbf{v}_m$

$$S_j = (v_{1j}^2 \quad v_{2j}^2 \quad ... \quad v_{Mj}^2) \tag{1}$$

where, larger coefficients are associated with seismic attributes having more contribution to that particular eigenvector. However, Guo et al. (2009), Roden et al. (2015), and Lubo-Robles and Marfurt (2019) noted that although higher variability may better represent the data mathematically, it may not help differentiate geologic features of interpretation interest from the overall response. For a mathematical explanation on how to implement PCA for seismic attribute selection, please refer to Appendix A.

Self-organizing maps (SOM)

SOM is an unsupervised machine learning technique (Kohonen, 1982) widely used for seismic facies identification (Roy et al. 2014; Roden et al. 2015; Zhao et al. 2016; Lubo-Robles and Marfurt, 2017; Ha et al., 2021). Using a suite of seismic attributes, SOM first projects the multi-dimensional input onto a 2D manifold and corresponding latent space (Zhao et al., 2015, 2016). Zhao et al. (2015, 2016) initialize their SOM algorithm using the first two principal components from PCA analysis.

After initialization, the 2D manifold is deformed to generate a suite of clusters that best represents the input data distribution, with the corresponding latent space mapped onto a 2D color bar (Stecker and Uden, 2002) where similar colors are associated with similar seismic responses/facies (Zhao et al. 2017, 2018). For more information of SOM for seismic facies classification and its mathematical implementation, please refer to Zhao et al. (2015, 2016).

Workflow

I select a suite of geometric and spectral candidate seismic attributes as input to evaluate meaningful input attribute combinations using PCA for three different types of training data. Given these attributes, I then perform an unsupervised facies classification to identify and differentiate the BSR from other target seismic facies in the Blake Ridge field.

As training strategies for PCA, I evaluate three cases: 1) using all samples extracted throughout a 3D grid spanning the entire data volume, (2) using only samples that fall within interpreter-generated polygons about the BSR seismic facies, and (3) using an equal number of samples for each of the four seismic facies, within a larger number of interpreter-generated polygons (Figure 4.3). Because seismic attributes have different units and PCA assumes Gaussian statistics (Guo et al., 2009; Honorio et al., 2014: Lubo-Robles and Marfurt, 2019), I apply a Z-score normalization to remove scale dependency. Then, I calculate the correlation matrix C of the normalized training data set, compute the eigenvectors and eigenvalues, and select seismic attributes showing the highest contribution in the eigenvectors (equation 1) for all cases.

Finally, using the selected seismic attribute combinations for all cases, I apply SOM to perform an unsupervised seismic facies classification and evaluate which combinations produce better SOM facies maps to identify and isolate the BSRs in the Blake Ridge seismic volume. To make an unbiased analysis, I use the same SOM parameters for all cases where only the input attributes are changing. Following Zhao et al. (2015, 2018), I select 256 colors as initial number of clusters and allow the SOM algorithm to group them into a smaller subset for subsequent interpretation. Although PCA and SOM are unsupervised algorithms, they are still biased. Clearly, they are biased by the attribute selection. Second, they are biased by the training data used to generate the eigenvectors and subsequently, the deformed SOM manifold.

Candidate seismic attributes

Following Chopra and Marfurt (2007), seismic attributes are all measurements estimated from seismic data that successfully allow geoscientists to quantify and interpret seismic patterns associated with changes in seismic geomorphology, structural framework, depositional environment, and reservoir properties.

Contrary to instantaneous or complex attributes (Taner et al., 1979), which analyze the real and imaginary part of the seismic trace using a single-trace analysis to compute changes in the amplitude, frequency, and phase, modern geometric attributes use multi-trace analysis – usually defining a 3D window – to obtain more robust estimations of geological features. Common geometric attributes include similarity and energy between seismic traces, changes in dip and azimuth, and reflector curvature (Chopra and Marfurt, 2007).

Gray-Level Co-Occurrence Matrix (GLCM) or textural attributes estimate lateral and vertical variations in the seismic amplitudes as a means to enhance changes in the seismic geomorphology (Haralick et al., 1973; Angelo et al., 2009, Matos et al., 2011, Di and Gao, 2017), whereas nonparallelism attributes (Qi and Marfurt, 2019) highlight lateral changes in the dip and energy of the seismic reflectors by computing different statistical measures. Because GLCM and nonparallelism attributes use a 3D analysis window for their computations, I consider these attributes to be part of the geometric attributes in this study.

Finally, by applying continuous wavelet transform (CWT) spectral decomposition, I analyze changes in the magnitude and phase components of the seismic data at different frequencies that can be related to variations in bed thickness and stratigraphy (Marfurt and Kirlin, 2001; Sinha et al., 2005; Chopra and Marfurt, 2007; Chopra and Marfurt, 2016).

Performing seismic facies classifications to highlight different geologic features, Zhao et al. (2016), Lubo-Robles et al. (2021, 2022), Salazar Florez and Bedle (2022) found that attributes measuring changes in the energy, frequency, dip, and morphology of the reflectors proved to be successful inputs for ML algorithms. Therefore, in this study, I consider seven candidate seismic attributes, GLCM entropy, total energy, peak frequency, peak magnitude, GLCM contrast, dip deviation, and coherence as input to PCA to find optimal attribute combinations and SOM for seismic facies analysis.

GLCM entropy and GLCM contrast: The GLCM entropy computes the level of disorder, whereas the GLCM contrast analyzes local variations in the intensity present in the seismic amplitudes (Chopra and Alexeev, 2006; Chopra and Marfurt, 2007; Yenugu et al., 2010; Di and Gao, 2017).

Total energy: Measures the energy inside a 3D window of seismic traces using eigenstructure analysis. This attribute is helpful to distinguish between strong and weak seismic reflectors (Gersztenkorn and Marfurt, 1999; Chopra and Marfurt, 2007).

Peak frequency and peak magnitude: These spectral decomposition attributes compute statistical estimations of the seismic spectrum and provide a means to interpret the general sequence stratigraphy and depositional environment (Marfurt and Kirlin, 2001). The peak frequency and peak magnitude are given by the mode of the spectrum. The former is helpful to analyze changes in bed thickness, whereas the latter is associated with changes in impedance and tuning thickness (Chopra and Marfurt, 2007; Zhao et al., 2016).

Dip deviation: Estimates lateral changes in the dip of the seismic reflector and it is useful to distinguish between parallel and chaotic reflectors (Qi and Marfurt, 2019).

Coherence: Computes the similarity between seismic traces inside a moving 3D window to map seismic discontinuities and chaotic, low energy reflectors and differentiate them from higher amplitude, homogenous seismic responses (Gersztenkorn and Marfurt, 1999; Chopra and Marfurt, 2007; Li and Lu, 2014).

In Figure 4.4, I show the seven candidate seismic attributes along inline 41. I observe that the BSRs are characterized by lower GLCM entropy, GLCM contrast and higher total energy, peak magnitude, and coherence. In addition, because the BSR cuts across dipping stratigraphic reflectors, attributes like dip deviation are useful. The continuous BSR towards the southwest shows lower dip deviation than the discontinuous BSRs in the northeastern

side. Also, I note that the former has a frequency of approximately 60 Hz, whereas the latter are not easily delineated using the peak frequency attribute.

In Table 4.1, I summarize the seismic amplitude and attribute response of the four facies of interest present in the Blake Ridge data set (Figure 4.2). Above the BSR, I observe high-amplitude, high-frequency continuous reflectors close to the sea floor that are characterized by low GLCM entropy, GLCM contrast, dip deviation, and high coherence, total energy, peak magnitude, and peak frequency ranging from approximately 70 to 120 Hz. In addition, low-amplitude, chaotic to sigmoid reflections are characterized by low total energy, and peak magnitude, whereas the dip deviation shows higher values towards the northeast. Moreover, the GLCM entropy, peak frequency, GLCM contrast, and coherence attributes show high variability.

Finally, the trapped free gas underlying the BSRs is mainly characterized by high-amplitude discontinuous reflectors and high values of total energy, peak magnitude, and low dip deviation and coherence. However, some areas associated with lower values of total energy, and peak magnitude, and higher values coherence and dip deviation are also visible. Furthermore, the GLCM entropy, peak frequency, GLCM contrast show high variability.

Definition of training data sets

For the first training data set (case 1), I simply use all data samples in the input seismic data, using voxels from every inline, crossline, and vertical sample within the analysis window shown in Figure 4.2. Note that the simple process of restricting my analysis window to follow the water bottom biases my "unsupervised" learning PCA and SOM algorithms to better represent the gas hydrates. I then construct training data sets 2 and 3 by

defining polygons on inlines 30, 35, 40, 45, and 50 enclosing my four seismic facies of interest (Figure 4.5). Above the BSR, the blue polygons enclose samples characterized by high-amplitude, high-frequency continuous reflectors close to the sea floor, whereas the green polygons enclose voxels associated with chaotic to sigmoid and lower amplitude reflections. The BSRs show strong leading negative amplitude reflections (purple polygons). Finally, high-amplitude discontinuous reflections below the BSR are related to trapped free gas (red polygons).

After picking the polygons, I extract the selected seismic voxels from my seven candidate seismic attributes (Figure 4.4). In this study, the training data for case 3 consist of 3208 voxels, in which 802 voxels have been randomly selected for each seismic facies to balance the training data set. The training data for case 2 consists of 802 voxels only associated with the BSR seismic facies.

In Figure 4.6, I show a cartoon explaining how the eigenvectors computed for PCA might be affected by different training data configurations. When the training data are selected to statistically represent all the data (case 1), the first eigenvector best represents the training data as a whole but does not serve as an optimum discriminator between the red and blue facies. However, when the training data are balanced (case 3), the first eigenvector serves as a much better discriminator between the two facies. Moreover, using different input attributes or increasing the dimensionality of the problem may further improve the discrimination between the two facies.

Results

Seismic attribute selection using PCA

To compare different strategies when choosing the most optimal seismic attributes using PCA to identify the BSR and distinguish it from other seismic facies in my data set, I analyze the first three eigenvectors for cases 1, 2, and 3 which contain 71.61%, 71.37%, and 75.26% of the variability of the data, respectively. Figure 4.7a shows eigenvector 1 for case 1 which represents 39.12% of the variability. For this eigenvector the highest contribution is given by the total energy attribute followed by the peak magnitude, coherence, GLCM contrast, dip deviation, GLCM entropy, and peak frequency.

Next, I examine eigenvector 1 for case 2 for training data drawn only from the BSRs, which represents 34.89% of the variability (Figure 4.7b). I observe that the total energy is still the most important attribute but now coherence is the second most important attribute. The GLCM entropy attribute becomes the third most important attribute, followed by the peak magnitude, GLCM contrast, dip deviation, and peak frequency.

Finally, using the balanced training data set containing the same number of voxels belonging to each of the four seismic facies (case 3), eigenvector 1 represents 42.56% of the variability of the data (Figure 4.7c). I note that a group of four attributes composed of the total energy, coherence, peak magnitude, and GLCM entropy have the highest contribution to this eigenvector. These attributes represent combination of the results seen in cases 1 and 2.

Eigenvector 2 for all cases represents an average of 19% of the variability. I observe that for case 1 (Figure 4.8a), GLCM entropy shows the highest contribution followed by GLCM contrast, peak frequency, total energy, peak magnitude, coherence, and dip deviation. For case 2 (Figure 4.8b), the peak magnitude has the highest importance, whereas the GLCM contrast and the total energy attributes are the second and third most important attributes, respectively. Considering case 3 (Figure 4.8c), the dip deviation has the highest contribution to eigenvector 2 followed by the peak frequency and peak magnitude attributes, whereas the remaining seismic attributes show very little impact in this eigenvector.

Finally, I examine eigenvector 3 representing an average of 15% of the variability of the data for all cases (Figure 4.9). Using all seismic attribute data samples (case 1), the three most important attributes are given by the dip deviation, peak frequency, and peak magnitude (Figure 4.9a) which is similar to the results seen for eigenvector 2 in case 3 (Figure 4.8c). When considering only the seismic voxels for the BSR facies (case 2), the peak frequency shows the highest contribution followed by the dip deviation, whereas GLCM contrast, peak magnitude, total energy, coherence, and GLCM entropy retain the remaining contribution (Figure 4.9b). For case 3, the seismic attributes showing higher importance are the peak frequency, GLCM contrast, and peak magnitude followed by the GLCM entropy, total energy, coherence, and dip deviation (Figure 4.9c).

In Table 4.2, I summarize the seismic attribute combinations used for performing an unsupervised seismic facies classification to identify the BSR and the rest of my target seismic facies. Because SOM applies PCA to project the data onto a 2D latent space for subsequent clustering and using a large number of input attributes might cause the 2D

manifold to represent increased variability of the data less accurately (Zhao et al., 2015, 2016), I select a maximum of three or four seismic attributes showing the highest importance as input for the ML algorithm.

Unsupervised seismic facies analysis using SOM

In Figure 4.10a, I analyze the SOM unsupervised facies classification corendered with the seismic amplitude volume along inline 61 (not used in the training for all three cases) considering the total energy, peak magnitude, and coherence as input (case 1a) because they show the highest contribution for eigenvector 1 in case 1 (Figure 4.7a and Table 4.2). I observe that the more continuous BSR towards the southwest and the more discontinuous BSR towards the northeast of the study area are correctly identified and they are characterized by a purple-reddish facies (the white arrows). However, the former BSR shows some discontinuities close to its edges (the blue arrows).

In addition, I note that high frequency, high-amplitude reflectors close to the sea floor are also being classified as purple facies and show overlap with the BSR (the red rectangle). Also, I observe that the trapped free gas below the BSR tends to be classified by a combination of purple (the red arrows) and dark blue-yellow facies (the orange arrows). The former facies represents voxels classified by the algorithm as BSR (the purple-reddish facies) because the free gas shows high amplitude in these areas, whereas the latter facies tends to be associated with a lower amplitude, more discontinuous seismic response below the BSR.

Furthermore, these dark blue-yellow seismic facies are also visible in slightly more discontinuous reflectors close to the sea floor (the gray arrow). Therefore, I hypothesize that

this blue-yellow seismic facies might be capturing changes in the amplitude and frequency content.

Studying the unsupervised classification along inline 61 for case 2a (Figure 4.10b), I note that the BSRs towards the southwest and northeast are characterized by purple seismic facies (the white arrows). The more continuous BSR towards the southwest is better identified by the algorithm than in case 1a (Figure 4.10a) because its definition towards the edges – characterized by lower reflectivity - has improved (the blue arrows). However, overlap between the BSR facies and reflectors closer to the sea floor increases (the red rectangle). Moreover, some dipping reflectors towards the northeast are also being classified as purple facies (the yellow arrows).

Then, analyzing the trapped free gas below the BSR, I observe that is mainly characterized by purple facies (the red arrows) – showing overlap with the BSR- and dark blue-greenish facies (the orange arrows). Moreover, similar to the results in case 1a, these clusters (dark blue-green facies for case 2a) are also in more discontinuous areas within reflectors closer to the sea floor and might be associated with changes in the amplitude and frequency.

Finally, I analyze the seismic facies classification corendered with the seismic amplitude along inline 61 for case 3a (Figure 4.10c), in which I use the total energy, coherence, peak magnitude, and GLCM entropy attributes as input (Table 4.2). I observe that the BSRs are correctly classified by the model (the white arrows). Moreover, this facies prediction offers a good tradeoff between the results obtained in cases 1a and 2a. Similar to case 2a, the BSR located in the southwestern side of the volume appears better defined

161

towards its edges (the blue arrows), whereas reflectors showing overlap with the BSR closer to the sea floor are reduced (red rectangle) – similar to the facies response seen in case 1a (Figure 4.10a).

I also note that some dipping reflectors located towards the northeastern side of the volume are still being classified as purple facies (the yellow arrows). Finally, the trapped free gas below the BSR still tends to be characterized by purple facies (the red arrows) and dark blue – yellow clusters that might be related to changes in the amplitude and frequency (the orange arrows).

Next, I evaluate the SOM facies classification results corendered with the seismic amplitude along inline 61 using the most optimal attribute combinations considering eigenvector 2 (cases 1b-3b; Table 4.2). Figure 4.11a shows the results for case 1b. I observe that this classification looks noisier than the results obtained in cases 1a-3a. Although the more continuous BSR towards the southwest is still correctly classified as green facies (the white arrows), the BSRs towards the northeastern side are more difficult to interpret.

In addition, an increase in the overlap between seismic facies is visible. Reflectors closer to the sea floor (the red rectangle) are characterized by green facies, whereas lower amplitude, more discontinuous reflectors throughout the seismic volume are classified by a combination of green, purple, blue, and yellow facies. Also, trapped free gas below the BSR tend to be characterized by a combination of several clusters and its interpretation becomes more challenging. I hypothesize that the variability captured by eigenvector 2 in case 1 might be associated with lower S/N responses in my multiattribute input.

Then, I analyze the SOM results for case 2b (Figure 4.11b). I note that this seismic classification looks less noisy, more geological than case 1b. The BSRs towards the southwest and northeast are classified as purple facies (the white arrows). However, some dipping reflectors (the yellow arrows) and higher amplitude reflectors closer to the sea floor (the red rectangle) still show overlap with the BSRs (the purple facies). In addition, the trapped free gas below the BSR is still associated with purple facies (the red arrows) - showing overlap with the BSRs – and dark blue-yellow facies that are still also visible in slightly more discontinuous, lower amplitude reflectors close to the sea floor (the orange arrows).

In Figure 4.11c, I study the SOM facies classification along inline 61 for case 3b. Similar to the results obtained in case 2b, this classification looks more geological and less noisy than the results in case 1b. Towards the southwest, I still can correctly identify the center and the edges of the more continuous BSR (the white arrows), whereas in the northeastern side of the seismic volume, the more discontinuous BSRs are also being correctly classified by the algorithm and are characterized by a purple seismic facies (the white arrows).

In addition, overlap between the BSRs and the reflectors closer to the sea floor is still visible (the red rectangle) and it increases compared to the classification for case 2b (Figure 4.11b). The dipping reflectors towards the northeast (the yellow arrows) are still characterized by purple seismic facies. However, they look noisier, more discontinuous than in cases 2a, 2b, and 3a. In addition, the trapped free gas is still characterized by a combination of two or more seismic facies. The purple seismic facies showing overlap with the BSR (the

red arrows) and the dark blue – red facies associated with areas potentially associated with changes in the amplitude and frequency of the reflectors (the orange arrows).

Finally, I study the unsupervised classifications corendered with the seismic amplitude along inline 61 using the selected attributes when considering eigenvector 3 for all cases (cases 1c-3c; Table 4.2). I observe that the seismic facies classification for case 1c offers identical results to case 3b because the same attributes dip deviation, peak frequency and peak magnitude show the highest contribution for both eigenvectors (Figure 4.12a).

Then, I evaluate the SOM results along inline 61 for case 2c (Figure 4.12b). Similar to the case 1b, the classification appears noisy. The BSRs towards the southwest is partially identified as green seismic facies (the white arrows) but overlap with other facies throughout the study area has increased. Moreover, interpretation of the more discontinuous BSRs towards the northeast and the trapped free gas below the BSRs is challenging. I hypothesize that using only the seismic voxels associated with the BSR seismic facies (case 2) for PCA attribute selection, eigenvector 3 captures noisier, less geological components in my input.

In Figure 4.12c, I study the seismic facies classification corendered with the seismic amplitude along inline 61 for case 3c. I note that the selected attributes from eigenvector 3, which represents a 14.6% variability of my balanced training data, still offer a geologically meaningful classification in which noisy components does not affect my interpretation of the geologic features of interest. The BSRs are still correctly classified as purple seismic facies (the white arrows). However, the edges of the southwestern BSR characterized by lower reflectivity appears slightly more discontinuous than in previous results (the blue arrow).

Moreover, overlap with the reflectors closer to the sea floor and other areas in my seismic volume is still visible and more prominent than in case 3a (red rectangle). The trapped free gas is still characterized by a combination of purple facies (the red arrows) – representing overlap with the BSR – and dark blue to yellow facies (the orange arrows).

Discussion

After considering three different strategies to select the training data to perform PCA for attribute selection and apply SOM for unsupervised seismic facies identification, I observe that combining geometric and spectral seismic attributes represents a powerful tool to characterize the continuous BSR towards the southwest, and more discontinuous BSRs towards the northeast in the Blake Ridge. Nevertheless, overlap between the BSR seismic facies, higher-amplitude reflectors closer to the sea floor, and trapped free gas is visible in the SOM facies map.

Holbrook et al. (2002) and Hornback et al. (2008) suggest that the more discontinuous BSRs might be related to gas migration associated with sediment waves that have been affected by erosion. In my results, I note that SOM classifies some reflectors within the GHSZ as BSRs – mainly purple facies - and these clusters might be associated with possible migration pathways that can potentially release gas hydrates in the ocean and atmosphere. However, higher-amplitude anomalies inside the GHSZ might also be related to misclassifications by the algorithm – similar to the overlap seen between the BSRs and reflectors close to the sea floor - or diagenetic changes and variations in the environment of deposition (Hornback et al., 2008).

I also note that lower amplitude, and chaotic to sigmoid reflectors within the GHSZ possibly associated with amplitude blanking and eroded sediment waves (Hornback et al. 2003; 2008) tend to be classified by a different set of clusters than the BSRs. According to Lee et al. (1994), Shipboard Scientific Party (1996), and Hornback et al. (2003), amplitude blanking is characterized by a decrease in the seismic amplitudes that can be related to hydrates filling the pore space. However, changes in the depositional environment or in the compaction of the sediments might also cause a reduction in the impedance contrast within the GHSZ (Lee et al. 1994; Hornback et al., 2003).

Therefore, these clusters might aid seismic interpreters in better defining possibly areas where gas hydrates are present. However, other geological effects and changes in the seismic S/N cannot be discarded as possible causes for these variations in the SOM facies map. Finally, although high amplitude trapped free gas shows overlap with the BSRs seismic facies, other areas underlying the BSR are characterized by a different set of clusters that appear to capture regions of decrease amplitude and frequency content.

In terms of using PCA for attribute selection, I observe that the lack of a quantitative measure to estimate how different attribute combinations – instead of individual attribute contributions – might impact the performance of the ML algorithm make the attribute selection subjective. Chenin (2020) selected eight attributes - representing more than 70% of the impact in the first three eigenvectors - to create combinations for SOM, whereas I limit myself to combinations using three or four attributes showing high contribution in the first three eigenvectors.

Nevertheless, I cannot rule out that the remaining four eigenvectors in my data, which retain an average variability of 27.25%, might also offer good attribute combinations for my facies analysis. Semisupervised and supervised techniques (Kim et al., 2019; Qi et al., 2020; Lubo-Robles et al., 2021) that quantitatively evaluate how different seismic attribute combinations affect the classification might offer a more robust approach to address this limitation.

Also, similar to Gao et al. (2009) and Lubo-Robles and Marfurt (2019), I found that higher variability does not necessarily mean more geological results. For case 1, I observe that attribute combinations associated with eigenvectors 1 and 3 offer better definition of the BSRs and surrounding facies than attributes related to eigenvector 2 which represent noisier components in the seismic data set. However, training strategies for cases 2 and 3 tend to improve this limitation. For case 2, geologically feasible results are given by the first 2 eigenvectors, whereas in case 3 attributes showing higher contribution in the first three eigenvectors provide good definition of the geologic features of interest.

Conclusion

In this study, I successfully apply SOM to map the BSRs and surrounding facies in a seismic volume located in the Blake Ridge and evaluate PCA as attribute selection technique under different training data selection strategies: (1) all samples in the volume, (2) samples only associated with the BSRs, and (3) balanced training data set considering four main target seismic facies seen in study area. I found that geometric seismic attributes measuring changes in similarity, energy, dip, and texture and spectral attributes that statistically summarize changes in the seismic spectrum represent an effective means to

highlight BSRs and confirm the presence of gas hydrates. Moreover, using different combinations of these attributes as input into SOM, I can correctly map continuous and discontinuous BSRs in the Blake Ridge. However, significant overlap between the SOM clusters for the BSR seismic facies, higher amplitude reflectors closer to the sea floor, and higher amplitude trapped free gas is visible in my data.

In general, reflectors within the GHSZ tends to be characterized by a different suite of SOM clusters -potentially associated with eroded sediment waves and amplitude blanking -, whereas some higher amplitude reflectors within the GHSZ are also classified as BSRs by the ML algorithm and might represent potential pathways for gas hydrates to migrate out of the subsurface. However, changes in the geology or misclassifications by the algorithm cannot be discarded as possible reasons for the clusters seen in the GHSZ.

Applying PCA for attribute selection, I found that using a balance training data set (case 3) offers a good tradeoff between BSRs identification, delineation of the edges of the continuous BSR associated with lower reflectivity, and reduction of overlap between the BSRs and the surrounding facies compared to using all seismic voxels (case 1) or only voxels associated with the BSR seismic facies (case 2). Moreover, all combinations of all attributes showing higher impact in the first three eigenvectors for case 3 – enclosing 75% of the input data variability - provide geologically feasible results, whereas the variability associated with eigenvectors 2 and 3 for cases 1 and 2, respectively, appear to be capturing seismic noise; thus, attribute combinations obtained from these eigenvectors provide SOM facies maps where geologic features of interest are difficult to interpret. Finally, because using PCA I evaluate the impact of individual attributes in a group of eigenvectors sorted by their

variability instead of quantitatively estimate the effect of different attribute combinations, determining how many attributes or eigenvectors should be used for the facies analysis is highly subjective.

Acknowledgments

Appendix A

PCA for attribute selection

Seismic attributes tend to have different units. For example, the coherence attribute ranges from 0 to 1, whereas energy attributes might range from 0 to +1000. Also, because PCA assumes Gaussian statistics, I first apply a Z-score normalization to each of the *M* candidate seismic attributes $\mathbf{a}_m$ subtracting the mean μ_m and divide by standard deviation σ_m – to remove scale dependency between the input features.

$$\hat{\mathbf{a}}_m = \frac{\mathbf{a}_m - \mu_m}{\sigma_m} \tag{A1}$$

where, $\hat{\mathbf{a}}$ represents the Z-normalized data.

Second, I compute the correlation matrix, **C**, from the normalized training data from *M* seismic attribute volumes as

$$C_{mj} = \frac{1}{N}\sum_{n=1}^{N} \hat{a}_{nm}\hat{a}_{nj}$$
(A2)

where N is number of voxels in the training data

Then, I compute the eigenvectors $\mathbf{v}_m$ from the correlation matrix given by

$$\mathbf{v}_m = \{v_{1m} \quad v_{2m} \quad \dots \quad v_{Mm}\}$$
(A3)

The jth principal components, p_{nj} at voxel n is the projection of an M-dimensional data vector onto the jth M-dimensional eigenvector computed as

$$p_{nj} = \mathbf{v}_j\hat{\mathbf{a}}_n = v_{1j}\hat{a}_{1n} + v_{2j}\hat{a}_{2n} + \dots + v_{Mj}\hat{a}_{Mn}$$
(A4)

To study the individual impact of attribute $\mathbf{a}$ on the jth eigenvector, $\boldsymbol{S}_j$, I evaluate the squares of each coefficient in the eigenvectors divided by the total energy in each eigenvector:

$$S_j = \frac{1}{\sum_{m=1}^{M} v_{mj}^2} (v_{1j}^2 \quad v_{2j}^2 \quad \dots \quad v_{Mj}^2)$$
(A5)

However, by definition

$$\sum_{m=1}^{M} v_{mj}^2 = 1$$
(A6)

Such that the impact of each seismic attribute for the jth eigenvector is given by

$$S_j = (v_{1j}^2 \quad v_{2j}^2 \quad \dots \quad v_{Mj}^2)$$
(A7)

References

Amin A., M. Deriche, M. A. Shafiq, Z. Wang, and G. AlRegib, 2017, Automated salt dome detection using an attribute ranking framework with a Dictionary-Based Classifier, Interpretation, **5**, no. 3, SJ61-SJ79.

Angelo, S.M, M. Matos, and K.J. Marfurt, 2009, Integrated seismic texture segmentation and clustering analysis to improved delineation of reservoir geometry: 79th Annual International Meeting, SEG, Expanded Abstracts, 1107-1111.

Bedle, H., 2019, Seismic attribute enhancement of weak and discontinuous gas hydrate bottom-simulating reflectors in the Pegasus Basin, New Zealand: Interpretation, **7**, no. 3, SG11-SG22.

Chenin, J., 2000, Examining seismic amplitude responses of gaseous media using unsupervised machine learning: M.S. thesis, University of Oklahoma.

Chopra, S., and V. Alexeev, 2006, Applications of texture attribute analysis to 3D seismic data: The Leading Edge, **25**, no. 8, 934-940.

Chopra, S., and K. J. Marfurt, 2007, Seismic attributes for prospect identification and reservoir characterization, SEG Geophysical Development Series, 11.

Chopra, S., and K.J. Marfurt, 2014, Churning seismic attributes with principal component analysis: 84th Annual International Meeting, SEG, Expanded Abstract, 2672-2676.

Chopra, S., and K.J. Marfurt, 2016, Spectral decomposition and spectral balancing of seismic data: The Leading Edge, **35**, 176-179.

Chopra, S., and K. J. Marfurt, 2019, Unsupervised machine learning applications for seismic facies classification: Presented at the Unconventional Resources Technology Conference, SEG, Global Meeting Abstracts, 3135-3142.

Clairmont R., H. Bedle, K. Marfurt, and Y. Wang, 2021, Seismic attribute analyses and attenuation applications for detecting gas hydrate presence: Geosciences, **11**, 450.

Collet T. S., and J. Ladd, 2000, Detection of gas hydrate with downhole logs and assessment of gas hydrate concentrations (saturations) and gas volumes on the Blake Ridge with electrical resistivity log data, *in* C. K. Paull, R. Matsumoto, P.J. Wallace, and W. P. Dillon, eds., Proceedings of the Ocean Drilling Program, Scientific Results, **164**, 179-191.

Davies, R. J., M. A. Morales Maqueda, A. Li, and M. Ireland, 2021, Climatically driven instability of marine methane hydrate along a canyon-incised continental margin: Geology, **49**, 973-977.

Di, H., and D. Gao, 2017, Nonlinear gray-level co-occurrence matrix texture analysis for improved seismic facies interpretation: Interpretation, **5**, SJ31-SJ40.

Dickens, G. R., 2003, A methane trigger for rapid warming?: Science, **229**, no. 5609, 1017.

Gersztenkorn, A., and K. J. Marfurt, 1999, Eigenstructure-based coherence computations as an aid to 3-D structural and stratigraphic mapping: Geophysics, **64**, no. 5, 1468-1479.

Guo, H., K. J. Marfurt, and J. Liu, 2009, Principal component spectral analysis: Geophysics, **74**, 35–43.

Haralick, R. M., K. Shanmugam, and I Dinstein, 1973, Textural features for image classification: IEEE Transactions on Systems, Man and Cybernetics, **3**, 610-621

Ha, T., D. Lubo-Robles, K. J. Marfurt, and B. C. Wallet, 2021, An in-depth analysis of logarithmic data transformation and per-class normalization in machine learning: Application to unsupervised classification of a turbidite system in the Canterbury Basin, New Zealand, and supervised classification of salt in the Eugene Island minibasin, Gulf of Mexico: Interpretation, **9**, no. 3, T685-T710.

He, L., O. Matsubayashi, and X. Lei, 2006, Methane hydrate accumulation model for the Central Nankai accretionary prism: Marine Geology, **227**, 201-214.

Holbrook, W. S., D. Lizarralde, I.A. Pecher, A. R. Gorman, K. L. Hackwith, M. Hornback, and D. Saffer, 2002, Escape of methane gas through sediment waves in a large methane hydrate province: Geology, **30**, no. 5, 467-470.

Honorio, B., A. Sanchetta, E. Pereira, and A. Vidal, 2014, Independent component spectral analysis: Interpretation, **2**, no. 1, SA21-SA29.

Hornback, M. J., W. S. Holbrook, A. R. Gorman, K L. Hackwith, D. Lizarralde, and I. Pecher, 2003, Direct seismic detection of methane hydrate on the Blake Ridge: Geophysics, **68**, no. 1, 92-100.

Hornback, M. J., D. M. Saffer, W. S. Holbrook, H. J. A. Van Avendonk, and A. R. Gorman, 2008, Three-dimensional seismic imaging of the Blake Ridge methane hydrate province: Evidence for large, concentrated zones of gas hydrate and morphologically driven advection: J. Geophys. Res., 113, B07101.

Jaiswal, P., 2016, Hydrate quantification: Integrating full-waveform inversion, seismic attributes, and rock physics: Interpretation, **4**, no.1, SA55-SA71.

Kennett, J. P., K. G. Cannariato, I. L. Hendy, and R. J. Behl, 2000, Carbon isotopic evidence for methane hydrate instability during Quaternary interstadials: Science, **288**, 128-133.

Kim, Y., R. Hardisty, and K. J. Marfurt, 2019, Attribute selection in seismic facies classification: Application to a Gulf of Mexico 3D seismic survey and the Barnett Shale: Interpretation, **7**, SE281–SE297.

Kohonen, T., 1982, Self-organized formation of topologically correct feature maps: Biological Cybernetics, **43**, 59–69.

Kuramoto, S., K. Tamaki, M.G. Langseth, D.C. Nobes, H. Tokuyama, K.A. Pisciotto, and A. Taira, 1992, Can opal-A/opal-CT BSR be an indicator of the thermal structure of the Yamato Basin, Japan Sea, *in* K. Tamaki, K. Suyehiro, J. Allan, M. McWilliams, et al., Proceedings of the Ocean Drilling Program, Scientific Results, **127/128**, no.2, 1145-1156.

Lee, M. W., D. R. Hutchinson, W. F. Agena, W. F. Agena, W. P. Dillon, J. J. Miller, and B. A. Swift, 1994, Seismic character of gas hydrates in the southeastern United States continental margin: Marine Geophysical Research, **16**, 163-184.

Li, F., and W. Lu, 2014, Coherence attribute at different spectral scales: Interpretation, **2**, no. 1, SA99–SA106.

Lubo-Robles, D., and K. J. Marfurt, 2017, Delineation of thick incised canyons using spectral-decomposition analysis, curvature and Self-Organizing Maps in the Exmouth Plateau, Australia: 87th Annual International Meeting, SEG, Expanded Abstract, 2420-2424.

Lubo-Robles, D., and K. J. Marfurt, 2019, Independent component analysis for reservoir geomorphology and unsupervised seismic facies classification in the Taranaki Basin, New Zealand: Interpretation, **7**, no. 3, SE19–SE42.

Lubo-Robles, D., T. Ha, S. Lakshmivarahan, K. J. Marfurt, and M. J. Pranter, 2021, Exhaustive probabilistic neural network for attribute selection and supervised seismic facies classification: Interpretation, **9**, no. 2, T421-T441.

Lubo-Robles, D., D. Devegowda, V. Jayaram, H. Bedle, K. J. Marfurt, and M. J. Pranter, 2022, Quantifying the sensitivity of seismic facies classification to seismic attribute selection: An explainable machine-learning study: Interpretation, **10**, no. 3.

Marfurt, K. J., and R.L. Kirlin, 2001, Narrow-band spectral analysis and thin-bed tuning: Geophysics, **66**, 1274–1283.

Matos, M., M. Yenugu, S. M. Angelo, and K. J. Marfurt, 2011, Integrated seismic texture segmentation and cluster analysis applied to channel delineation and chert reservoir characterization: Geophysics, **76**, no. 5, P11-P21.

Shipboard Scientific Party, 1996, Introduction, *in* C. K. Paull, R. Matsumoto, P. J. Wallace, et al., 1996, Proceedings of the Ocean Drilling Program, Initial Reports, **164**, 5-12.

Plaza-Faverola, A., D. Klaeschen, P. Barnes, I. Pecher, S. Henrys, and J. Mountjoy, 2012, Evolution of fluid expulsion and concentrated hydrate zones across the southern Hikurangi subduction margin, New Zealand: An Analysis from the depth migrated seismic data: Geochem. Geophys. Geosyst., 13, Q08018.

Posamentier, H. W., and V. Kolla, 2003, Seismic geomorphology and stratigraphy of depositional elements in deep-water settings. Journal of Sedimentary Research, 73, 367-388.

Qi, J., and K. Marfurt, 2019, Nonparallelism attributes and data adaptive Kuwahara image processing: 89th Annual International Meeting, SEG, Expanded Abstracts, 1858-1861.

Qi, J., B. Zhang, B. Lyu, and K. Marfurt, 2020, Seismic attribute selection for machine-learning-based facies analysis: Geophysics, **85**, no. 2, O17-O35.

Roden, R., T. Smith, and D. Sacrey, 2015, Geologic pattern recognition from seismic attributes: Principal component analysis and self-organizing maps: Interpretation, **3**, SAE59–SAE83.

Roden, R., and C. W. Chen, 2017, Interpretation of DHI characteristics with machine learning: First Break, **35**, no. 5, 55-63.

Roy A., A. S. Romero-Peláez, T. J. Kwiatkowski, and K. J. Marfurt, 2014, Generative topographic mapping for seismic facies estimation of a carbonate wash, Veracruz Basin, southern Mexico: Interpretation, **2**, no. 1, SA31-SA47.

Salazar Florez, D., and H. Bedle, 2022, Study on the parameterization response of probabilistic neural networks for seismic facies classification in the Gulf of Mexico: Interpretation, **10**, no. 1, 1-23.

Shipley, T. H., M. H. Houston, R. T. Buffler, F. J., Shaub, K. J. McMillen, J. W. Ladd, and J. L. Worzel, 1979, Seismic evidence for widespread gas hydrate horizons on

continental slopes and rises: The American Association of Petroleum Geologist (AAPG) Bulletin, **63**, no. 12, 2204-2213.

Sinha S., P. Routh, P. Anno, and J. Castagna, 2005, Spectral decomposition of seismic data with continuous-wavelet transform: Geophysics, **70**, no. 6, 19-25.

Strecker, U., and R. Uden, 2002, Data mining of 3D post- stack attribute volumes using Kohonen self-organizing maps: The Leading Edge, **21**, 1032–1037.

Taner, M. T., F. Koehler, and R. E. Sheriff, 1979, Complex seismic trace analysis: Geophysics, **44**, no. 6, 1041-1063

Wang, Z., C. Yin, X. Lei, F. Gu, and J. Gao, 2015, Joint rough sets and Karhunen-Loève transform approach to seismic attribute selection for porosity prediction in a Chinese sandstone reservoir: Interpretation, **3**, SAE19–SAE28.

Wood, W. T., and C. Ruppel, 2000, Seismic and thermal investigations of the Blake Ridge gas hydrate area: A synthesis, *in* C. K. Paull, R. Matsumoto, P.J. Wallace, and W. P. Dillon, eds., Proceedings of the Ocean Drilling Program, Scientific Results, **164**, 253-264.

Yenugu, M., K. J. Marfurt, and S. Matson, 2010, Seismic texture analysis for reservoir prediction and characterization: The Leading Edge, **29**, no. 9, 1116-1121.

Yoo D. G., N. K. Kang, B. Y. Yi, G. Y. Kim, B. J. Ryu, K. Lee, G. H. Lee, and M. Riedel, 2013, Occurrence and seismic characteristics of gas hydrates in the Ulleung Basin, East Sea: Marine and Petroleum Geology, **47**, 236-247.

Zhao, T., V. Jayaram, A. Roy, and K. J. Marfurt, 2015, A comparison of classification techniques for seismic facies recognition: Interpretation, **3**, no. 4, SAE29–SAE58.

Zhao, T., J. Zhang, F. Li, and K. J. Marfurt, 2016, Characterizing a turbidite system in Canterbury Basin, New Zealand, using seismic attributes and distance-preserving self-organizing maps: Interpretation, **4**, no. 1, SB79-SB89.

Zhao, T., F. Li, and K. J. Marfurt, 2017, Constraining self-organizing map facies analysis with stratigraphy: An approach to increase the credibility in automatic seismic facies classification: Interpretation, **5**, no. 2, T163-T171.

Zhao, T., and K. J. Marfurt, 2017, Different training sample selection strategies in unsupervised seismic facies analysis: 87th Annual International Meeting, SEG, Expanded Abstracts, 2132-2136.

Zhao, T., F. Li, and K. J. Marfurt, 2018, Seismic attribute selection for unsupervised seismic facies analysis using user-guided data-adaptive weights: Geophysics, **83**, no. 2, O31-O44.
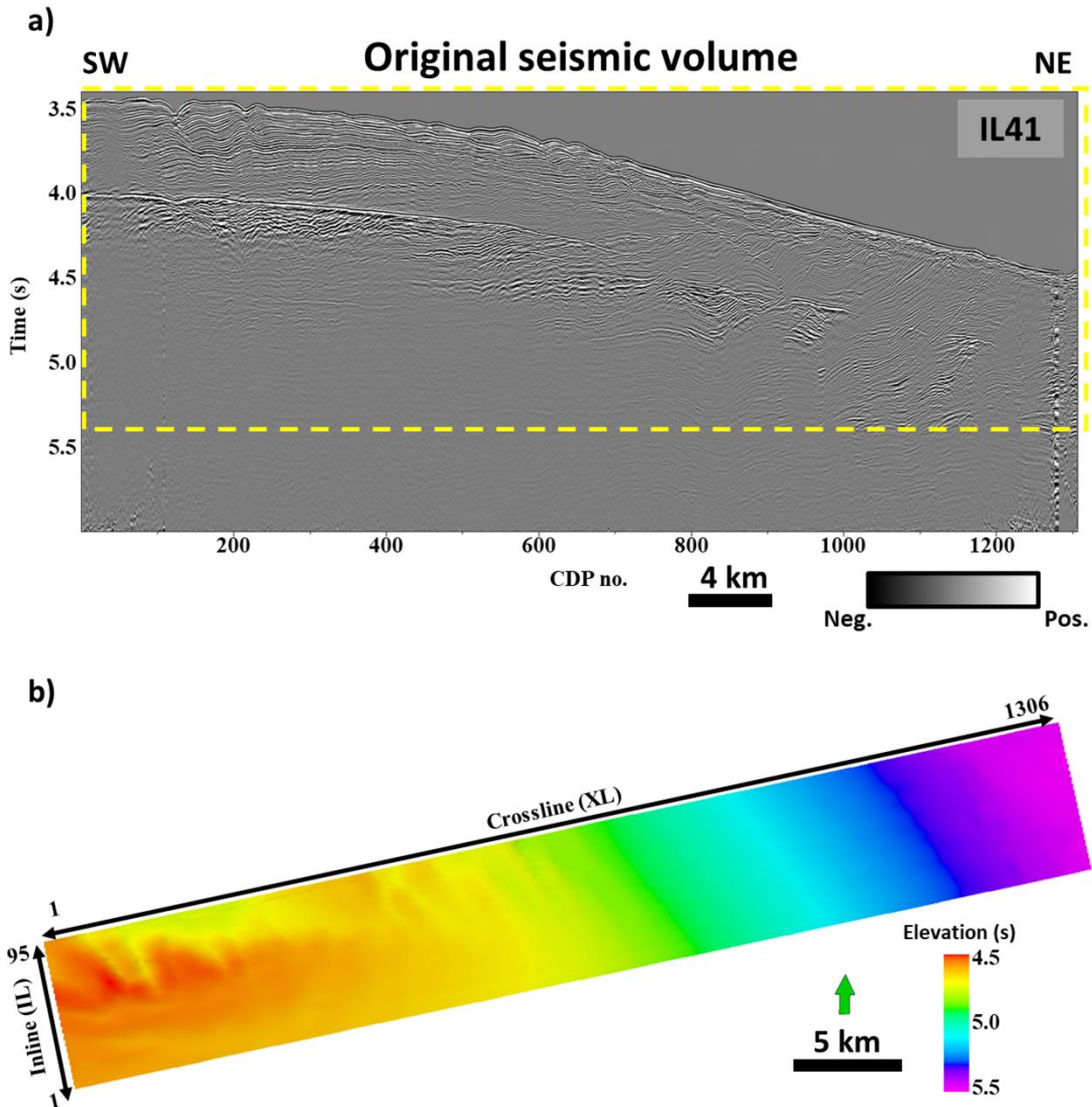
Chapter 4 Figures

Figure 4.1. The 3D Blake Ridge seismic volume. (a) Representative vertical section along inline 41. (b) Phantom horizon ranging from 4.5 to 5.5 s generated after picking the sea floor reflector. I bracket the seismic geologic features of interest (the yellow rectangle) and discard areas characterized by lower signal-to-noise ratio (S/N) with little interpretational value.
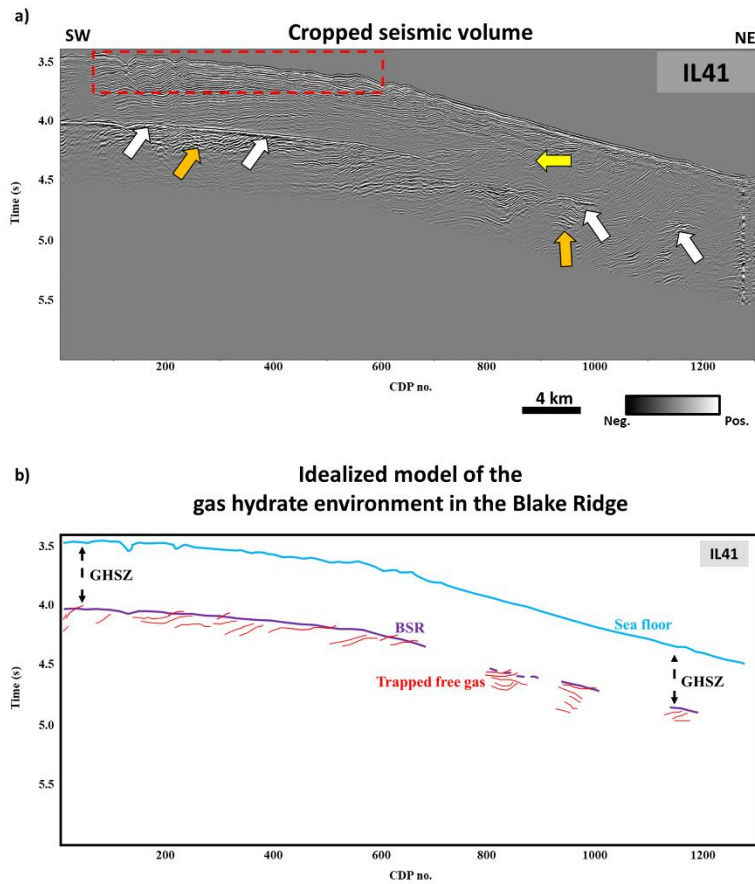
Figure 4.2. Seismic response of target seismic facies. (a) Along inline 41. Four main seismic facies are visible. The BSR cross-cuts strata and it is characterized by a leading negative high-amplitude reflector (the white arrows). Above the BSR, I observe high-amplitude (the yellow arrows), chaotic to sigmoid, low-amplitude reflectors whereas reflectors close to the sea floor are associated with high-amplitude, high frequency seismic response. Below the BSRs, high-amplitude discontinuous reflectors are seen (the orange arrows). (b) Idealized model of the gas hydrate environment in the Blake Ridge. The GHSZ is characterized by favorable pressure and temperature conditions for gas hydrate development and represents the region from the BSR up to the sea floor. The BSR tends to be parallel to the sea floor, whereas trapped free gas underlies the BSR.
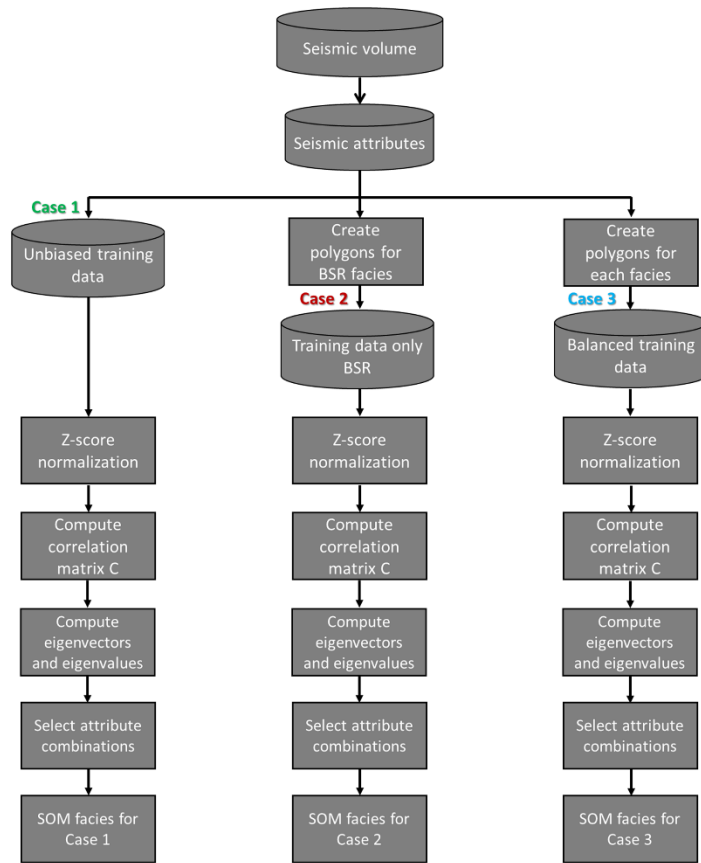
Figure 4.3. PCA for attribute selection and SOM for unsupervised seismic facies workflow. To delineate the BSR and differentiate it from other seismic facies in the Blake Ridge, I select a suite of spectral and geometric seismic attributes. To determine meaningful seismic attributes, I pick a suite of polygons enclosing the four target seismic facies and analyze three training data selection strategies for PCA (1) unbiased training data using all samples in the 3D seismic volume, (2) biased training data using samples associated with the BSR seismic facies, and (3) biased training data using same number of samples per each of the four seismic facies. Furthermore, I also apply Z-score normalization to remove scale dependency between seismic attributes. Next, I compute the correlation matrix C, calculate the eigenvectors and eigenvalues. Then, I select seismic attributes associated with high impact in the eigenvectors. Finally, using the selected attributes as input for SOM, I perform an unsupervised seismic facies analysis for each case in my analysis to delineate and isolate the BSRs.
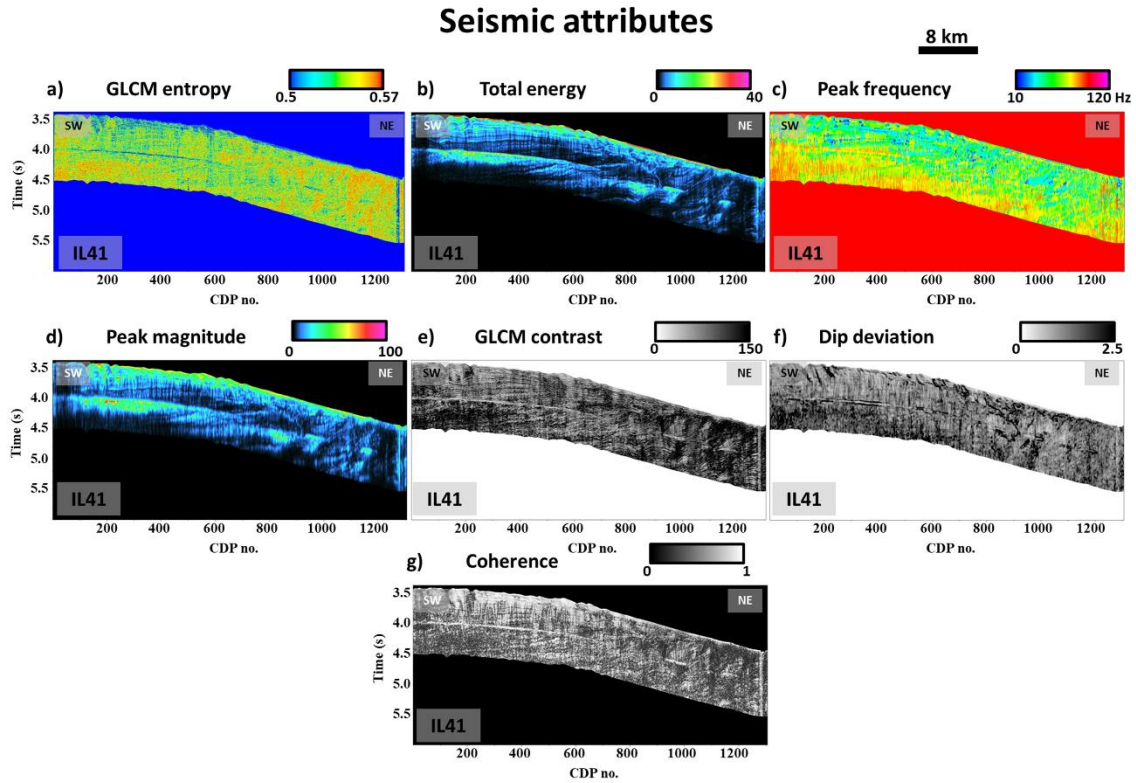
Figure 4.4. Seismic attributes along inline 41. (a) GLCM entropy, (b) total energy, (c) peak frequency, (d) peak magnitude, (e) GLCM contrast, (f) dip deviation, and (g) coherence. The BSRs show lower GLCM contrast, GLCM entropy, and high total energy, coherence, and peak magnitude. The continuous BSR towards the southwest is characterized by low values of dip deviation and peak frequency of approximately 60 Hz. The discontinuous BSRs towards the northeast are characterized by higher dip deviation, whereas they cannot be correctly interpreted using the peak frequency attribute.
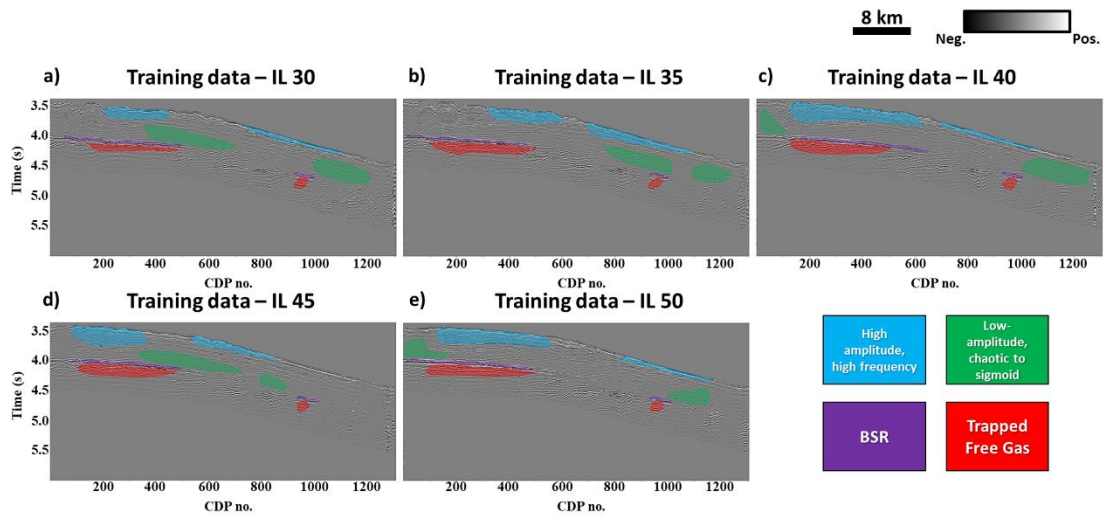
Figure 4.5. Training data sets definitions (a-e) The training data consist of manually picked polygons enclosing the BSRs (purple polygons), high-amplitude, high frequency reflectors (blue polygons), chaotic to sigmoid, low-amplitude reflectors (green polygons), and high-amplitude, discontinuous reflectors associated with trapped free gas below the BSRs (red polygons).
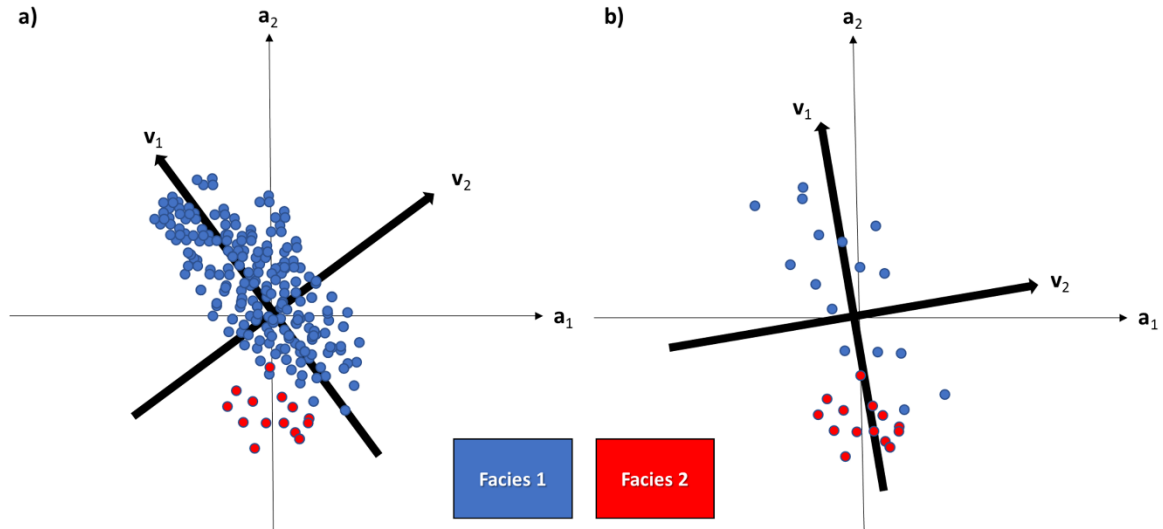
Figure 4.6. Cartoons showing the relation between choice of training data and eigenvectors v_1 and v_2. Red circles represent attribute values a_1 and a_2 for voxels associated with the target facies, whereas blue circles represent values associated with all other facies. (a) The first eigenvector v_1 best represents the data as a whole when the training data are selected to statistically represent all the data but does not discriminate between the blue and red seismic facies. (b) The first eigenvector v_1 represents a better discriminator between the seismic facies when the training data are balanced (~15 voxels representing each facies in this image). Note that the center of the crossplot has shifted such the mean value of the training data in the two images is at the origin of the a_1 and a_2 axes. Finally, increasing the number of input attributes or selecting different attributes might improve the differentiation between the seismic facies.
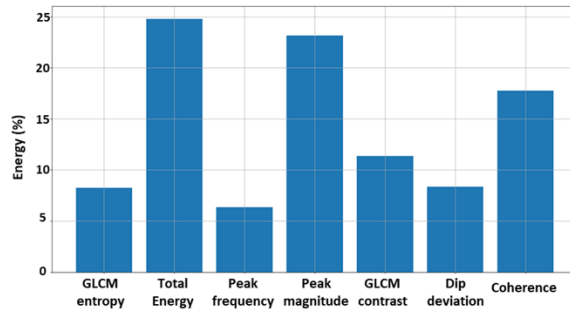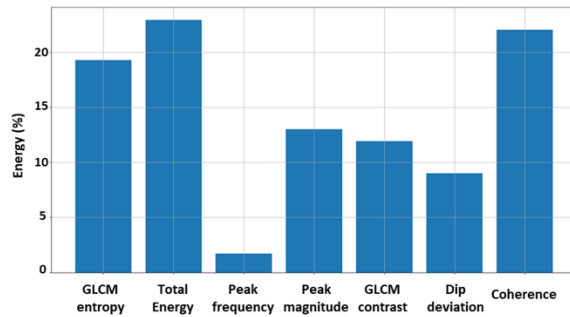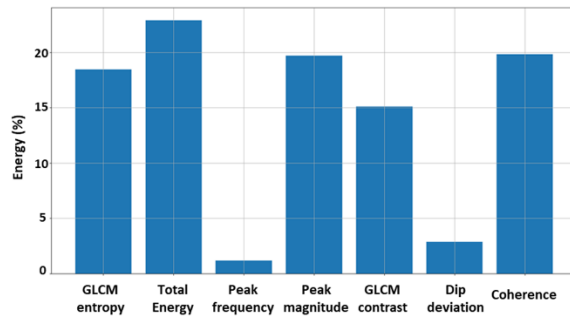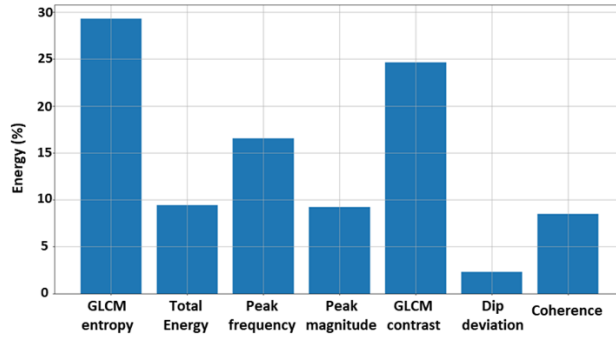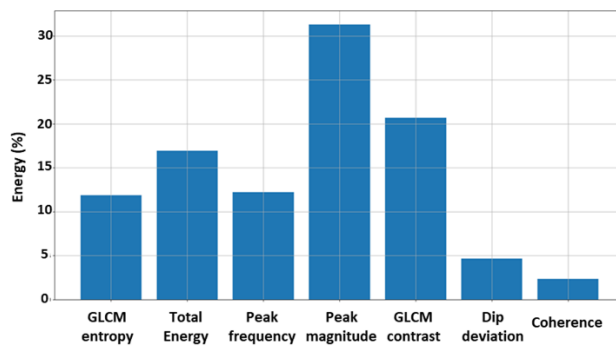
Figure 4.7. Eigenvector 1 for the three training data selection strategies. (a) using all samples in the seismic volume as training data (case 1). I observe that the total energy attribute shows the highest contribution followed by the peak magnitude, coherence, GLCM contrast, dip deviation, GLCM entropy, and peak frequency. (b) using training data considering only voxels associated with the BSR (case 2). The total energy still shows the highest contribution, whereas coherence becomes the second most important attributes, followed by the GLCM entropy, the peak magnitude, GLCM contrast, dip deviation, and peak frequency. (c) using a balanced training data considering the four target seismic facies (case 3). The most meaningful attributes are given by the total energy, coherence, peak magnitude, and GLCM entropy.

Figure 4.8. Eigenvector 2 for the three training data selection strategies. (a) using all samples in the seismic volume as training data (case 1). The highest contribution is associated with the GLCM entropy, whereas the second most important attributes is given by the GLCM contrast, followed by the peak frequency, total energy, peak magnitude, coherence, and dip deviation. (b) using training data considering only voxels associated with the BSR (case 2). The highest contribution is given by the peak magnitude, followed by the GLCM contrast, and total energy seismic attributes. (c) using a balanced training data considering the four target seismic facies (case 3). The dip deviation attribute shows the highest impact, followed by the peak frequency, and peak magnitude.
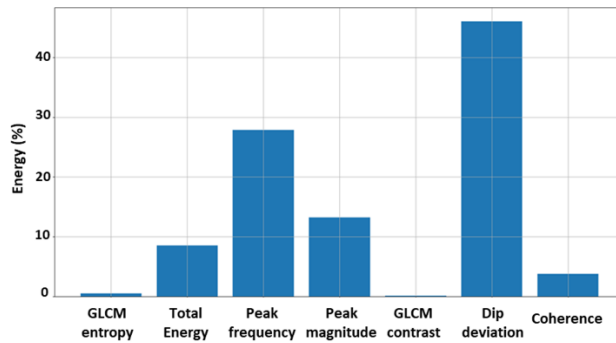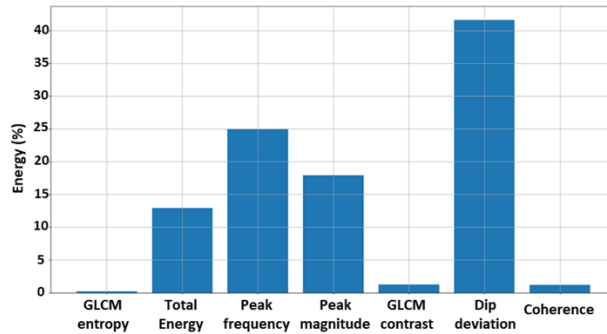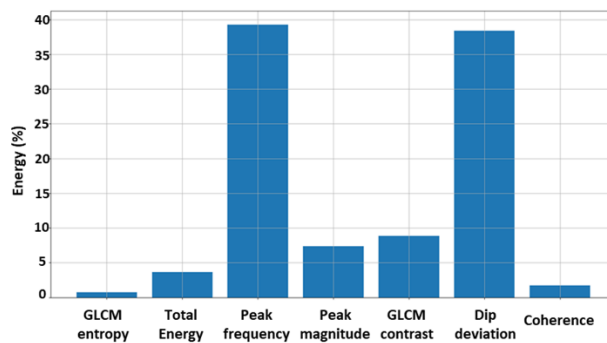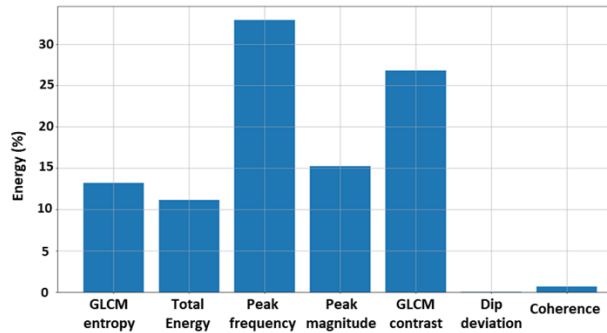
Figure 4.9. Eigenvector 3 for the three training data selection strategies. (a) using all samples in the seismic volume as training data (case 1). Dip deviation shows the highest contribution, followed by the peak frequency, and peak magnitude. (b) using training data considering only voxels associated with the BSR (case 2). The most important attribute is given by the peak frequency, whereas the dip deviation is the second most important attribute, followed by the GLCM contrast, peak magnitude total energy, coherence, and GLCM entropy. (c) using a balanced training data considering the four target seismic facies (case 3). The peak frequency has the highest impact followed by the GLCM contrast, peak magnitude, GLCM entropy, total energy, coherence, and dip deviation attributes.

Figure 4.10. SOM facies prediction corendered with the seismic amplitude along inline 61 for cases 1a, 1b, and 1c. (a) For case 1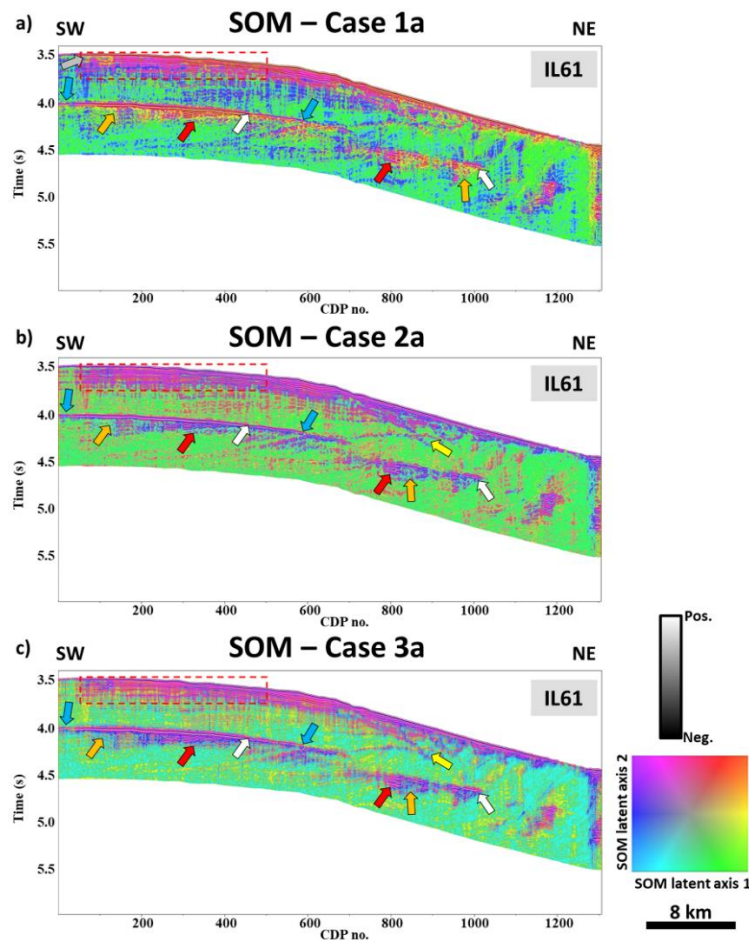a, I consider the total energy, peak magnitude and coherence attributes as input. The more discontinuous BSR towards the northeast and the more continuous BSR towards the southwest are characterized by a purple-reddish facies (the white arrows). However, some discontinuities close to the edges of the continuous BSR are visible (the blue arrows). The high-amplitude, high frequency reflectors close to the sea floor (red rectangle) and the high-amplitude discontinuous reflectors associated with trapped free gas below the BSR (the red arrows) tend to also be characterized by purple facies. However, some reflectors below the BSRs can be characterized by dark blue-yellow facies associated with of lower-amplitude, more discontinuous reflectors (the orange arrows). (b) For case 1b, the BSRs are characterized by purple facies (the white arrows), whereas the edges of the more continuous BSR are better delineated (the blue arrows). (c) For case 1c, I use as input for SOM the total energy, coherence, peak magnitude, and GLCM entropy attributes. The BSRs are characterized by purple seismic facies (the white arrows). Moreover, case 1c provides better delineation than case 1a of the edges of the continuous BSR towards the southwest, and less overlap between seismic facies than case 1b (the red rectangle).
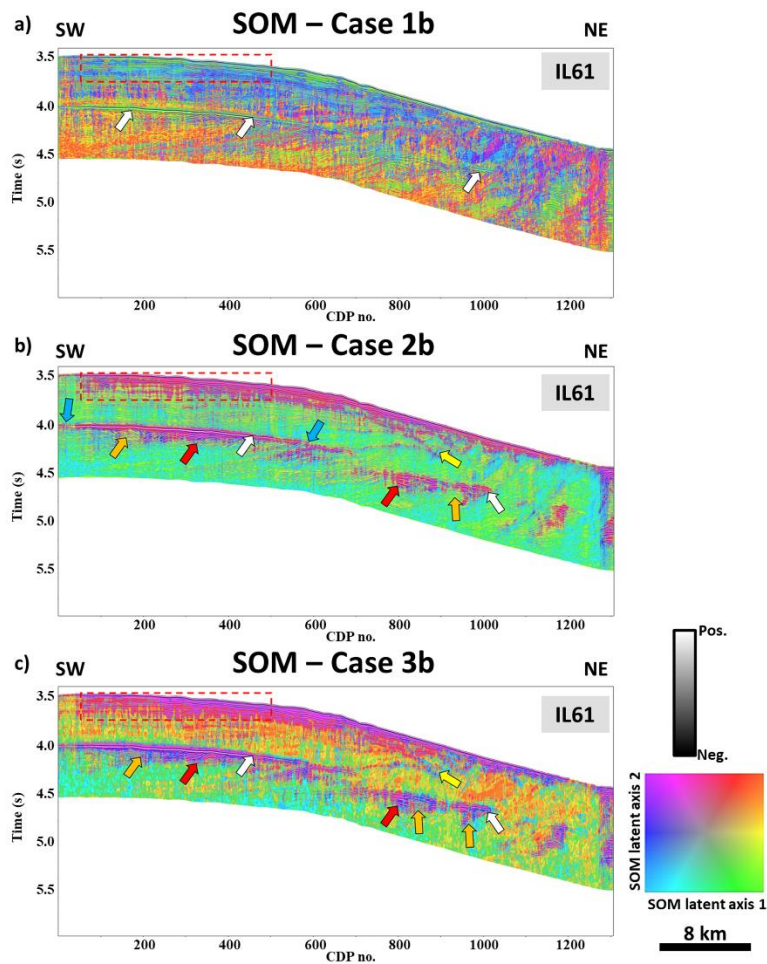
Figure 4.11. SOM facies prediction corendered with the seismic amplitude along inline 61 for cases 2a, 2b, and 2c. (a) For case 1b, the BSR towards the southwest is characterized by green seismic facies (the white arrows). However, the classification looks noisier which makes the interpretation of the more discontinuous BSRs towards the northeast challenging. Furthermore, there is an increase in the overlap between the target seismic facies. (b) For case 2b, the BSRs are characterized by purple seismic facies (the white arrows). Also, I observe some dipping reflectors (the yellow arrows) and high-amplitude reflectors close to the sea floor (the red rectangle) being classified as purple seismic facies. The trapped free gas underlying the BSRs tend to be classified as a combination of purple facies (the red arrows) and dark blue-yellow facies (the orange arrows) by the algorithm. (c) For case 2c, the BSRs are still correctly classified as purple seismic facies (the white arrows). I also observe that some dipping reflectors (the yellow arrows) and high-amplitude, high frequency reflectors (the red rectangle) above the BSRs are also characterized by purple seismic facies. Finally, the trapped free gas below the BSR still shows some overlap with the BSR seismic facies (the red arrows), whereas dark-blue-red facies represents area potentially associated with changes in the amplitude and frequency (the orange arrows).
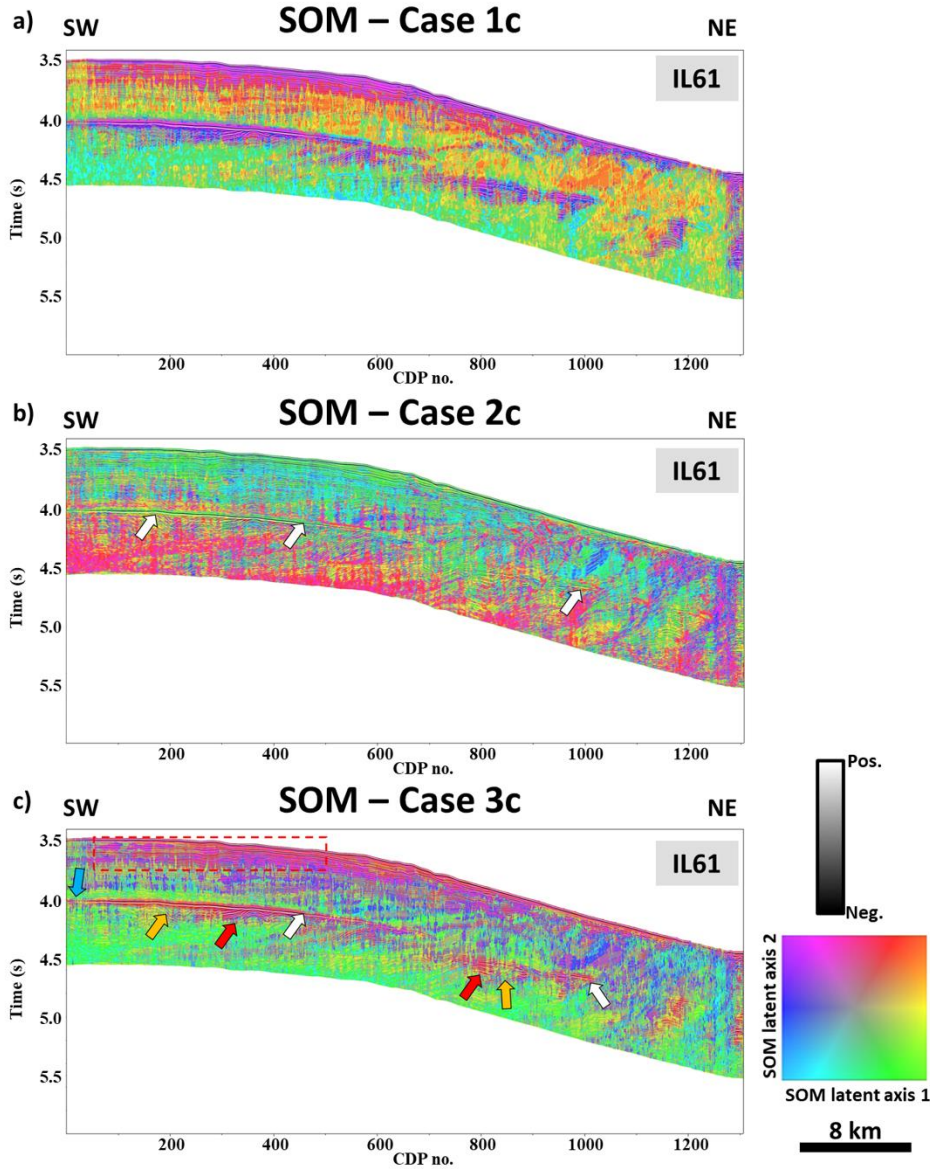
Figure 4.12. SOM facies prediction corendered with the seismic amplitude along inline 61 for cases 3a, 3b, and 3c. (a) Case 3a offers the same results than case 1c because the same input attributes, dip deviation, peak frequency and peak magnitude, are used for SOM. (b) For case 3b, the classification appears noisier similar to case 1b. The continuous BSRs towards the southwest is defined as green seismic facies (the white arrows). However, correct identification of the surrounding geologic features such as the discontinuous BSRs and trapped free gas is challenging. (c) For case 3c, the BSRs are still characterized by purple seismic facies (the white arrows). However, the edges of the BSRs towards the southwest appear more discontinuous than in previous results (the blue arrows). Finally, overlap between the BSR and surrounding seismic facies is still visible.
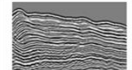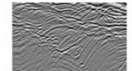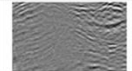
Chapter 4 Tables

Seismic facies	Vertical slice	Seismic response	GLCM entropy	Total energy	Peak frequency	Peak magnitude	GLCM contrast	Dip deviation	Coherence
Reflectors above the BSR		Sea floor shows strong positive reflection followed by high-amplitude, high-frequency reflectors	Low entropy	High energy	Peak frequencies range from 70 to 150 Hz	High peak magnitude	Low contrast	Low dip deviation	High coherence
		Chaotic to sigmoid reflectors	Highly variable (Low to high values of entropy)	Low energy	Highly variable (Low to high values of peak frequency)	Low peak magnitude	Highly variable (Low to high values of contrast)	Low dip deviation (Higher values are seen towards the NE)	Highly variable (Low to high values of coherence)
		Very low-amplitude reflectors / low internal reflectivity							
BSR		Strong leading negative amplitude cross-cutting strata and parallel to the ocean bottom	Low entropy	High energy	Continuous BSR towards the SW ~60 Hz. Discontinuous BSRs towards the NE are not easily delineated	High peak magnitude	Low contrast	Low to high dip deviation. Higher dip deviation towards the NE	High coherence
Trapped free gas		High-amplitude discontinuous reflectors below the BSR	Highly variable (Low to high values of entropy)	High energy (Some areas showing lower energy are visible)	Highly variable (Low to high values of peak frequency)	High peak magnitude (Some areas showing lower peak magnitude are visible)	Highly variable (Low to high values of contrast)	Low dip deviation (Some areas showing higher dip deviation are visible)	Low coherence (Some areas showing higher coherence are visible)

Table 4.1. Seismic amplitude and attribute response of the four target seismic facies in the Blake Ridge seismic volume. Above the BSR, the high-amplitude, high frequency reflectors close to the sea floor are associated with high coherence, total energy, peak magnitude, and low GLCM entropy, GLCM contrast, dip deviation and peak frequency ranging from approximately 70 to 120 Hz, whereas the low-amplitude, chaotic to sigmoid reflections show high variability for the GLCM entropy, peak frequency, GLCM contrast, and coherence attributes and low values of total energy, and peak magnitude. Below the BSR, the trapped free gas associated with high-amplitude discontinuous reflector in general shows high values of total energy, peak magnitude, and low dip deviation and coherence. However, some higher values of coherence and low values of total energy, peak magnitude, and dip deviation are seen. Finally, the GLCM entropy, peak frequency, GLCM contrast attributes are characterized by high variability.

	Eigenvector 1	Eigenvector 2	Eigenvector 3
Case 1	Case 1a	Case 1b	Case 1c
	Total energy, peak magnitude, coherence	GLCM entropy, GLCM contrast, peak frequency	Dip deviation, peak frequency, peak magnitude
Case 2	Case 2a	Case 2b	Case 2c
	Total energy, coherence, GLCM entropy	Peak magnitude, GLCM contrast, total energy	Peak frequency, dip deviation, GLCM contrast
Case 3	Case 3a	Case 3b	Case 3c
	Total energy, coherence, peak magnitude, GLCM entropy	Dip deviation, peak frequency, peak magnitude	Peak frequency, GLCM contrast, peak magnitude

Table 4.2. Selected seismic attributes to use as input for SOM to perform an unsupervised seismic facies analysis to identify BSRs and differentiate it from surrounding seismic facies in the Blake Ridge seismic volume. For SOM, I select a maximum of three or four seismic attributes characterized by highest impact in the first three eigenvectors for cases 1, 2, and 3.

Chapter 5: Conclusions

In this dissertation, I studied the importance of the choice of seismic attributes when using machine learning (ML) to perform a seismic facies analysis. I found that combining attributes measuring changes in the continuity, dip, energy, texture, and spectral seismic response represents a robust method to distinguish between salt, mass transport deposits (MTDs), and background conformal reflectors in the Gulf of Mexico, USA and to identify BSRs in the Blake Ridge, offshore South Carolina, USA. Also, I find that the overlap between the predicted facies increases or decreases depending on the seismic attributes used, the seismic data (and subsequent attribute) quality, or how the training data were selected.

I introduced a novel technique which I call exhaustive probabilistic neural network (PNN) by coupling a PNN with an exhaustive search algorithm. This method tested all possible combinations of seismic attributes, selected the optimal combination to differentiate salt and nonsalt facies, and rejected irrelevant attributes. Furthermore, it demonstrated that redundant attributes could complement each other to provide better facies separation and reduced the Hughes phenomena which might cause a decrease in the performance of the PNN associated with increasing the number of input attributes.

Applying Shapley additive explanations (SHAP) to a random forest model and adding band-limited random noise or using a Kuwahara filter to the input attributes, I found that the attribute importance changes based on their quality and the target facies analyzed. Moreover, I observed that the ML model is learning a set of rules in multiattribute space. Because MTDs, salt, and conformal siliciclastic sediments might show better or worse

191

discrimination depending on the seismic attribute analyzed, the use of multiattribute analysis offers a good approach to perform a facies classification because it maximizes the differentiation among seismic facies.

Finally, I evaluated the popular principal component analysis (PCA) to select the best seismic attributes. Although considered to be either a projection or unsupervised learning technique, I introduced a component of supervision (in actuality, bias) by comparing three different training data configurations. Once the best attributes for that training were selected, I applied self-organizing maps (SOM) to perform the final facies analysis and found that using the same number of samples per each target facies provides the best discrimination between localized anomalies of interest (such as the BSRs) and the surrounding (dominant) facies. Unfortunately, the absence of a quantitative metric to test alternative attribute combinations makes the selection technique less useful than the exhaustive PNN method.

I hope this dissertation represents a guide to seismic interpreters to better select the input seismic attributes and better understand how these might impact their ML-based seismic facies analysis.